

**ON THE USE OF OVERHEAD PINS  
FOR PART ORIENTING – AN EXPLORATORY STUDY**

by

Herbert F. Noriega

B.A.Sc., Mechanical Engineering

University of Waterloo, 1999

THESIS SUBMITTED IN PARTIAL FULFILLMENT OF  
THE REQUIREMENTS FOR THE DEGREE OF  
MASTER OF APPLIED SCIENCE  
in the Department  
of  
Engineering Science

© Herbert F. Noriega 2003

SIMON FRASER UNIVERSITY

February 2003

All rights reserved. This work may not be  
reproduced in whole or in part, by photocopy  
or other means, without permission of the author.

## Approval

Name: Herbert F. Noriega  
Degree: Master of Applied Science  
Title of thesis: On the Use of Overhead Pins for Part Orienting – An  
Exploratory Study.

### Examining Committee:

Chair: Dr. John Dill  
Professor – Engineering Science  
Committee Chair

---

Dr. Shahram Payandeh  
Professor – Engineering Science  
Co-Senior Supervisor

---

Dr. Kamal K. Gupta  
Professor – Engineering Science  
Co-Senior Supervisor

---

Dr. William A. Gruver  
Professor – Engineering Science  
Examiner

Date approved: Tuesday, February 25, 2003

## Abstract

The process of part orienting refers to aligning a batch of parts to be assembled in a desired or unique configuration from an unknown initial configuration. This thesis presents an innovative approach towards the development of a hybrid part orienter, where hybrid denotes something that has two or more different types of functionalities operating towards the same goal.

Focusing on the principle of minimalism, this thesis investigates the use of overhead pins of various classes over a slow moving conveyor to orient polygonal planar parts. First, a study is carried out to understand the motion behaviour of these parts when contacting point obstacles. Then, to represent the parts' behaviour configuration maps are created. Configuration maps encapsulate the physics of an operation such as a part contacting a pin, indicating the part's final orientation at the end of contact from an initial orientation prior to contact. Lastly, using these configuration maps a simple planner is implemented. The planner returns sequences of pins to orient a given part from a random initial state to a final orientation set; thereby, providing a solution to the problem of part orienting using overhead pins.

Nonetheless, cases in which a single final orientation is not found are encountered, and thus, a force/torque sensor is incorporated to help distinguish between the possible final orientation sets. Results obtained from an empirical exercise show that the force/torque sensor allows for the distinction of the initial states of a given polygon, and in conjunction with the planner results, the final orientation set can be known.

Also, using the force/torque sensor a distinction between different contact types (vertex vs. edge) against a pin are studied. The objective is to identify cases where a vertex contact may lead to unpredicted motion causing the orienting procedure to yield unexpected results.

Finally, limitations in orienting parts with overhead pins exist due to the complexity of the problem. Therefore, the purpose of the work in this thesis is to serve as an introductory study towards developing a more complete mechanics-based hybrid part feeder that uses a new class of orienting devices: overhead pins.

## **Dedication**

I dedicate this thesis to those who have seen me throughout all moments in life,  
my family.

To mom and dad, for their unconditional love and support.

To my brothers (Axel, Erick, and Erwin), for shaking their heads at me when necessary  
and always finding a way to make me laugh.

And to Grandma, for believing in me.

## Acknowledgments

I start by acknowledging and thanking my supervisors, Dr. Kamal Gupta and Dr. Shahram Payandeh, for making this possible and who through it all provided their advice and support towards the development of this work.

I then extend my utmost gratitude to the number of people who in one way or another contributed to make my stay here most entertaining and fruitful as well as challenging and rewarding. Extending from the many open-ended and intricate academic discussions and conversations, to sitting down with me to make sense of the obvious, to simple words of encouragement in the dire moments of need, I am indebted.

And so I thank (alphabetically): María del Carmen Amezquita, Cristofer Atiencia, George Austin, Mahta Boozari, Rebecca Brumer, Marta Fernández, Ian Gipson, Dr. Bill Gruver, Veljko Jovanovic, Slaven Karalic, Aaron Lee, Qingguo Li, Temei Li, Lakshman (Lucky) One, Paris Polydorou, Brigitte Rabold, Karolla Romero, Bernard Smit, Babak Taati, Frank Turco, Valerie Walker, Pengpeng Wang, and Graham Wilson. Lastly, I extend a special thank you to Erin Louise Fitzpatrick for always being there for me.

One thing we did learn throughout the course of this journey, it was “good times...to be had by all”.

## Table of Contents

<b>Approval .....</b>	<b>ii</b>
<b>Abstract.....</b>	<b>iii</b>
<b>Dedication .....</b>	<b>v</b>
<b>Acknowledgments .....</b>	<b>vi</b>
<b>Table of Contents .....</b>	<b>vii</b>
<b>List of Figures.....</b>	<b>x</b>
<b>List of Tables .....</b>	<b>xii</b>
<b>Chapter 1 Introduction .....</b>	<b>1</b>
1.1 – Objective and Motivation .....	2
1.2 – Related Work .....	4
1.3 – Thesis Layout .....	6
1.4 – Thesis Contributions .....	7
<b>Chapter 2 Background Material and the Modeling Approach .....</b>	<b>9</b>
2.1 – Assumptions .....	9
2.2 – Nomenclature .....	10
2.3 – Quasi-Static Motion.....	11
2.4 – Coulomb Friction.....	11
2.5 – Pressure Distribution .....	11
2.6 – Mason's Voting Theorem .....	12
2.7 – Center of Rotation (COR) – Peshkin and Sanderson.....	14
2.8 – COR Locus .....	15
2.9 – COR Locus Without Contact Friction.....	16
2.10 – COR Locus With Contact Friction ( $\mu_c$ ) .....	17
2.10.1 – Sticking and Slipping Zones .....	18
2.10.2 – Slipping Locus .....	19
2.10.3 – Sticking Locus .....	19
2.11 – Normal Pressure Distribution Assumption .....	21
2.12 – Minimum Power Mechanics .....	21
2.13 – Contact Parameter .....	22
2.14 – Finding the Point of Contact.....	23
2.15 – Relative Motion of the Part Against the Pin .....	25

2.16 – Estimating the COR Using Minimum Power Mechanics.....	27
2.17 – Configuration Maps .....	31
2.18 – Stable Equilibrium States .....	33
<b>Chapter 3 Configuration Maps Using Overhead Pins .....</b>	<b>35</b>
3.1 – Static Passive Simulation Results .....	35
3.1.1 – Motion of Polygonal Part.....	36
3.1.2 – Configuration Maps .....	38
3.1.2.1 – Instances of No-Contact (NC) with Pin .....	40
3.2 – Static Passive Experimental Results .....	40
3.3 – Bands' Interval Widths .....	42
3.3.1 – Comparing Simulation Against Experimental Band Intervals.....	45
3.4 – Adjusting the Bands' Interval Widths .....	47
3.5 – Effects of Friction .....	48
3.5.1 – Surface Friction .....	48
3.5.2 – Contact Friction .....	50
3.6 – Discussion and Conclusions .....	50
<b>Chapter 4 Planning .....</b>	<b>52</b>
4.1 – Planning with Configuration Maps.....	53
4.1.1 – Complications due to COM Positioning and the Contact Parameter .....	55
4.1.2 – Reducing the Random Initial Configurations .....	56
4.2 – The Search Tree.....	57
4.2.1 – The “Moving” Pins Method: Following Peshkin and Sanderson's Approach .....	57
4.2.2 – The “Fixed Pins” Method .....	59
4.2.2.1 – Expanding the Trees .....	61
4.2.3 – Searching for a Solution .....	64
4.2.3.1 – Defining the Solution .....	64
4.2.3.2 – Searching by Backtracking .....	65
4.3 – Planning Results .....	67
4.3.1 – Successful Results .....	68
4.3.2 – Partial Results .....	69
4.3.3 – Experimental Trials .....	70
4.4 – Discussion and Conclusions .....	71
<b>Chapter 5 Introducing the Force/Torque Sensor .....</b>	<b>73</b>
5.1 – Purpose and Approach.....	73
5.2 – Force/Torque Profiles.....	75
5.2.1 – Approximating the Direction of Force.....	76
5.2.2 – Expectations due to Contact Interaction .....	77
5.3 – Static Active Simulation Results .....	78



5.4 – Static Active Experimental Results .....	80
5.5 – Simulation vs. Experimental F/T Profiles Comparison .....	81
5.5.1 – Indistinguishable Orientation States .....	88
5.6 – Planning with F/T Sensor.....	90
5.7 – Vertex/Edge Contact Detection .....	91
5.7.1 – Experiment.....	93
5.7.2 – Detection Method .....	93
5.7.3 – Results .....	96
5.8 – Discussion and Conclusions .....	96
Chapter 6 Conclusions and Future Work .....	98
6.1 – Conclusions .....	98
6.2 – Future Work .....	100
Appendix A Nelder-Mead Simplex Algorithm.....	104
Appendix B Finite Element Methods for Integration.....	108
Appendix C Force/Torque Sensor Specifications .....	116
Appendix D Simple Moving Averages and The Least Squares Method.....	117
D1 – Simple Moving Averages.....	117
D2 – Least Squares Method.....	119
Appendix E Dynamic Pins.....	121
E1 – Motion Modeling using Dynamic Pins .....	121
E2 – Preliminary Results .....	123
Appendix F Timing Throughout Contact.....	127
Appendix G Preliminary Work Toward the Design of the Hybrid Gravity Part Orienter (HGPO) .....	132
G1 – Modeling.....	133
G1.1 – Rotation About a Fixed Pin .....	136
G1.2 – Rotation and Sliding .....	138
G2 – Simulation Results .....	139
G3 – Experimental Results .....	143
G4 –Conclusions and Future Work Recommendations.....	144
Bibliography .....	146

## List of Figures

Figure 1-1	Orienting parts from unknown initial to final unique configuration. ....	2
Figure 1-2	(a) Overhead pin classes and (b) Fence contact vs. Pin Contact .....	4
Figure 1-3	Orienting with overhead pins: the concept. ....	4
Figure 2-1	Triangular polygon in (a) with cross-sectional area $A$ and its corresponding weight $Mg$ .....	12
Figure 2-2	Mason's Voting Theorem exemplified.....	14
Figure 2-3	Instantaneous center of rotation .....	15
Figure 2-4	(a) COR locus for the case with $\mu_c = 0$ . (b) Triangular polygon being pushed.....	17
Figure 2-5	Object showing components of applied force upon contacting the pin.....	18
Figure 2-6	Construction of Slipping Zones and relative directions of slip. ....	20
Figure 2-7	Slipping and sticking locus. ....	20
Figure 2-8	(a) Pin and COM distance. (b) Positive and negative $d$ . ....	23
Figure 2-9	Determining point of contact geometrically.....	25
Figure 2-10	Relative motion of polygonal part against stationary point obstacle .....	26
Figure 2-11	(a) Maintaining contact between part and pin after rotating polygon by $\delta\theta$ .....	27
Figure 2-12	COR locus tip locations during slipping and sticking.....	29
Figure 2-13	Determining the instantaneous COR using minimum power mechanic.....	30
Figure 2-14	Typical configuration map. ....	31
Figure 2-15	Triangular polygons: (a) TriPoly1 and (b) TriPoly2.....	34
Figure 3-1	Comparison of TriPoly1 motion against point obstacle (i.e. overhead pin). ....	37
Figure 3-2	Experimental trial for triangular polygon (TriPoly1) starting at $\theta_i = 30.00^\circ$ .....	38
Figure 3-3	Configuration maps for given $d$ values, using the $r_{tip}$ as COR in (a-c), minimized $E_r$ .....	39
Figure 3-4	Passive pin experimental setup. ....	41
Figure 3-5	Variation in final angles $\theta_f$ resulting in band intervals for TriPoly1.....	43
Figure 3-6	Band intervals vs. contact parameter plot. ....	44
Figure 3-7	Experimental band interval vs. contact parameter plot. ....	45
Figure 3-8	Adjusted band intervals vs. contact parameter . ....	48
Figure 4-1	(Copy of Figure 1-1) Orienting parts from unknown initial to final unique configuration. ....	52
Figure 4-2	(Copy of Figure 1-3) Orienting with overhead pins: the concept. ....	53
Figure 4-3	Illustration of orienting with fences, where random initial orientations are reduced .....	54
Figure 4-4	Sample illustration of map combination as described in expression (4-1) .....	54
Figure 4-5	Curved fence used to reduce the part's initial random orientations.....	56
Figure 4-6	Combining initial states of polygon TriPoly2.....	57
Figure 4-7	Tree expansion illustrating the adaptation of Peshkin and Sanderson's method .....	58
Figure 4-8	Referencing the pins from the "New Reference Line" for all states .....	59
Figure 4-9	Combined tree after expanding separately for each initial state .....	60
Figure 4-10	Initial states for triangular polygon and fixed global pins. ....	61
Figure 4-11	Bounding the COM region to select pins resulting from the range of $\theta_f$ orientations .....	62
Figure 4-12	Combination of configuration maps $M_1$ and $M_2$ given an initial state of $\theta_i$ .....	64
Figure 4-13	Combination of configuration maps $M_1$ and $M_2$ given an initial state of $\theta_i$ .....	65
Figure 4-14	Expanded tree showing selected (shaded) nodes after backtracking.....	67
Figure 4-15	Pin sequence used to orient TriPoly2 from its three initial states to a final orientation .....	68
Figure 4-16	Pin sequence orienting symmetric triangular polygon TriPoly1 .....	69
Figure 5-1	Applied force $F$ resulting from part contacting pin with sensor .....	74
Figure 5-2	Side-view schematics of pin without sensor in (a) and with F/T sensor in (b).....	75

Figure 5-3	Approximated direction of applied force at the point of contact .....	77
Figure 5-4	(a) Motion of part against pin. (b) Snapshots of part motion .....	78
Figure 5-5	Simulation force/torque profiles for TriPoly1 ( $\theta_i = 0^\circ$ and $d = -0.2$ ) .....	79
Figure 5-6	Experimental setup using the F/T sensor on the static pin. ....	81
Figure 5-7	F/T profiles from raw experimental data ( $\theta_i = 0^\circ$ and $d = -0.2$ ) .....	82
Figure 5-8	Smoothed F/T profiles from experimental data ( $\theta_i = 0^\circ$ and $d = -0.2$ ) .....	83
Figure 5-9	Force profiles and fitted cubic polynomials for simulation (a,c) and experimental (b,d) .....	84
Figure 5-10	Selected five regions in force profiles used to evaluate curve trends .....	85
Figure 5-11	Contact configuration similarities between Initial States 1 and 2 for TriPoly1. ....	89
Figure 5-12	Similar $F_x$ and $F_y$ profiles for $\theta_i = 0^\circ$ and $\theta_i = 135^\circ$ .....	89
Figure 5-13	Contact configuration similarities between final orientation sets 1 and 2 for TriPoly1 .....	90
Figure 5-14	Vertex contact plots for TriPoly2 ( $\theta_i = 0^\circ$ ). (a) shows the spike in the x-dir force .....	95
Figure 6-1	Dynamic pins, as first illustrated in Chapter 1, capable of moving perpendicularly .....	101
Figure 6-2	Polygonal part at initial contact ( $t = t_i$ ) and at the end of the contact period ( $t = t_f$ ) .....	102
Figure 6-3	Notion of proposed dynamic environment setup .....	103
Figure A-1	Two-dimensional simplex. ....	104
Figure B-1	Arbitrary area in xy-plane showing limits of integration. ....	109
Figure B-2	Transformation from arbitrary triangle to standard triangle. ....	110
Figure B-3	Transformation from regularized triangle to regularized rectangle. ....	112
Figure E-1	(a) Combined conveyor and pin motions, (b) push due to conveyor motion .....	122
Figure E-2	Motion of TriPoly1 against a static pin - remains in Orientation1 .....	123
Figure E-3	Motion of TriPoly1 due to dynamic pin: $\theta_i = 15^\circ \rightarrow \theta_f = 163.2^\circ$ .....	124
Figure E-4	Motion of TriPoly1 against a static pin - remains in Orientation2. ....	125
Figure E-5	Motion of TriPoly1 due to dynamic pin: $\theta_i = 160^\circ \rightarrow \theta_f = 297.5^\circ$ .....	126
Figure F-1	TriPoly1 in its three initial states ( $0^\circ$ , $135^\circ$ and $225^\circ$ ) with pins .....	129
Figure F-2	TriPoly2 in its three initial states ( $0^\circ$ , $90^\circ$ and $206^\circ$ ) with pins .....	130
Figure G-1	Setup of passive pin arrangement with coordinate frames and possible events .....	134
Figure G-2	FBD of triangular polygon experiencing pure rotation against pin. ....	136
Figure G-3	FBD of triangular polygon experiencing rotation and slip against pin .....	138
Figure G-4	Polygon rotating, sliding and free falling about a pin with edge .....	140
Figure G-5	Phase changes illustrated by polygon rotating, sliding and free falling .....	142
Figure G-6	Picture of experimental test-bed for HGPO. ....	143

## List of Tables

<i>Table 2-1 Nomenclature of most common terms used in this thesis.....</i>	<i>10</i>
<i>Table 2-2 Voting summary for rotation sense illustrated in Figure 2-2(a-c).....</i>	<i>14</i>
<i>Table 3-1 Comparison of interval widths, Simulation vs. Experimental.....</i>	<i>46</i>
<i>Table 3-2 Comparison of interval widths, Adjusted vs. Experimental.....</i>	<i>49</i>
<i>Table 3-3 Effects of varying the friction coefficient at the surface interface. ....</i>	<i>49</i>
<i>Table 3-4 Effects of varying the coefficient friction at the point of contact. ....</i>	<i>50</i>
<i>Table 4-1 Pin sequences experimental results .....</i>	<i>70</i>
<i>Table 5-1 Experimental vs. Simulation matrix matching comparison .....</i>	<i>86</i>
<i>Table 5-2 Comparison of matching scores from force/torque profiles .....</i>	<i>87</i>
<i>Table 5-3 Pin sequence for TriPoly1 yielding Final Orientations 1 and 2.....</i>	<i>91</i>
<i>Table 5-4 Vertex/edge contact detection results .....</i>	<i>96</i>
<i>Table C-1 Specifications for Nano Force/Torque sensor model FT3629. ....</i>	<i>116</i>
<i>Table D-1 Sample data depicting the simple moving averages method.....</i>	<i>118</i>
<i>Table F-1 Partial timing results throughout period of contact between part TriPoly1 and the pin .....</i>	<i>128</i>
<i>Table F-2 Partial timing results throughout period of contact between part TriPoly2 and the pin. ....</i>	<i>130</i>
<i>Table G-1 Possible events per pin (refer to Figure G-1) .....</i>	<i>135</i>

# Chapter 1

## Introduction

The manufacturing field is one in which speed and volume throughput of assembly parts play a dominant role. Further, *flexible* manufacturing refers to an aspect of manufacturing where the parts being moved and assembled can vary on short notice, and it is imperative that the process and assembly lines continue to move without a great deal of disruption. Moreover, *holonic* manufacturing refers to a flexible manufacturing system where self-contained entities or agents “*organize themselves without the power of an external force*” [9]. The term holon was proposed by the philosopher Arthur Koestler who identified that “*wholes*” and “*parts*” in their absolute sense, where a “*whole*” is seen as something complete in itself, and a “*part*” refers to something fragmentary and incomplete, just do not exist anywhere [11]. Thus, a *holon* refers to every identifiable unit of organization that comprises more basic units while at the same time forms a part of a larger unit of organization. In the grand scheme of things, our work comprises a small fragment within the realm of flexible and holonic manufacturing where various classes of overhead pins acting as agents later defined are used in collaboration with one another towards a common goal, that of polygonal part orienting.

In a holonic system, agents continuously exchange information and collaborate with each other towards a solution. In this thesis, pins are first studied as individual agents to understand the interaction between a given moving part and the pin it comes into contact with. Later, sequences of pins are found to orient the part; hence, each pin sequentially contributing towards the common goal behaving as a multi-agent system. Note however though, that no information will be exchanged between agents (i.e. overhead pins) in this study. Further work will be necessary to create a holonic system.

Orienting parts refers to aligning a batch of parts to be assembled in a desired or unique configuration from an unknown initial configuration as illustrated in Figure 1-1 through a speculated system here depicted by a “black box”. It is one of the early stages within the manufacturing process, and generally, it is this step that becomes the bottleneck of the process [22]. The most common feeder used in manufacturing is the vibratory bowl feeder; however, the biggest drawback with this feeder is its lack of flexibility, wherein flexibility refers to “*the ability to change a variety of parameters of the manufacturing process in response to business needs*” [26]. Therefore, the long term goal of part orienting research is the design and development of flexible part feeders capable of orienting various different parts on demand without the need to redesign the system. Instead, for each new part, a model (e.g. CAD) of the part defining its geometry is provided to the part orienting system, and based on the resulting part's mechanics and interaction with the system's environment the system “adapts” to orient the new given part.

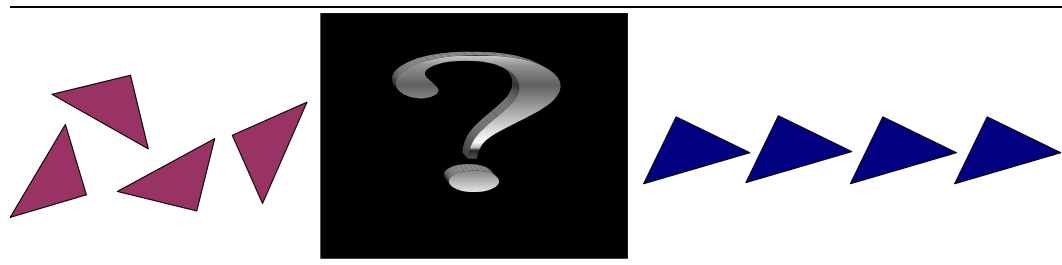


**Figure 1-1 Orienting parts from unknown initial to final unique configuration.**

## 1.1 – Objective and Motivation

This thesis sets out to introduce aspects of an innovative method towards the development of a hybrid part feeder. Hybrid refers to something that has two or more different types of components performing the same function. Here, the notion of a multi-agent hybrid system is explored through application and usage of *overhead pins* of

various classes. Pins of various classes are, more specifically, pins with and without sensors, as well as stationary and moving pins, and combinations of these (see Figure 1-2(a)), that are utilized over a slow moving conveyor to orient polygonal planar parts.

The motivation for the use of pins is tied to the principle of minimalism, which refers to the simplest and minimal interaction between the orienting device and the part to be oriented. Unlike fences that are used for the same orienting purpose, pins do not rely on multiple point contact as it occurs between the fence and the part, but instead the focus lies on a single point contact between the part and the pin at all times throughout the period of interaction as illustrated in Figure 1-2(b). Thus, the main advantage that can be cited for the use of pins is the shorter necessary setup within the assembly line in comparison to fences. Ideally, if the two systems (pins vs. fences) are equivalently capable, using fences generally require long setups taking up much needed space within the manufacturing floor. Similar setups using overhead pins would require less space hence freeing floor space for other events. Furthermore, because of the resulting shorter setup, for a conveyor belt moving at slow constant speed, the process of part orienting would be completed faster through a sequence of pins than through a sequence of fences. Thereby reducing the time necessary for the part orienting stage throughout the assembly process and proving to be more efficient than fences.

Finally, the concept of orienting with overhead pins is illustrated in Figure 1-3 where a triangular polygon traverses a sequence of static pins without sensors as it travels on a slow moving conveyor belt along the indicated direction. Given the geometry of the polygon, the amount of rotation and translation that will result against each pin will depend on numerous factors such as the initial orientation of the part, the amount friction at the point of contact and the distance between the part's center of mass (COM) and the pin. The layout of the pins must be such that no multiple contact may occur between the part and the pins at all times.

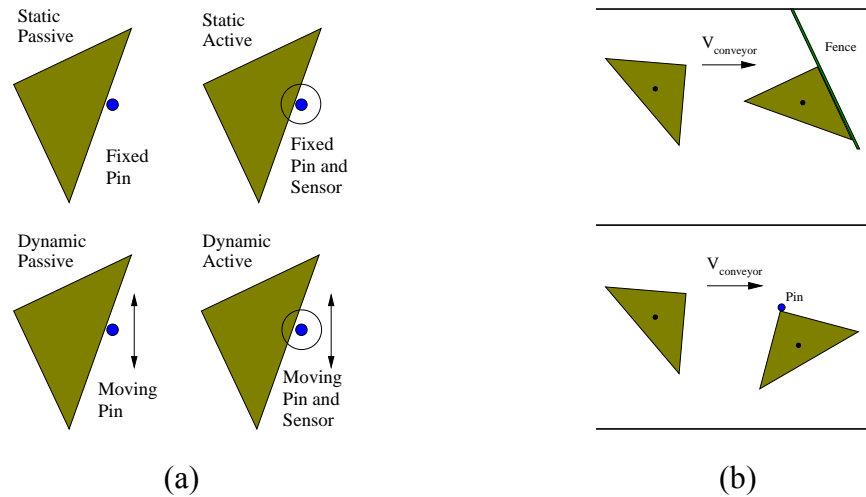


**Figure 1-2 (a) Overhead pin classes and (b) Fence contact vs. Pin Contact**

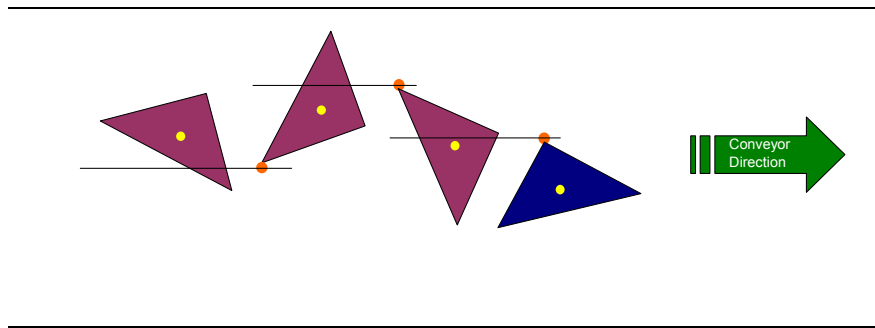


**Figure 1-3 Orienting with overhead pins: the concept.**

## 1.2 – Related Work

The notion of orienting parts over a conveyor belt using fences was first presented by Peshkin and Sanderson in [18]. They introduced the use of configuration maps that encapsulate the physics of an operation such as a part contacting a fence, where the horizontal axis gives the initial orientation prior to contact and the vertical axis gives the final orientation at the end of contact of the part with the fence. Using these maps representing the orienting effect of fences, operation sequences were defined to orient given parts through planning searches.

Other work for orienting with fences include that of Akella and Mason in [1] and [2]. In [1] they investigated the use of partial sensor information alongside mechanical



operations (i.e. push-align operations) to reduce uncertainty in part orienting thereby demonstrating the advantages of sensor-based orienting. Then, in [2] they presented a shape uncertainty model used to generate orienting plans to orient a class of polygonal shapes with and without sensors given the non-determinism that arises from a polygon's shape uncertainty. In general, part orienting methods must be robust enough to allow for uncertainties arising from slight variations in the geometry of a part.

A limitation of orienting with fences is that once the part exits the fence its final orientation is confined to a narrow range of possible orientations but is not unique, consequently, Brokowski, Peshkin, and Goldberg in [7] added curved sections to the ends of fences to reduce uncertainty in the outcome and guarantee unique orientations. Moreover, Rusaw, Gupta, and Payandeh [21] examined the effect of uncertainty in the coefficient of friction and its effect on the typical size of the final assembly, and later [22] incorporated a force/torque sensor to determine the orientation of a polygon on a horizontal surface by pushing with a sensor equipped fence. In addition, Salvarinov and Payandeh in [23] manipulated parts using an active fence with embedded sensory system.

Later, Akella, Huang, Lynch, and Mason [3] reduced the orienting problem to planning manipulations with a single rotational fence using a robot with just one joint, referred to as the 1JOC (1-joint over conveyor). Then, Lynch in [16] in the spirit of minimalism, utilized toppling as a manipulation primitive which in combination with previous works orienting planar parts permits parts feeding of 3D objects on a conveyor with a 2 joint robot.

Orienting with fences has the advantage that they guarantee that the part will rotate and slide onto one of its natural resting edges as long as the fence is long enough for this motion to occur [17],[18]. On the other hand, orienting with pins cannot take advantage of the part's stable edges in the same manner. Thus, the behaviour of the part to be oriented as it comes into contact with a stationary pin (Figure 1-1(b)) must be understood, and consequently the actual motion of the part approximated.

In addition, previous work using pins for part orienting include Zhang, Smith, Berretty, Overmars and Goldberg in [28] where a sensorless approach to feeding parts on a conveyor belt is presented using pins that serve as rigid barriers in order to topple parts into desired orientations. On the other hand, Blind, McCullough, Akella, and Ponce in [5] addressed the problem of manipulating polygonal parts with a device consisting of a grid of retractable pins mounted on a vertical plate. When a part is dropped on this device, it may come to rest on two or three of the actuated pins, thereby capturing the part, or bounce out or fall through. Sequences of pin actuations and retractions that bring the part to a goal configuration are computed. More recently, Berretty, Goldberg, Overmars, and van der Stappen in [4] used pins without sensors as overhead fingers to orient a distinct class of polygonal parts, asymmetrical parts with elevated edges, by inside-out pulling. And finally, amongst other works in part orienting, Zhang and Gupta in [29] proposed an algorithm for sensorless reorientation of 3D convex polyhedral parts through a sequence of step devices.

### **1.3 – Thesis Layout**

The layout for the remainder of the thesis is as follows: Chapter 2 outlines the relevant background theory on which most of the work presented is built on. This material is repeatedly used throughout the entirety of the thesis. Here, the approach used to model the motion of the polygonal part is also described.

Chapter 3 presents the part's motion results describing the interaction of a planar polygonal part with a stationary overhead pin over a slow moving conveyor belt. In this chapter, the configuration maps used later in the planning process in Chapter 4 are created and compared against the experimental results.

Chapter 4 outlines the planning method used to search for a sequence of overhead pins to orient the given polygonal part from a set of initial states to a final orientation.

Chapter 5 introduces the use of the force/torque (F/T) sensor first used to complement the planning search in cases where a single final orientation is not found due to symmetries present in the geometry of the part and outlines the results obtained. In addition, the F/T sensor is used to distinguish between vertex and edge contact with the pin.

Chapter 6 offers conclusions to the work presented, and outlines the future work to be done as a continuation of this exploratory study.

## **1.4 – Thesis Contributions**

As a contribution to the part orienting research community, the work in this thesis, introduces the novel idea of using overhead pins to orient planar polygonal parts on a slow moving conveyor belt.

First, the motion of a polygonal part forced by a point pusher (or a point obstacle) as described by Peshkin and Sanderson [17] is revisited. Using the assumption of a constant and even pressure distribution as well as known contact friction, the actual motion of a polygonal part is approximated using minimum power mechanics [17],[19]. Thereby, successfully creating configuration maps for the first time that closely describe the part's interaction with an overhead pin.

Then, a simple “brute-force” planner, referred to as the “Fixed-Pins” method, that yields sequences of static passive pins to orient the part from a random initial state to a final orientation set is presented. Due to the initial uncertainty in the part's configuration, a similar method to that presented in [18] could not be applied, and hence, an alternative method was needed. Although the Fixed-Pins method comes with certain limitations, it provides a solution to the problem of part orienting using overhead pins.

Finally, a force/torque sensor is incorporated to compliment the planning process whereby using an empirical method, the initial states of the given polygonal part are identified or the set reduced; hence, helping to identify the final orientation in the cases

where a single final orientation is not found. Moreover, the sensor is used to distinguish between vertex and edge contact again using an empirical method. This investigation is carried out with the notion that in future work we may be able to identify states where a part traversing through a selected pin sequence might fail to arrive at the expected orientation due to unexpected motion caused by the pin “catching” the part's vertex.

Overall, the contributions presented in this thesis are intended as an exploratory study towards the future design and development of a more complete mechanics-based hybrid part feeder. Where in terms of holonic manufacturing the objective of part manipulation is accomplished by the use of a distributed multi-agent system such as that of overhead pins of various classes. These contributions are examined in the chapters to follow.

## Chapter 2

# Background Material and the Modeling Approach

This chapter presents the necessary background material pertaining to the quasi-static motion of a polygonal part traveling on a slow moving conveyor and contacting a stationary overhead pin, and outlines the approach used to model the motion of the part. Also in this chapter, the material used for the part orienting process is introduced.

### *A. Background Material*

Throughout the study of the part's motion against a stationary point obstacle, the assumptions below are used. These assumptions also apply to the orienting techniques presented in the chapters to follow.

#### **2.1 – Assumptions**

1. Motion is quasi-static (slow moving conveyor).
2. Friction is modeled as Coulomb friction at all interactions.
3. Coefficient of friction  $\mu_s$  over the sliding surface is constant.
4. Coefficient of friction  $\mu_c$  at the point of contact between the part and the pin is known and constant throughout the period of contact.
5. Parts are polyhedral of constant polygonal cross sectional area.
6. Pressure distribution is constant and uniform over the entire cross sectional area of the polygonal part, and it is assumed to be known.
7. The objects and pins are rigid.
8. Locations of the part vertices and center of mass (COM) are known.

## 2.2 – Nomenclature

Table 2-1 in this section outlines and defines some of the most used terms in this thesis.

**Table 2-1 Nomenclature of most common terms used in this thesis.**

$A$	• Cross sectional area of polygon.
$Mg$	• Weight of polygon, where $M$ is the mass and $g$ is the gravity constant.
$V_{conveyor}$	• Unit vector indicating direction of conveyor belt motion.
COM	• Center of Mass of polygon.
COR	• Center of Rotation
$\delta X$	• Infinitesimal amount of displacement of polygon.
$\delta \theta$	• Infinitesimal amount of rotation of polygon.
$\vec{w}$	• Arbitrary point in the area $A$ of polygon.
$P(\vec{w})$	• Pressure distribution of polygon for all points $\vec{w}$ on the polygon.
$P_w$	• Constant pressure distribution term.
$P$	• “Push” by pin acting on the polygon.
$\alpha$	• Magnitude of angle of edge in contact with the pin.
$\vec{\alpha}$	• Unit vector indicating angle of edge in contact with the pin.
$\vec{F}$	• Force applied on the pin by the part.
$\vec{c}$	• Vector between point of contact and center of mass.
$\vec{r}$	• Vector between center of mass and center of rotation.
$\theta_i$	• Initial orientation of polygon prior to contact with pin.
$\theta_f$	• Final orientation of polygon after contact with pin.
$\mu_c$	• Coefficient of friction at the point of contact.
$\mu_s$	• Coefficient of friction at the sliding surface interface.
$\vec{f}_{right}$	• Right bound of friction cone from normal (also referred to as $\vec{f}_{down}$ ).
$\vec{f}_{left}$	• Left bound of friction cone from normal (also referred to as $\vec{f}_{up}$ ).
$v$	• Half angle of friction cone.
$d$	• <i>Contact parameter</i> : perpendicular distance between COM and pin.
$B_j$	• Range of final orientation angles for a given $j$ .
$K_j$	• Range of initial orientation angle for a given $j$ .
$COM_j$	• Range of final COM positions for a given $j$ .

### 2.3– Quasi-Static Motion

Quasi-static motion refers to the slow motion approximation where frictional forces dominate over the inertial forces and quickly dissipate any kinetic energy of the part,

$$V^2 \ll Xg\mu_s \quad (2-1)$$

where  $V$  is the velocity of the part,  $g$  is the acceleration due to gravity and  $X$  refers to the distance the part travels over its supporting surface [17].

### 2.4 – Coulomb Friction

Coulomb friction is independent of normal force magnitude, tangential force magnitude, direction and velocity [17]. Further, no distinction is made between “static” and “dynamic” friction in this study, and it is assumed that the coefficient of friction of the part with the supporting surface,  $\mu_s$ , is known and constant over the surface. When using a simple model of friction such as Coulomb friction, Peshkin and Sanderson acknowledged in [17] that  $\mu_s$  does not affect the motion of the part. Thus, by using Coulomb friction as the model of friction in this study, it is assumed that the motion of any given part over the conveyor belt is not affected by the sliding friction coefficient  $\mu_s$  at the sliding interface between the conveyor belt and the part.

On the other hand, the other coefficient of friction in the problem which does affect the motion of the part is that at the point of contact between the part and the pin,  $\mu_c$ . Here, it is assumed that  $\mu_c$  is known and constant throughout the period of contact under the Coulomb friction model.

### 2.5 – Pressure Distribution

The pressure distribution refers to the amount of pressure  $P(\vec{w})$  an object exerts on its supporting surface due to the object's weight and how it is distributed over the area  $A$  on which the object rests. This notion is defined as follows:

$$\int_A P(\vec{w}) d\vec{w} = Mg \quad (2-2)$$

where  $\vec{w}$  is a point in the area  $A$  of the object, and  $Mg$  is the weight of the object, also illustrated in Figure 2-1.

The weight of a polygonal part is sustained by a set of points that bear the total normal force  $N$  due to the weight of the part between the part and its supporting surface. As the part moves on the surface, the pressure distribution may change due to irregularities at the supporting interface, such as irregularities in flatness, dust and part irregularities. However, for the purpose of investigating the motion of planar parts against a point obstacle a constant and uniform pressure distribution is assumed in this study. Thus any minor irregularities between the surface and the part such as dust are discarded.

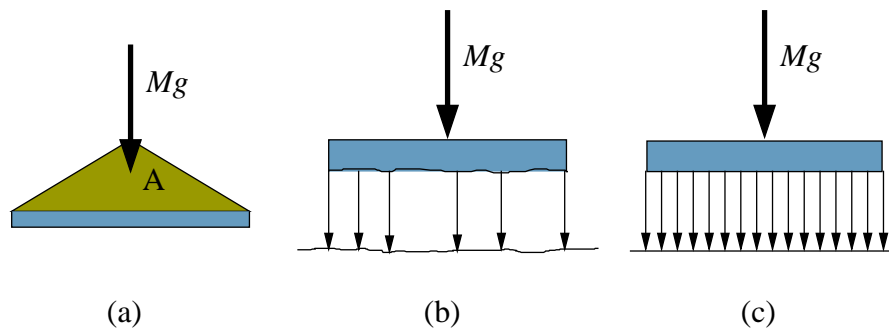


**Figure 2-1** Triangular polygon in (a) with cross-sectional area  $A$  and its corresponding weight  $Mg$ . (b) Shows the weight the polygon's weight  $Mg$  unevenly distributed and sustained by a set of points due to uneven rough supporting surface and part's bottom surface while (c) shows the same weight  $Mg$  evenly distributed over the entire cross-sectional area  $A$  due to a smooth and even surface interface.

## 2.6– Mason's Voting Theorem

A part's motion is dependent on the applied force and the frictional forces  $f_s = \mu_s N$  at the sliding surface opposing the part's motion. Further, according to the Coulomb's friction model, these frictional forces are related to the pressure distribution between the object and its supporting surface [22]. However, in general, as an object is pushed,



neither the direction or magnitude of the applied force, nor the part's pressure distribution are known, and thus, the part's motion is deemed unknown.

Subsequently, Mason developed a rule to determine the *rotation sense* of an object acted upon by an external force such as pushing [22]. This rule is solely based on the location of the center of mass (COM) of the object and is independent of the pressure distribution, frictional forces and normal force between the part and the sliding surface. Thus, although, the object's exact motion is not known, Mason showed that the *rotation sense* (i.e. counterclockwise, CCW or clockwise, CW) can be determined based on the contact configuration. Where the contact configuration refers to the initial orientation and position of the part with respect to the pusher prior to contact with it as well as the contact friction coefficient  $\mu_c$ .

To obtain the rotation sense, the theorem relies on three “votes” resulting from three comparisons between specified vector pairs. The vectors compared are the direction of push or for the case of the moving object, the opposing direction of conveyor belt motion  $-V_{conveyor}$ , the vector from the point of contact to the COM  $\vec{c}$ , and both extremes of the friction cone  $\vec{f}_{left}$  and  $\vec{f}_{right}$  as illustrated in Figure 2-2(a-c). Each vote evolves from taking the cross product of  $-V_{conveyor}$ ,  $\vec{f}_{left}$ , and  $\vec{f}_{right}$  with  $\vec{c}$ . Using standard Cartesian nomenclature CCW or CW results are obtained (see Figure 2-2(a-c) and Table 2-2), and hence, the *sense of rotation* is dictated by the majority of CCW or CW votes.

A tie is possible whenever  $V_{conveyor} \parallel \vec{c}$  and the other two votes are opposite to each other. This tie indicates a metastable push, which says that ideally the object will not rotate unless disturbed by another external force and its resulting direction of rotation cannot be predicted. In the work of this thesis, this singularity of a tie indicating metastable pushing is avoided due to the random nature of the part's rotation and its unpredictable motion. Figure 2-2(a-c) illustrates the rotation sense cases described

above. Furthermore, the corresponding votes that yield the rotation sense results in Figure 2-2(a-c) are tabulated below in Table 2-2 to exemplify Mason's Voting Theorem.

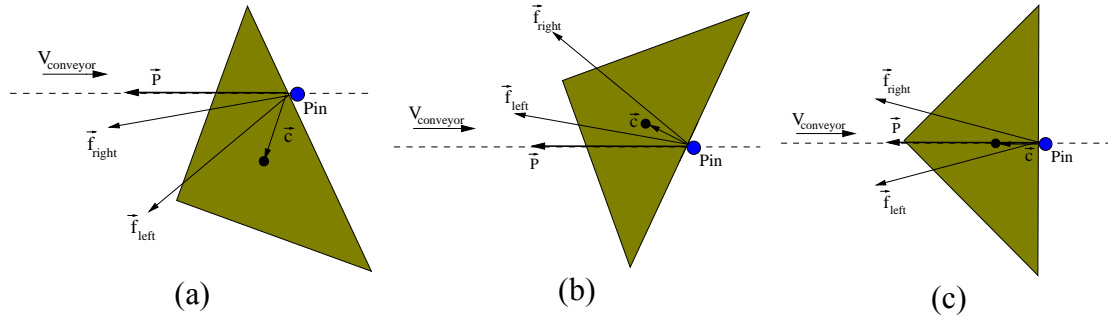


**Figure 2-2 Mason's Voting Theorem exemplified: (a) results in a CCW rotation, (b) results in a CW rotation and (c) results in a tie, implying a metastable state.**

**Table 2-2 Voting summary for rotation sense illustrated in Figure 2-2(a-c)**

For Figure 2-2 (a):	For Figure 2-2 (b):	For Figure 2-2 (c):
$vote1 = \text{sign}(-V_{conveyor} \times \vec{C})$ = +1	$vote1 = \text{sign}(-V_{conveyor} \times \vec{C})$ = -1	$vote1 = \text{sign}(-V_{conveyor} \times \vec{C})$ = 0
$vote2 = \text{sign}(\vec{f}_{left} \times \vec{C})$ = +1	$vote2 = \text{sign}(\vec{f}_{left} \times \vec{C})$ = -1	$vote2 = \text{sign}(\vec{f}_{left} \times \vec{C})$ = -1
$vote3 = \text{sign}(\vec{f}_{right} \times \vec{C})$ = +1	$vote3 = \text{sign}(\vec{f}_{right} \times \vec{C})$ = +1	$vote3 = \text{sign}(\vec{f}_{right} \times \vec{C})$ = +1
Sign of voting total = +1 Rotation sense: <b>CCW</b>	Sign of voting total: -1 Rotation sense: <b>CW</b>	Sign of voting total: 0 Rotation sense: <b>TIE</b>

## 2.7 – Center of Rotation (COR) – Peshkin and Sanderson

The center of rotation (COR) is defined as the point about which the instantaneous motion of a rotating and/or translating object can be expressed as a rotation  $\delta\theta$  about that point [22]. The COR is selected such that the instantaneous motion of each point  $\vec{w}$  in the polygon's area is perpendicular to the vector from the COR to the point  $\vec{w}$  as illustrated in Figure 2-3. It was shown in [17] that this point and hence the motion of the

part depends on the pressure distribution of the polygonal part, which is generally unknown. Consequently, they introduced the COR locus explained in the next section.

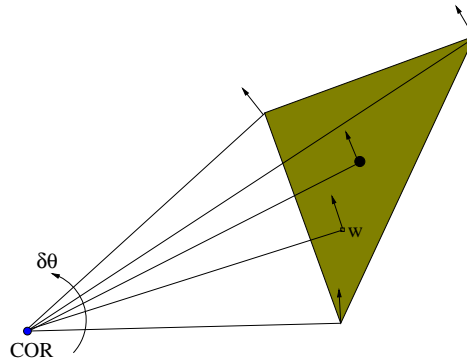


**Figure 2-3 Instantaneous center of rotation**

## 2.8 – COR Locus

Since the COR depends on the pressure distribution of the polygonal part being studied, Peshkin and Sanderson in [17] determined the instantaneous CORs for all possible pressure distributions for a given contact configuration given the geometry of the polygonal part. The result is the COR locus, the “teardrop” bounded area shown in Figure 2-4, containing the set of all possible instantaneous CORs.

Of particular interest in Figure 2-4(a) is the tip of the locus ( $r_{tip}$ ). This point represents the slowest possible rotation of the part regardless of the pressure distribution because it is the furthest point on the locus. For the same displacement  $\delta X$  of any point  $\vec{w}$  on the part, the resultant amount of rotation  $\delta\theta$  about the locus tip is less than for any other point of rotation in the locus as illustrated in Figure 2-4(b,c). The  $r_{tip}$  is calculated as follows:

$$r_{tip} = \frac{a^2}{\vec{\alpha} \cdot \vec{c}} \quad (2-3)$$

Where  $a$  is the radius of the disc enclosing the polygon (dotted circle in Figure 2-4(a)) and also corresponds to the largest distance from the COM to any vertex on the polygon,

$\vec{\alpha}$  is the unit vector of the edge that makes contact with the pin, and  $\vec{c}$  is the vector from the pin to the COM.

The  $r_{tip}$  of the locus has been frequently used for the purpose of orienting with fences [1],[2],[3],[7],[18],[21],[27]. In [17] Peshkin and Sanderson showed the example of pushing an arbitrary object with a straight edge pusher (i.e. fence) and finding the necessary push to achieve a certain amount of rotation. In this example they used the tip of the locus as the worst case location for the COR  $\vec{r}$ , and the result was the *longest* push to achieve the desired rotation. So, in the case of parts moving along a conveyor belt and coming into contact with stationary fences, it is possible to determine the minimum length of a fence that guarantees a given part comes to rest on one of its stable edges along the fence using the COR locus tip,  $r_{tip}$ .

Unfortunately, orienting with pins cannot take advantage of modeling the part's motion using the slowest rotation about the  $r_{tip}$ , because parts turning about CORs in the rest of the locus other than the tip of the locus (Figure 2-4(c)) rotate more and translate less than the slowest turning parts rotating about the  $r_{tip}$  (Figure 2-4(b)) [7].

Consequently, the true motion of the part dependent on other COR points within the locus will be different than that that would result by modeling with the COR locus tip. A comparison is later made in Chapter 3. Thus, to orient with overhead pins it is necessary that the instantaneous CORs somewhere within the locus for each infinitesimal  $\delta\theta$  dictating the overall motion of the part be approximated and hence the behaviour of the part understood.

## 2.9 – COR Locus Without Contact Friction

For the case of zero contact friction ( $\mu_c = 0$ ) between the polygon and the pusher (i.e. pin) the applied force  $\vec{F}$  is perpendicular to the polygon's edge that contacts the pin indicated by the unit vector  $\vec{\alpha}$ . The resultant COR locus is illustrated in Figure 2-4(a) where its axis of symmetry is perpendicular to  $\vec{F}$  and parallel to  $\vec{\alpha}$ .

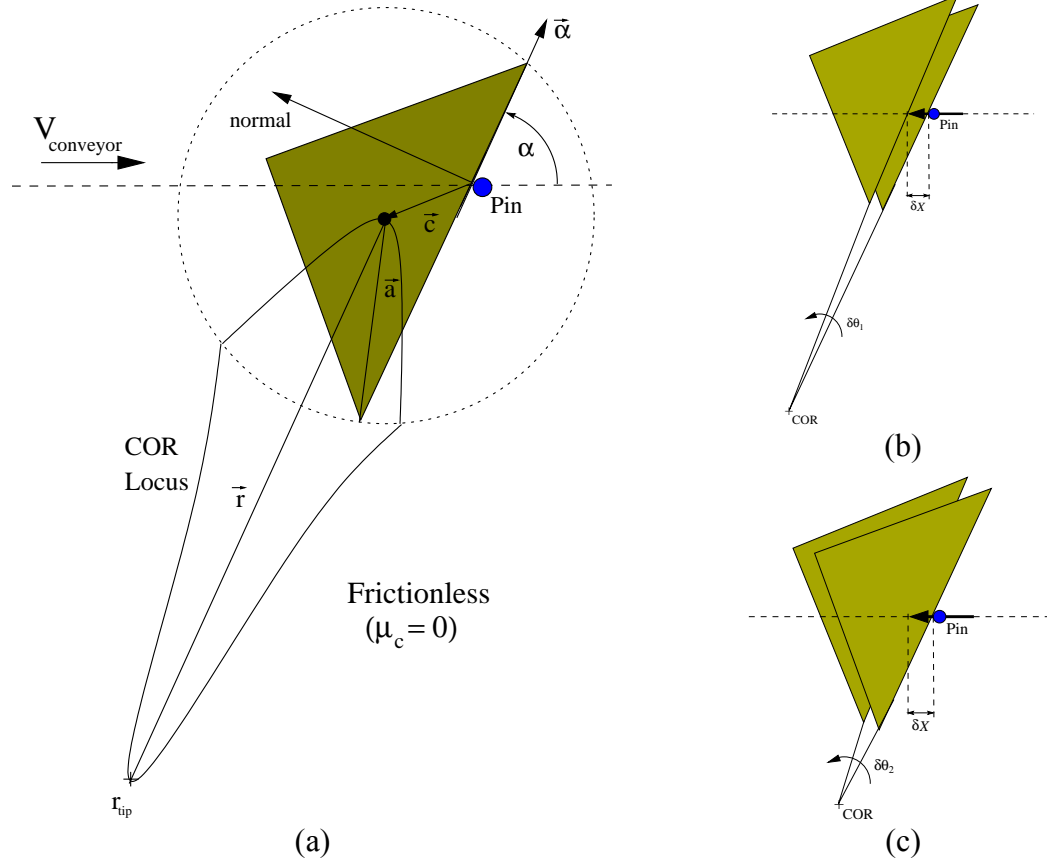


**Figure 2-4** (a) COR locus for the case with  $\mu_c = 0$ . (b) Triangular polygon being pushed a distance  $\delta X$  and rotating about the COR locus tip  $r_{tip}$  results in an amount of rotation  $\delta\theta_1$ , while in (c) the polygon rotates about other COR within the locus and rotates an amount  $\delta\theta_2$ , where for the same  $\delta X$ ,  $\delta\theta_2 > \delta\theta_1$ .

## 2.10 – COR Locus With Contact Friction ( $\mu_c$ )

For the case of non-zero contact friction ( $\mu_c > 0$ ) between the polygon and the pin, the applied force direction can lie anywhere within the friction cone. As stated in [17] and illustrated in Figure 2-5,  $F_{\parallel}$ , the component of the applied force tangential to the edge, is supported by friction, and its magnitude cannot exceed  $\mu_c F_{\perp}$ , where  $F_{\perp}$  is the normal component of force. Therefore, the total applied force must lie within the friction cone with a half angle  $\nu = \tan^{-1} \mu_c$ .

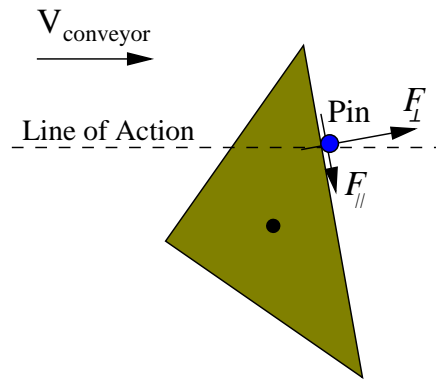


**Figure 2-5** Object showing components of applied force upon contacting the pin.

The system can depict two modes of behaviour: *sticking* and *slipping*. *Sticking* refers to when the part undergoes pure rotation, the point of contact remains the same, the edge does not slide in relation to the pin, and the applied force remains within the friction cone. *Slipping* on the other hand, refers to when the part rotates and slips in relation to the pin. The edge of the part remains in contact with the pin, but the point of contact does change, and the applied force acts along one of the friction cone extremes.

### 2.10.1– Sticking and Slipping Zones

To determine the motion of the part, the plane of motion, parallel to the sliding surface, is divided into three sections, 1) the *sticking line*, 2) the *up-slipping zone* and 3) the *down-slipping zone*. These three zones, as illustrated in Figure 2-6, dictate the three possible motion behaviours of the part. If the COR lies in the *up-slipping zone*, the polygon slips up with respect to the pin, and the relative direction of slip of a polygonal part with the pin is illustrated in Figure 2-6. Similarly, if the COR lies in the *down-slipping zone*, the polygon slips down with respect to the pin, also shown in Figure 2-6. And in comparison, if the COR lies on the *sticking line* then the point of contact does not move and sticking occurs leading to pure rotation.

### 2.10.2 – Slipping Locus

Peshkin and Sanderson give a consistency for slipping: if the part slips relative to the pin (up or down), then the direction of the force is known, it is along one extreme of the friction cone [17], perpendicular to  $\vec{\alpha}_{up}$  or  $\vec{\alpha}_{down}$  as defined in expression (2-4) and illustrated in Figure 2-6. Then, the slipping locus corresponds to the sum of the up-slipping locus and the down-slipping locus. Each constructed perpendicularly to its corresponding friction cone extreme in a “teardrop” shape as before. Where the slowest rotation for each case is given by:

$$r_{tip}^{up} = \frac{a^2}{\vec{\alpha}_{up} \cdot \vec{c}} \quad \text{and} \quad r_{tip}^{down} = \frac{a^2}{\vec{\alpha}_{down} \cdot \vec{c}} \quad (2-4)$$

where  $\vec{\alpha}_{up} = (\cos(\alpha + \nu), \sin(\alpha + \nu))$

and  $\vec{\alpha}_{down} = (\cos(\alpha - \nu), \sin(\alpha - \nu))$

Further, referring to Figure 2-6, for slipping to occur, the COR must be either in the  $\{COR\}_{\alpha-\nu}$  **and** the *down-slipping zone*, or in the  $\{COR\}_{\alpha+\nu}$  **and** the *up-slipping zone*. The sum of these two conditions yields the hatch-patterned area in Figure 2-7.

### 2.10.3– Sticking Locus

If the instantaneous COR lies on the sticking line, then sticking occurs and the applied force can be anywhere within the friction cone [17]. The sticking locus is defined as the intersection of the *sticking line* (see Figure 2-6) with the union of all the angles perpendicular to the possible direction of the applied force acting within the friction cone. The result is shown as a bold line in Figure 2-7.

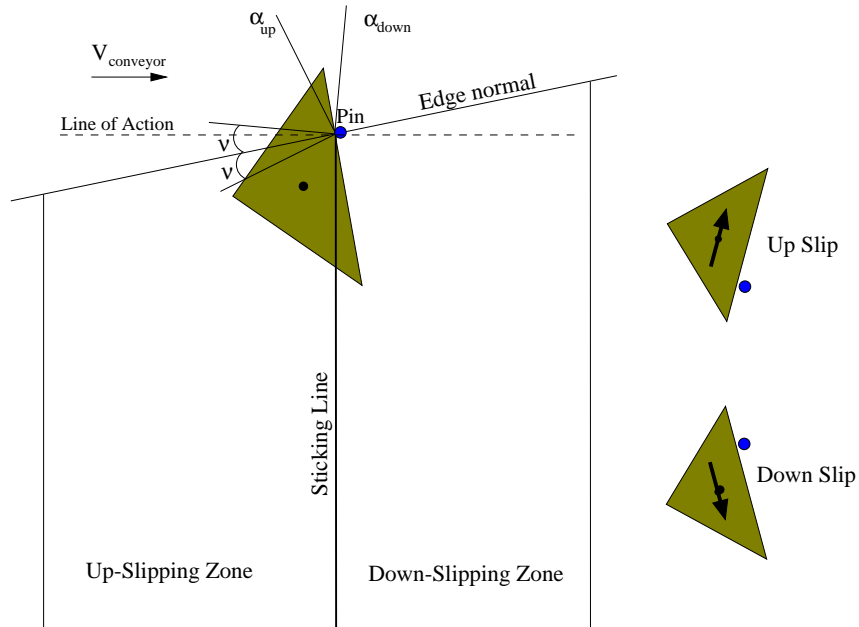


Figure 2-6 Construction of Slipping Zones and relative directions of slip.

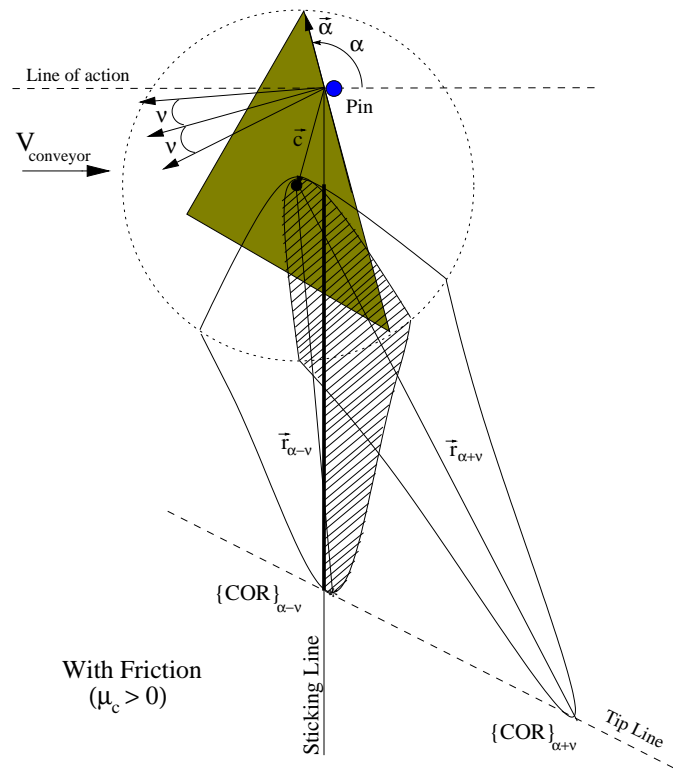


Figure 2-7 Slipping and sticking locus.



## 2.11– Normal Pressure Distribution Assumption

In this study, for the purpose of exploring the behaviour of planar parts with constant thickness and presumably smooth surfaces for part orienting, the instantaneous CORs for a given part geometry are determined by making use of the following assumption: *the planar polygons in this study have a constant and uniform pressure distribution over their entire area and it is assumed to be known.* This concept of normal pressure distribution was illustrated in Figure 2-1(c).

## 2.12– Minimum Power Mechanics

The minimum power principle presents the appealing idea that the motion of the part, that is, the motion that the part “chooses” to undergo given a single pressure distribution, corresponds to that for which the energy dissipated due to sliding friction ( $\mu_s$ ), as per the Coulomb friction model, is minimized [17]. This principle holds true only for the quasi-static approximation along with the simplest model of friction: Coulomb friction [19].

Thus, the amount of energy that will be dissipated as a result of the rotation  $\delta\theta$  about the COR  $\vec{r}$  is described as follows:

$$dE_r = \mu_s P(\vec{w}) d\vec{w} \delta\theta |\vec{w} - \vec{r}| \quad (2-5)$$

Where,  $\delta\theta |\vec{w} - \vec{r}|$  is the distance that an area element at  $\vec{w}$  supporting a force  $P(\vec{w}) d\vec{w}$  normal to the work surface will slide due to the rotation  $\delta\theta$ . Subsequently, the total energy dissipated by the polygonal part is obtained by integrating over its area  $A$ .

$$E_r = \mu_s \delta\theta \int_A P(\vec{w}) |\vec{w} - \vec{r}| d\vec{w} \quad (2-6)$$

Equation (2-6) is rewritten to emphasize that  $E_r$  is a function of the location of the COR  $\vec{r}$ . Thus substituting for  $\delta\theta$ ,

$$E_r = \frac{\delta x \mu_s \sin \alpha}{\vec{\alpha} \cdot (\vec{c} - \vec{r})} \int_A P(\vec{w}) |\vec{w} - \vec{r}| d\vec{w} \quad (2-7)$$

This energy equation needs then to be minimized with respect to  $\vec{r}$  in order to find the COR representing the point about which the part “chooses” to rotate for a given contact configuration. In the proposed modeling approach later outlined, the contact configuration is known, and since the behaviour of the part depends on this known contact configuration then local minimum points are obtained.

### 2.13– Contact Parameter

In this thesis, orienting with pins requires that the position of the polygon’s COM and its perpendicular distance from the pin be known prior to contact. This perpendicular y-distance (Figure 2-8(a)) from the COM to the pin is represented by the contact parameter ( $d$ ). The contact parameter along with the part’s initial orientation  $\theta_i$ ,  $\mu_c$  and  $P_w$  determines the part’s motion when contacting an overhead pin as in expression (2-14).

In the following chapters, selected values of  $d$  are used in the construction of configuration maps to be used in the planning process. For simplicity, the contact parameter  $d$  is labeled as decimal fractions varying within  $[0.1, 0.9]$  and  $[-0.1, -0.9]$  of the geometric parameter  $a$ , where  $a = \max(r_v)$ , and  $r_v$  represents the part’s radii measured from the part’s COM to the part’s vertices as shown in Figure 2-8(a). Parameter  $a$  is used as the geometric reference parameter because it represents the distance between the COM and the farthest point on the part.

Positive values of  $d$  correspond to pins located “above” the COM and negative values correspond to pins “below” as in Figure 2-8(b). The true perpendicular distance between the COM and the pin is the product  $da$  and it is geometry dependent.

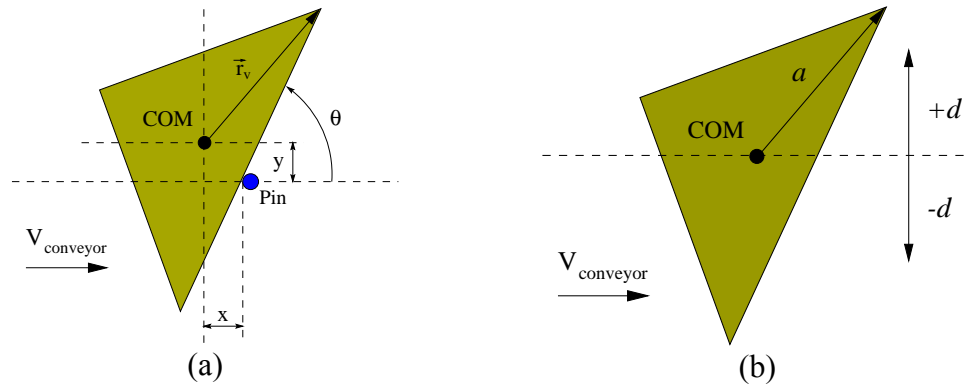


Figure 2-8 (a) Pin and COM distance. (b) Positive and negative  $d$ .

## B. Quasi-Static Motion Modeling

As previously stated, orienting with overhead pins requires an approximation of the motion of the part as it comes into contact with the pin based on the determination of CORs other than the tip of the COR locus. Assuming that a single constant and uniform pressure distribution is present and that  $\mu_c$  is known and constant, the notion of minimum power mechanics is utilized to approximate the instantaneous CORs that dictate the part's motion with friction at the point of contact.

The objective of this section is to present the approach taken to model the motion of a polygonal planar part traveling on a slow moving conveyor belt as it comes into contact with a stationary overhead pin at an initial orientation  $\theta_i$ , rotates and translates against the pin until losing contact and “exits” the pin at a distinct final orientation  $\theta_f$ .

### 2.14 – Finding the Point of Contact

The point on the part that contacts the pin is determined via a simple geometrical approach by using parametric equations for the lines parallel to the edges of the polygon and for the line parallel to the line of action going through the pin. These lines are equated as follows and are illustrated in Figure 2-9:

$$\begin{aligned}\vec{l}_{edge\_i} &= \vec{V}_i + t(\vec{V}_{i+1} - \vec{V}_i) \text{ where } (i = 1,2,3) \\ \vec{l}_{motion} &= \vec{P} - sV_{conveyor}\end{aligned}\tag{2-8}$$

Where  $\vec{V}_i$  ( $i = 1,2,3$ ) indicate the polygon vertices,  $\vec{P}$  is the overhead pin,  $V_{conveyor}$  is the conveyor belt direction unit vector, and  $t$  and  $s$  are referred to as the contact intersection parameters.

For contact to occur, equate  $\vec{l}_{edge\_i}$  and  $\vec{l}_{motion}$ , representing the intersection of these lines, and solve for  $t$  and  $s$  to obtain the following equations for each  $i = 1,2,3$ :

$$\begin{aligned}t &= \frac{\|(\vec{V}_i - \vec{P}) \times V_{conveyor}\|}{\|V_{conveyor} \times (\vec{V}_{i+1} - \vec{V}_i)\|} \\ s &= \frac{\|(\vec{V}_i - \vec{P}) \times (\vec{V}_{i+1} - \vec{V}_i)\|}{\|V_{conveyor} \times (\vec{V}_{i+1} - \vec{V}_i)\|}\end{aligned}\tag{2-9}$$

The contact point therefore is determined in the following sequence, 1) solve for all intersection points, 2) select the edges intersecting the line of action while discarding the others, and 3) select the intersection point closest to the pin. In short, to determine the contact point, select  $s$  as follows:  $\min(s) \exists s \in \{s > 0\}$  for which  $t \in [0,1]$  indicating that the selected point lies within the edge and not “outside” the edge. Figure 2-9 illustrates an example of the selected point of contact for a given configuration. Once the point of contact has been determined and the part makes contact with the pin, the corresponding COR must be resolved and the relative motion of the part against the pin explored.

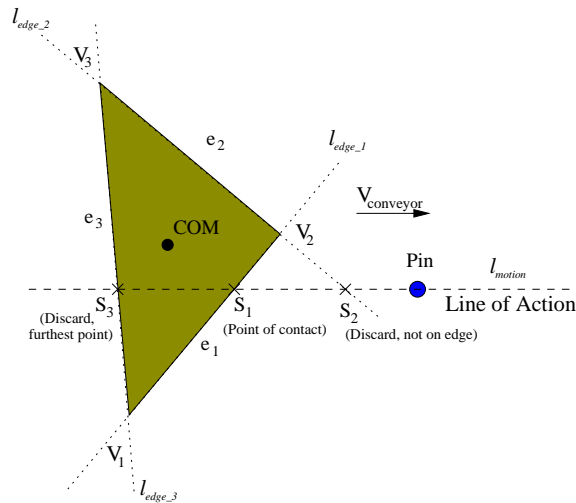


**Figure 2-9 Determining point of contact geometrically.**

## 2.15– Relative Motion of the Part Against the Pin

When the polygonal part makes contact with the pin, in order to accommodate for the infinitesimal advance of the moving conveyor belt  $\delta X$  forcing the part against the pin, the part will rotate an amount  $\delta\theta$  about the COR. This motion is equivalent to the case where the part initially at rest is continuously pushed by a point pusher such as a moving pin.

As described in [17], a rotation of  $\delta\theta$  allows for an advance of the pusher  $\delta X$  consisting of two parts,  $\delta X_1$  and  $\delta X_2$  as illustrated in Figure 2-10. In the case of a stationary pin and a moving part, the same motion equations, (2-10) through (2-12), apply for infinitesimal amounts of rotation  $\delta\theta$  resulting from the continuous motion of the conveyor belt carrying the part over infinitesimal amounts of distance  $\delta X$ .

As the part translates due to the motion of the conveyor belt, the edge in contact with the pin must remain in contact with the pin while accommodating for the advance of the part. That is, from the opposite perspective, the edge being “pushed” by the pin must move out of the way of the pin (i.e. rotate and translate) but stay in contact. The overall motion of the part for an infinitesimal amount of rotation  $\delta\theta$  is determined by the equations that follow.

Due to rotation:

$$\delta X_1 = \delta\theta |\vec{c} - \vec{r}| \cos \theta = \delta\theta (c_y - r_y) \quad (2-10)$$

Due to translation of the contact point along the edge:

$$\delta X_2 = \delta X_1 \frac{\tan \theta}{\tan \alpha} = \frac{\delta\theta}{\sin \alpha} \vec{\alpha} \cdot (\vec{c} - \vec{r}) \quad (2-11)$$

$$\text{where } \vec{\alpha} = (\cos \alpha \quad \sin \alpha)$$

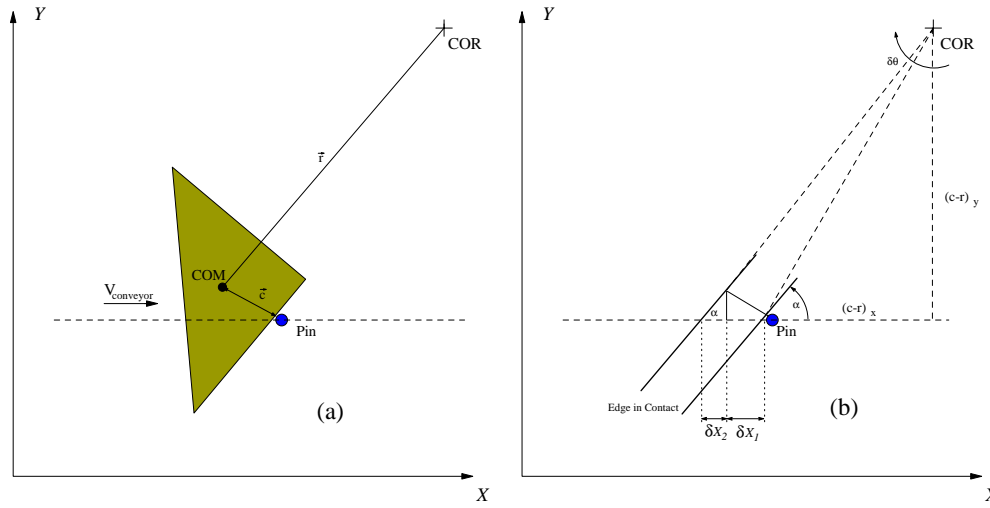


**Figure 2-10 Relative motion of polygonal part against stationary point obstacle, where (a) shows the instantaneous COR for the given contact configuration, and (b) shows the resulting  $\delta\theta$  about the COR due to the advancement  $\delta X$  of the conveyor belt, where  $\delta X = \delta X_1 + \delta X_2$ .**

The total displacement is:

$$\delta X = \delta X_1 + \delta X_2 \quad (2-12)$$

For the modeling of the case of a stationary pin and a moving object, throughout each iteration in the simulation, the displacement resulting from the infinitesimal  $\delta\theta$  about the appropriate instantaneous COR is determined and the polygon is rotated. Since

the part must remain in contact with the pin throughout the entire period of motion and interaction, to complete the iteration the part is then translated a distance  $\delta X$  so that the part is again in contact with the pin at its new contact point. Figure 2-11(a) shows the edge that contacts the pin before and after the rotation of  $\delta\theta$  and it shows the original contact point labeled “Reference Point”. Depending on whether the part slips or sticks, the point of contact will change or remain the same. In Figure 2-11(b), the mode of behaviour was *slipping* and therefore the new contact point is not different from the reference point. But, in Figure 2-11(c), the mode of behaviour was *slipping* and the point of contact does change.

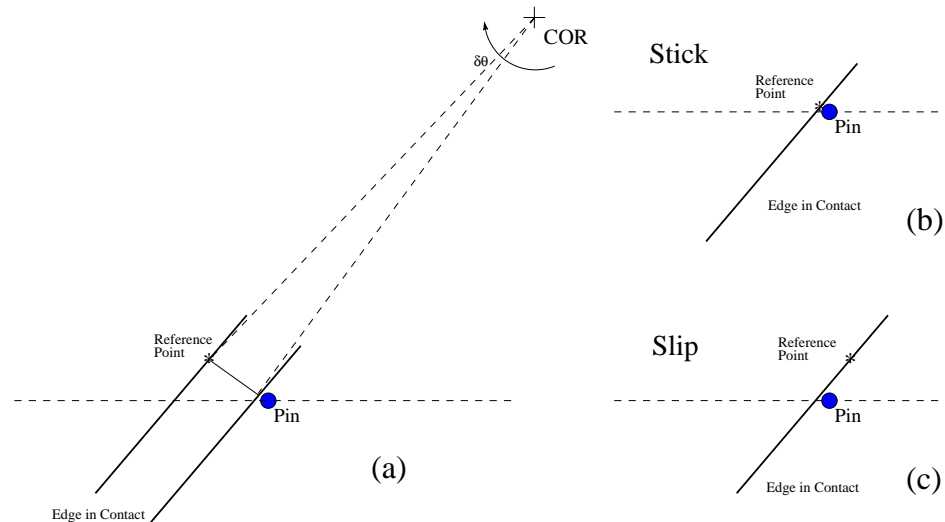


**Figure 2-11 (a) Maintaining contact between part and pin after rotating polygon by  $\delta\theta$ . In (b) the figure corresponds to *sticking* while in (c) it corresponds to *slipping* motion.**

## 2.16 – Estimating the COR Using Minimum Power Mechanics

This section outlines the methodology used for approximating the instantaneous CORs that underline the motion of a given part against an overhead stationary pin.

As previously stated, the minimum power principle presents the appealing idea that the motion of the part corresponds to that for which the energy dissipated due to

sliding friction is minimized. Subsequently, the equation representing the total energy  $E_r$  lost to friction with the surface due to the rotation  $\delta\theta$  as previously visited in equation (2-7) is modified as follows:

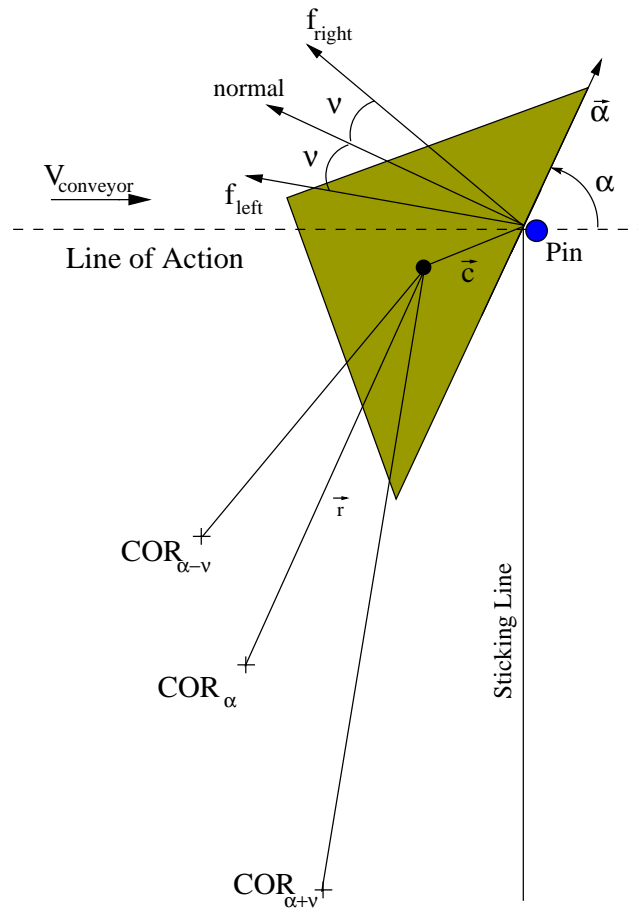
$$E_r = \frac{\delta x \mu_s \sin \alpha}{\vec{\alpha} \cdot (\vec{c} - \vec{r})} P_w \iint_A \sqrt{(w_x - r_x)^2 + (w_y - r_y)^2} dw_y dw_x \quad (2-13)$$

Of interest is the position of the vector  $\vec{r}$  that minimizes equation (2-13), where  $w_x$  and  $w_y$  are the coordinates of a point  $\vec{w}$  in the area of a given polygon as illustrated in Figure 2-3, and  $P_w$  is the term representing the constant uniform pressure distribution as per the stated assumption. Note that even if the pressure distribution is not a normal distribution but it is known as a function  $P(\vec{w})$  then the modeling approach proposed here still holds. For the minimization of  $E_r$  the **Matlab** function **fminsearch** is utilized. This function bases its solution on a Nelder-Mead type simplex method (see Appendix A) when searching for the minimum value of a given equation such as (2-13). Given an initial guess, the function returns a vector  $\vec{r}$  which is a local minimizer of  $E_r$  near the given starting vector. In the proposed approach, this initial guess is the tip of the COR locus. Using the tip of the locus as the initial vector for the minimizing function is considered an educated first guess because the locus tip is the furthest point within the COR locus where the actual COR is expected to be. Hence, appropriately selecting the area where the local minimum is expected to be found by the function **fminsearch**. To obtain the COR locus tip vector for a given contact configuration, first, the rotation sense is determined using Mason's Voting Theorem, and then by checking whether the line of action is contained within the friction cone bounds or not and referring to Section 2.10 for the conditions of slip and stick the appropriate COR locus tip is determined. Figure 2-12 illustrates the resulting COR locus tip positions that can be used as initial guesses



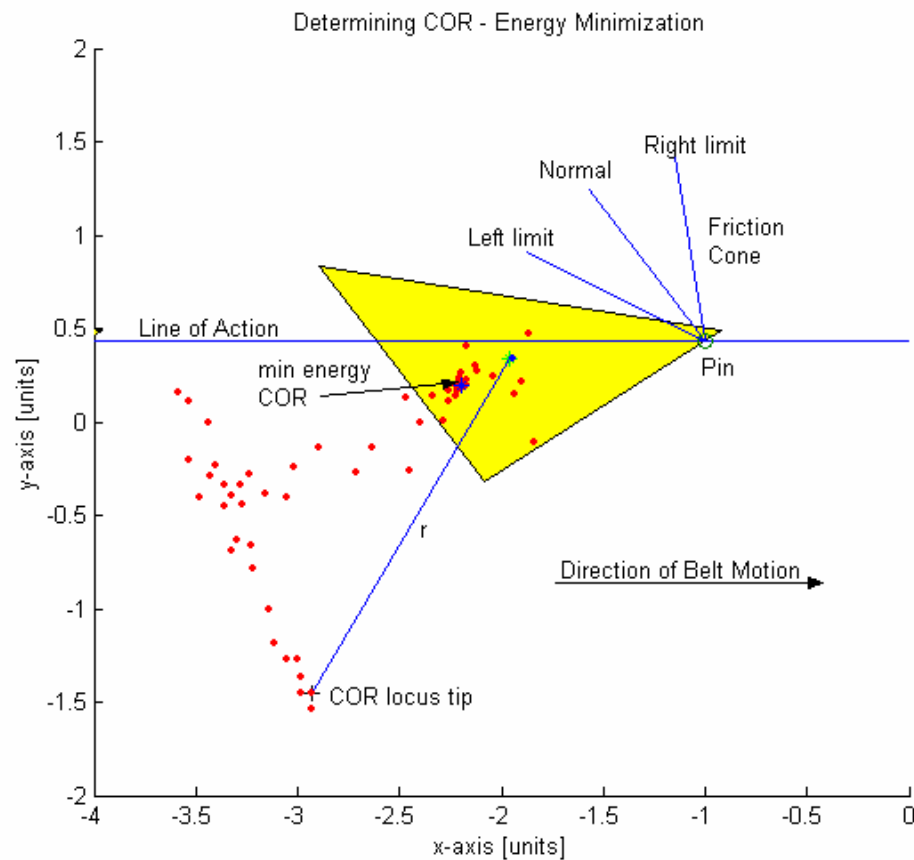
for the minimization of  $E_r$  depending on the conditions of motion (i.e. stick, up-slip, and down-slip).

Figure 2-13 illustrates the minimization process of  $E_r$  and the resulting instantaneous COR. The initial guess is the COR locus tip shown in the figure, and the scattered dots in Figure 2-13 are the function's iterations' results towards finding the point of minimum energy  $E_r$  representing the instantaneous COR. Note the difference in position of the resultant minimal energy COR, labeled as “min energy COR” in the figure, from the initial guess, the COR locus tip. The final position of the COR being closer to the part’s COM implies more rotation and less translation of the part about this new COR point as indicated in Section 2.8.



**Figure 2-12 COR locus tip locations during slipping and sticking.**

In [17] the integration in equation (2-13) is carried over the entire area of the predefined disc of radius  $a$  enclosing the polygon shown in Figure 2-4, while in this study it is carried over the actual cross-sectional area  $A$  of the polygon. Thus, attempting to find a more representative instantaneous COR for the given polygon's geometry under the stated assumptions. Moreover, due to the complexity of this integration, Finite Element methods (see Appendix B) are used to transform a general triangular polygon into a standardized rectangle; thus, simplifying the calculations.



**Figure 2-13** Determining the instantaneous COR using minimum power mechanics: starting with the point “COR locus tip” as the initial guess, the minimization function finds a new instantaneous COR, the result is the point labeled “min energy COR”.

## C. Part Orienting Background

### 2.17 – Configuration Maps

Configuration maps were introduced in [18]. They encapsulate the physics of an operation such as a part contacting an overhead pin. Figure 2-14 illustrates a typical configuration map. The horizontal axis gives the initial orientation  $\theta_i$  of the part prior to contact with the pin, while the vertical axis gives the final orientation  $\theta_f$  after contacting the pin, rotating and sliding about it until losing contact.

The resulting map is composed of rectangular bands, where the sets  $B_j$  ( $j=1,2,3$ ) represent the intervals of the sets of final orientations and the sets  $K_j$  bound the ranges of initial orientations that result in the corresponding final orientation sets  $B_j$ . The bands in this map indicate the uncertain variation in rotation of a part due to the unknown pressure distributions.

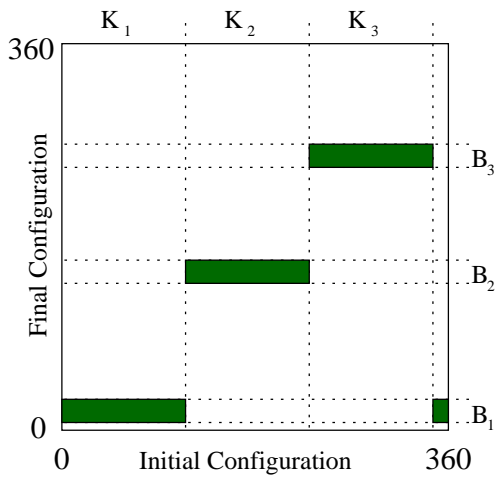


**Figure 2-14 Typical configuration map.**

In this study, the final orientations of a given polygon after contacting a stationary overhead pin, result from the relation:

$$\theta_f = f(\theta_i, d, \mu_c, P_w) \quad (2-14)$$

Where  $\mu_c$  and  $P_w$  are assumed to be known constants and  $d$  is the contact parameter discussed in the next section. This relation implies a 1:1 mapping from initial to final orientation. But, it is of interest to form bands similar to those seen in the typical configuration map in Figure 2-14. For this purpose, for the listed values of  $\theta_i$   $[0^\circ, 360^\circ)$ , their corresponding values of  $\theta_f$  are examined and compared against their adjacent  $\theta_f$  values. The common  $\theta_f$  values whose difference is less than a set threshold value  $T$  as in the expression that follows are grouped together. Thus, the condition for  $\theta_f$  grouping is as follows:

$$|\theta_{f_{j+1}} - \theta_{f_j}| \leq T \quad (2-15)$$

These groups are then bounded by their maximum and minimum values and the result are intervals  $B_j$  along the  $\theta_f$  axis such as band  $B_2$  in the typical configuration map shown in Figure 2-14. For each group, the band interval is defined as the bounded set of all  $\theta_f$  belonging to that group as follows:

$$B_j = [\min, \max) \{ \theta_f \in group \} \quad (2-16)$$

And the corresponding initial orientation interval  $K_j$  is defined as the bounded set of all  $\theta_i$  for which  $\theta_i$  yields a final orientation included in the corresponding band  $B_j$  as follows:

$$K_j = [\min, \max) \{ \theta_i \mid \alpha = f(\theta_i, d, \mu_c, P_w) \forall \alpha \in B_j \} \quad (2-17)$$

Of importance are also the center of mass (COM) intervals that result due to the variation in final orientations  $\theta_f$  in the corresponding  $B_j$ . These intervals  $COM_j$  are defined as the bounded sets of the possible COMs resulting from the final orientations  $\theta_f$  contained within the corresponding band  $B_j$  as follows:

$$COM_j = [\min, \max) \{COM \mid \theta_f \Rightarrow COM \forall \theta_f \in B_j\} \quad (2-18)$$

These intervals are then used in the planning process.

## 2.18 – Stable Equilibrium States

The determination of a part's stable equilibrium states stems from the radius function first applied by Goldberg for the purpose of orienting a polygon through a series of parallel jaw grasps [10]. The radius function of a polygon is, as defined by Goldberg, a mapping from the orientation  $\phi$  of a support line or base line of the polygon to the perpendicular distance  $r$  from a reference point in the polygon, such as the COM of the polygon, to the support line. Where, the local minima of the radius function indicate the stable equilibrium orientations of the polygon. Figure 2-15(a,b) shows two triangular polygons used in this study, each shown at their  $\phi=0^\circ$  initial orientation, and their corresponding radius function plots are illustrated in Figure 2-15(c,d) respectively. The local minima in each plot clearly show that each triangular polygon has three stable equilibrium states.

These two polygons are used throughout the remainder of this thesis document for discussion purposes. The first one (Figure 2-15(a)) is a triangle polygon with symmetric properties and will be referred to as TriPoly1, while the second one (Figure 2-15(b)) is an asymmetric triangular polygon that will be referred to as TriPoly2.

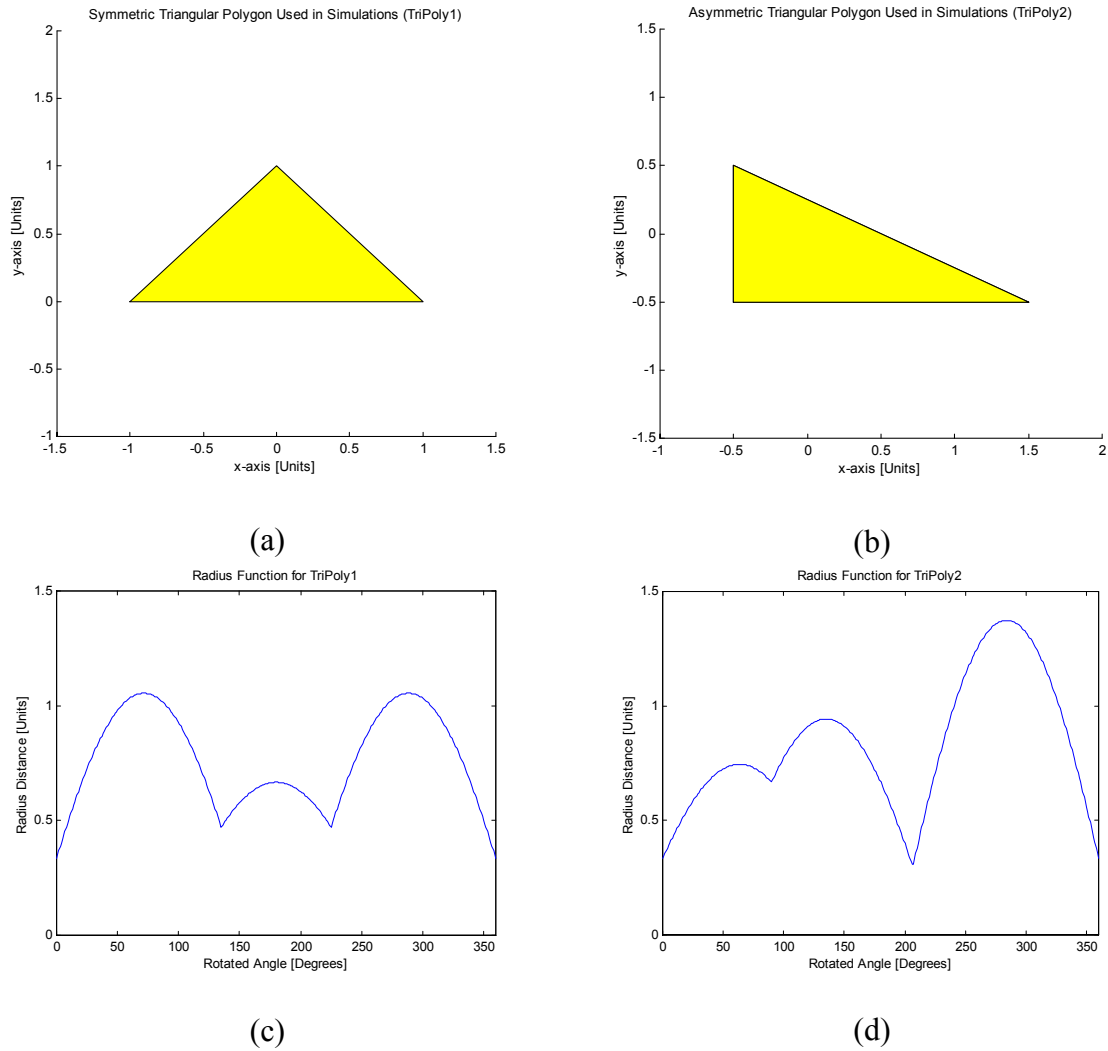


**Figure 2-15** Triangular polygons: (a) TriPoly1 and (b) TriPoly2, with their respective radius function plots in (c) and (d) respectively.

## Chapter 3

# Configuration Maps Using Overhead Pins

In this chapter the behaviour of triangular polygonal parts is investigated as per the modeling approach outlined in Chapter 2, and verified by a series of experimental trials. First, using the proposed model, the motion of polygonal parts against static passive overhead pins is studied, and the results are presented in the form of *configuration maps* (Section 2.17). Then, results from experimental trials using a simple setup of Mylar film and an overhead static pin without sensing are obtained and compared against the simulation results. Lastly, based on this comparison, an empirical method of adjusting the width of the bands  $B_j$  (defined in Section 2.17) in the configuration maps is devised with the goal of reducing uncertainty due to the assumptions made in the modeling method. The results obtained in this chapter are then used in the development of the planning strategy presented in the following chapter, Chapter 4.

### 3.1 – Static Passive Simulation Results

In order to develop a planning strategy for part orientation, the behaviour of the part being investigated must be understood. This section presents the results obtained for the motion of a triangular polygon against an overhead pin in accordance to the modeling approach described in the previous chapter. First, individual initial orientations are explored, and then configuration maps are constructed. Throughout this chapter, the two triangular polygons referenced are TriPoly1 and TriPoly2 as illustrated in Figure 2-15(a) and (b) respectively in Section 2.18.

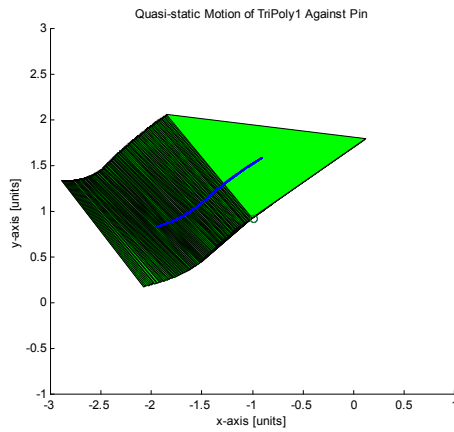
### 3.1.1 – Motion of Polygonal Part

First, results were obtained for simulations of individual random initial orientations using the tip of the COR locus ( $r_{tip}$ ) as the instantaneous center of rotation (COR) for each contact configuration resulting from infinitesimal amounts of rotation  $\delta\theta$ . The purpose of simulating the motion of the polygonal part against an overhead stationary pin using the  $r_{tip}$  point is for comparing them against the approximated CORs calculated via minimum power mechanics as explained in Section 2.12.

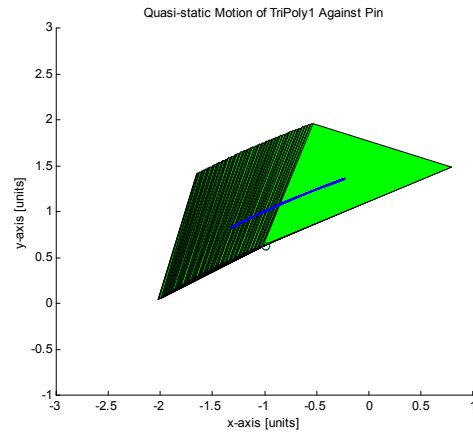
Figure 3-1 depicts the motion of the symmetrical triangular polygon, TriPoly1, against a point obstacle representing the overhead pin as per the modeling approach using a constant coefficient of friction for  $\mu_c$  equal to 0.5. Figure 3-1(a-b) correspond to two scenarios where the  $r_{tip}$  is used as the instantaneous COR in each iteration of the overall motion plotted; whereas, Figure 3-1(c-d) pertain to the equivalent two scenarios where the COR points in each iteration were calculated by the minimization of the energy equation (2-13). As described in Section 2.8, parts that rotate about any point other than the  $r_{tip}$  within the locus will rotate more and translate less, where those closer to the part's COM exhibit larger amounts of rotation. Here, plots (a-b) exhibit less rotation than plots (c-d) due to the position of the CORs within the described COR locus area. Note the resulting angles between the corresponding contact edges and the  $x$ -axis at the end of contact, where the angles for plots (a-b) are larger than those in (c-d). The more acute angles in (c-d) indicate that the polygon does indeed rotate more against the pin in these cases than in their equivalent counterparts (a-b). For further comparison and validation of the polygon's observed motion against a stationary overhead pin, a sample of an experimental trial at  $d = -0.2$  and  $\theta_i = 30.00^\circ$  is depicted in Figure 3-2. The resulting final orientation for this trial is  $\theta_f = 11^\circ$ , which is only  $1^\circ$  apart from the proposed model response, while the resulting motion about the COR locus tip is  $14^\circ$  apart. This experimental trial then supports the proposed modeling approach presented in Chapter 2.



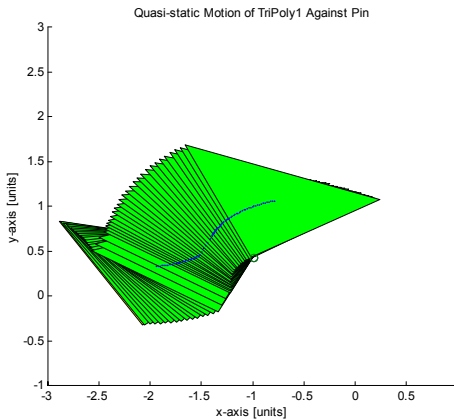
This comparison of the part's motion resulting from using the COR locus tip vs. using the minimum energy COR points, against the equivalent experimental trials illustrates the reason why using the locus tip points as CORs is deemed not sufficient to model and understand the behaviour of the part for the purpose of part orienting with overhead pins. Thus, it is imperative that an appropriate motion model like the one presented in Chapter 2 is implemented for the understanding and representation of the part's behaviour.



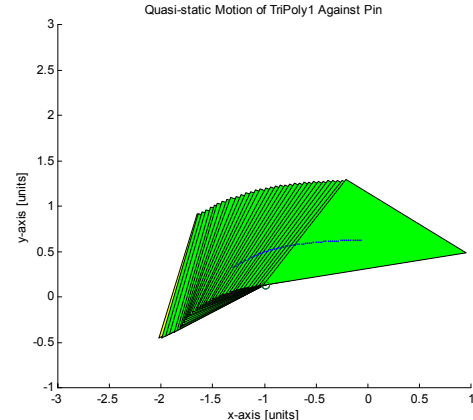
(a)  $d = 0.1$ ,  $\theta_i = 170.00^\circ$   $\theta_f = 172.35^\circ$



(b)  $d = -0.2$ ,  $\theta_i = 30.00^\circ$   $\theta_f = 25.41^\circ$

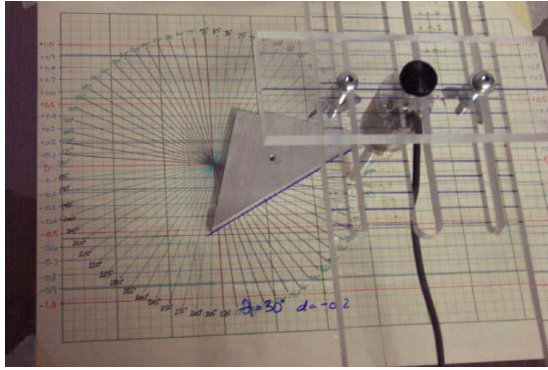
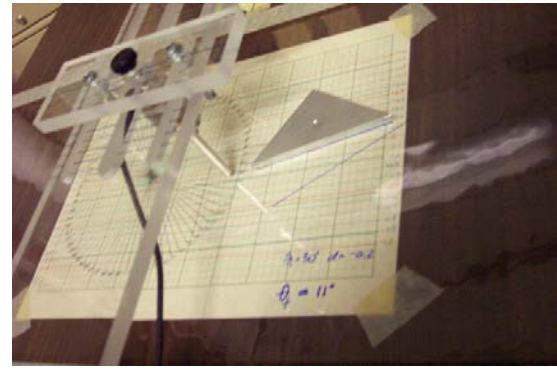


(c)  $d = 0.1$ ,  $\theta_i = 170.00^\circ$   $\theta_f = 161.72^\circ$



(d)  $d = -0.2$ ,  $\theta_i = 30.00^\circ$   $\theta_f = 9.99^\circ$

**Figure 3-1 Comparison of TriPoly1 motion against point obstacle (i.e. overhead pin) between COR locus tip point (a-b) and minimum energy COR (c-d) for two different contact configurations.**

(a)  $d = -0.2$ ,  $\theta_i = 30.00^\circ$ (b)  $d = -0.2$ ,  $\theta_f = 11^\circ$ 

**Figure 3-2** Experimental trial for triangular polygon (TriPoly1) starting at  $\theta_i = 30.00^\circ$  in (a) and ending at  $\theta_f = 11^\circ$  in (b) for a contact parameter value of  $d = -0.2$ .

### 3.1.2– Configuration Maps

Configuration maps were constructed, as per equations (2-14) thru (2-17), using the compiled data pertaining to the motion of each given triangular polygonal part against a stationary point obstacle for all the contact configurations dependent on selected values of initial orientation  $\theta_i$  and contact parameter  $d$ . Overall, 18 configuration maps for each triangular polygon investigated were generated. Each map corresponds to a distinct value of the contact parameter  $d$  varying within  $[0.1, 0.9]$  and  $[-0.1, -0.9]$ .

Figure 3-3 illustrates and compares samples of configuration maps corresponding to TriPoly1. Figure 3-3(a-c) show maps generated using the tip of the COR locus ( $r_{tip}$ ), maps in (d-f) using the minimum energy CORs and lastly, the equivalent experimental results in (g-i). The experimental setup and trials are discussed in Section 3.2 to follow.

In general, within each map three clear bands were observed. This indicates that for any initial orientation  $\theta_i$  and a given  $d$ , the final orientation will exist within these three final orientations *bands*,  $B_j$ . However, within all cases studied, the width of the bands  $B_j$  varies. All plots on the 1<sup>st</sup> row (a-c) clearly show wider bands than those on the remaining two rows (d-f) and (g-i). This difference in band width is due to the increased amount of sliding and reduced rotation attributed to motion about the COR locus tip. Furthermore, physically, the motion of the part against a pin cannot be constrained to

behave as if the part rotated about the  $r_{tip}$ . Thus, it must be emphasized that the  $r_{tip}$  can't be used when modeling the part's motion. Finally, for planning purposes, narrower bands are desired, as they increase the likelihood that a solution will be found in the planning strategy. Hence, the instantaneous CORs that dictate the motion of the part resulting in behaviour similar to that of Figure 3-3(g-i) are found and the behaviour mapped in (d-f).

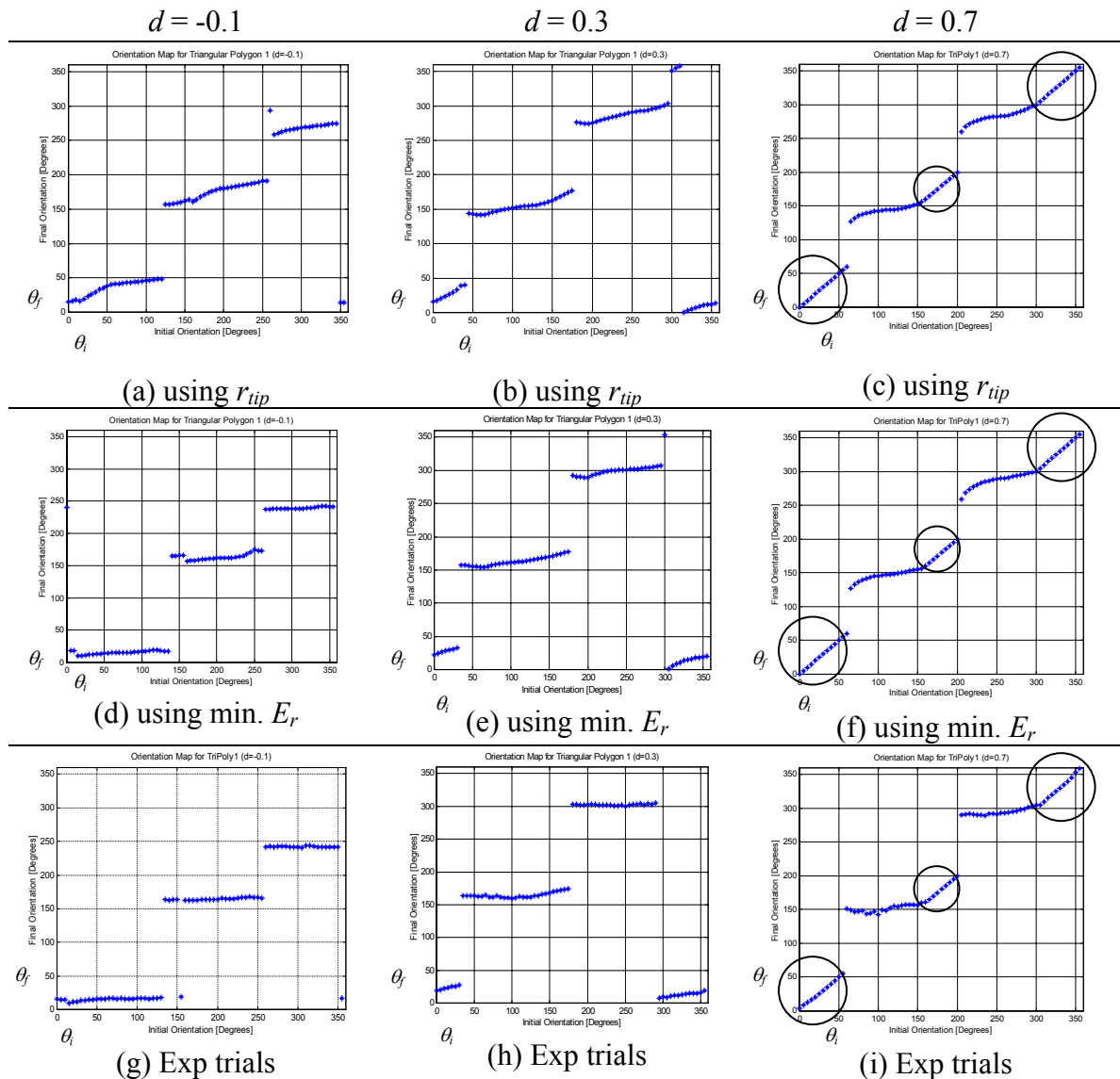


**Figure 3-3** Configuration maps for given  $d$  values, using the  $r_{tip}$  as COR in (a-c), minimized  $E_r$  in (d-f) and equivalent experimental trials in (g-i).

### 3.1.2.1 – Instances of No-Contact (NC) with Pin

Brief regions within the configuration maps for  $d = 0.7$  (circled regions in Figure 3-3(c,f,i)) in which the plots are linear, that is,  $\theta_i = \theta_f$ , are noted. This linearity corresponds to instances in which the part does not make contact with the pin for the specified  $\theta_i$  orientation and contact parameter  $d$ , but instead the part continues to travel along the direction of belt motion without change in orientation. These instances are important because unlike orienting with fences where all parts will make contact with the fences as they move down the conveyor belt, orienting with pins requires that intervals of “no-contact” are created in a similar fashion to the *bands*  $B_j$ , and be incorporated in the planning strategy.

Thus, for the cases of “no-contact” the adjacent values of  $\theta_f$  are grouped according to expression (2-15) and the intervals  $NC_j$  ( $j=1,2,3$ ) are defined as bounded sets where for all initial orientations equal to their respective final orientations belong to a selected *group*. This definition is written as follows:

$$NC_j = [\min, \max) \{ \theta_i \mid \theta_i = \theta_f \forall \theta_f \in group \} \quad (3-1)$$

## 3.2– Static Passive Experimental Results

Having created configuration maps via simulations, the motion results must be compared against experimental outcomes for validation. For this purpose, a simple setup consisting of a roll of Mylar film acting as a conveyor belt and a static passive pin mounted overhead was used. Figure 3-4 shows a picture of this setup.

Note that the materials selected and used in this experimental setup will affect the coefficient of contact friction,  $\mu_c$ . Here, the pin is made of steel while the polygon is made of aluminum, and the static coefficient of friction is given as 0.61 while the kinetic coefficient of friction is given as 0.47 in [32]. Given that in quasi-static motion no

distinction is made between static and kinetic friction, and that any kinetic energy resulting from the part's motion (i.e. sliding against the pin) is quickly dissipated by the frictional forces, then it is assumed that static friction prevails. But as an “ad hoc” method the value assumed for  $\mu_c$  is an average of the two aforementioned values; thus, the coefficient of friction is estimated to be approximately 0.54. Furthermore, in order to remove any irregularities on the edges of the polygon, the edges were polished, thus creating smooth surfaces, which in turn reduced the amount of friction by a slight but unknown amount. Consequently, an approximate constant value of  $\mu_c = 0.5$  for the coefficient of friction at the polygon-pin interface is assumed. This value of contact friction matches the value used in the modeling simulations, and is therefore justified for comparison purposes of the quasi-static motion results between modeling and experimental results.

Lastly, it must be noted that in the simulations the overhead pin is modeled as a point obstacle, while the steel pin used in the experimental setup has an actual diameter of  $\frac{1}{4}$  inch. Discrepancies in the resulting initial orientation intervals  $K_j$  and final orientation bands  $B_j$  between the simulation and experimental configuration maps in Figure 3-3 can be attributed to the pin diameter.

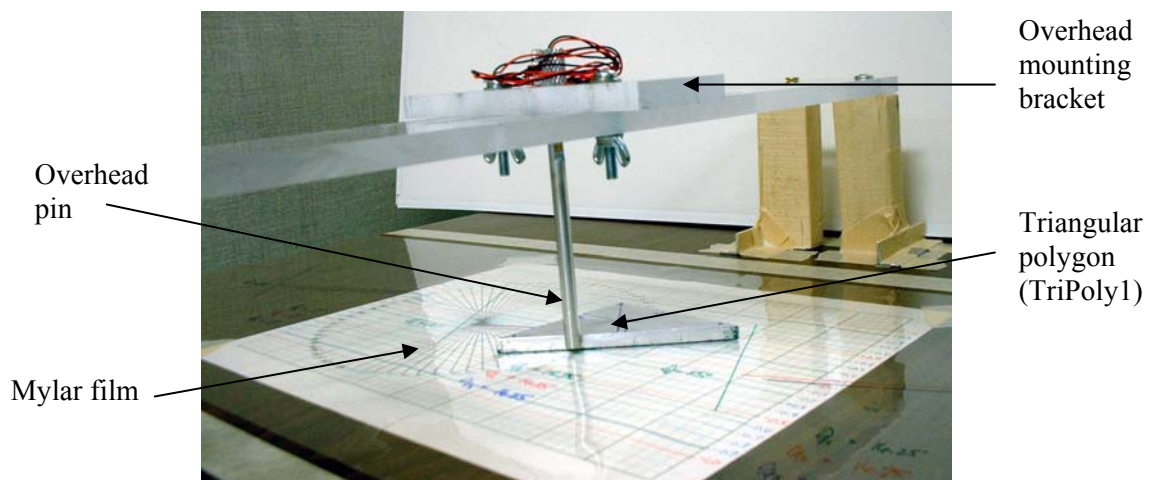


**Figure 3-4** Passive pin experimental setup.

The experimental configuration maps were created by conducting three trials for each  $\theta_i$  and averaging the resulting  $\theta_f$  to be plotted. Row 3, (g-i) of Figure 3-3 shows the experimental maps for the equivalent values of  $d = -0.1, 0.3$  and  $0.7$  respectively. The bands in these experimental maps are clearly narrower than in any of the simulation maps shown. But, comparing (d-f) and (g-i) shows that the maps created using the calculated CORs provide a good approximation of the part's actual motion; thus, supporting the modeling approach presented in this thesis.

Nonetheless, attention must be paid to the single outlier point in (g) at  $\theta_i = 155^\circ$ . Here, the part contacted the pin not on an edge but on a vertex. Consequently, the part rotated unpredictably in the opposite direction than expected. This phenomenon, capable of leading to failure in the orienting process is later explored and discussed empirically in Chapter 5 using a force/torque sensor.

### 3.3– Bands' Interval Widths

The large intervals of final angles  $\theta_f$  in the experimental configuration maps (Figure 3-3(g-i)) occur due to uncertainties from the part's unknown pressure distribution as well as any slight irregularities at the contact interface affecting the final amount of slip and slide of the part against the pin. On the other hand, the simulation configuration maps (Figure 3-3(d-f)) were constructed by assuming a *constant and uniform pressure distribution* and *constant contact friction*, and they show even larger  $B_j$  interval widths. These larger band widths further occur due to the idealistic assumptions and criteria used in the proposed model to determine whether a part sticks or slips against the pin even when it is difficult to predict the behaviour modes.

Figure 3-5 shows TriPoly1 in two orientations representing the upper and lower limits of an orientation band  $B_j$  after contacting a pin. This figure depicts how, for the same contact parameter  $d$ , a part can rotate to various  $\theta_f$  angles that belong to the same set of final orientations dependent on the initial orientation  $\theta_i$ . Any other  $\theta_f$  orientations

resulting within these illustrated upper and lower limits belong to the same final orientation band  $B_j$  as defined in expression (2-16). The problem that arises with large  $\theta_f$  intervals  $B_j$  is the consequent upper and lower limits of COM location also illustrated in Figure 3-5 resulting in large COM intervals  $COM_j$  as defined in expression (2-18). For planning purposes, the variation in the position of the COM introduces an uncertainty that affects the decision of locating pins to find a sequence to orient the part to a final single orientation set.

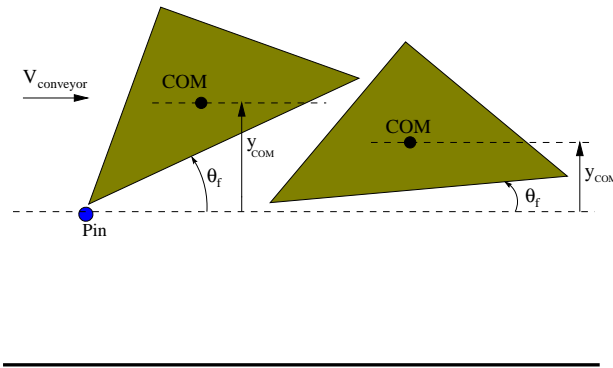


**Figure 3-5 Variation in final angles  $\theta_f$  resulting in band intervals for TriPoly1.**

Moreover, the width difference of the band intervals is also dependent on the location of the point of contact, that is, the value of the contact parameter. For example, comparing the bands in the configuration maps for  $d = 0.3$  in Figure 3-3 against those in the maps for  $d = 0.7$  (ignoring the linear regions), observe the difference. The  $B_j$  intervals for  $d = 0.7$  are wider than those for  $d = 0.3$ . This difference is indicative of the decrease/increase in rotation/translation of the part with relation to  $d$ .

Figure 3-6 summarizes the results of all 18 configuration maps corresponding to TriPoly1 for all initial orientations  $\theta_i \in [0^\circ, 360^\circ)$ , where the figure illustrates the plot of the resulting band intervals  $B_j$  for each contact parameter  $d$  contained within  $[0.1, 0.9]$  and  $[-0.1, -0.9]$  along the horizontal axis and the final angle  $\theta_f$  intervals on the vertical axis.

Here, the band intervals  $B_j$  are represented by short vertical line segments bounded by their minimum and maximum values as defined in expression (2-16) and depicted by a “+”, along with their corresponding calculated mean values, depicted by a “\*”. Referring to Figure 2-8 where the contact parameter was defined, observe in Figure 3-6 that the intervals' widths increase as the value of  $|d|$  increases. So, for low values of  $|d|$ , that is, when the pin is perpendicularly closer to the part's COM, the part rotates more closely to an average value of  $\theta_j$ , hence, creating a smaller band interval. On the other hand, as  $|d|$  increases, that is, when the pin is perpendicularly farther from the part's COM, the band interval increases implying that the part translates more and rotates less, and  $\theta_j$  is more dependent on the initial orientation  $\theta_i$  prior to contacting the pin.

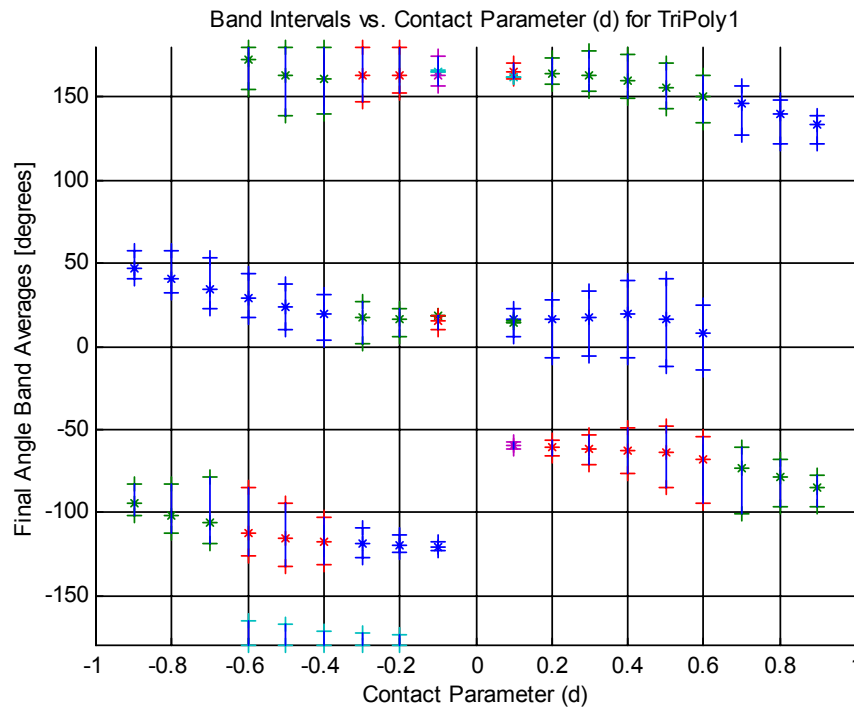


**Figure 3-6 Band intervals vs. contact parameter plot.**

Another important feature of Figure 3-6 is its ability to show that the final orientations for the triangular polygon studied are limited. For each different contact



parameter three band intervals are observable and these are clearly similar to those of other contact parameter values. Two of these final orientation sets can occur given any contact parameter, while there are two other orientation sets from which one occurs only under a positive contact parameter ( $+d$ ) and the other under a negative contact parameter ( $-d$ ). Therefore, it can be deduced that if a single final orientation exists it is most likely to be one of the two common orientation sets occurring for most values of  $d$ .

### 3.3.1– Comparing Simulation Against Experimental Band Intervals

To verify the collection of final orientation simulation bands in Figure 3-6 a comparison with the experimental results was carried out. The experimental band intervals are plotted in Figure 3-7 where although less points are available to compare against, it can be seen that for lower values of  $|d|$  smaller interval widths still do occur and the ranges of the band intervals closely match those in the previous figure. Nonetheless, note that the widths of these intervals are smaller than those seen in Figure 3-6.

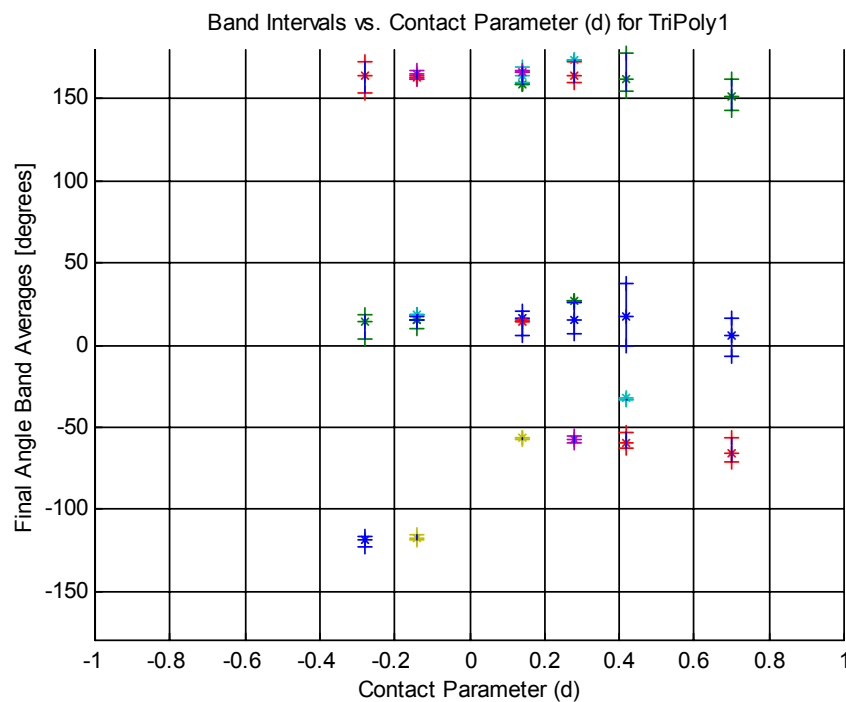


**Figure 3-7** Experimental band interval vs. contact parameter plot.

Table 3-1 tabulates the results of the final orientation intervals' comparison between the simulation and experimental results (Figure 3-6 vs. Figure 3-7). In all the cases outlined, the widths of the simulation intervals are noticeable larger than those of the experimental counterparts; therefore, for this particular comparison the experimental intervals are said to be subsets of their corresponding simulation intervals. The difference in intervals' widths are shown in the last column of Table 3-1.

The large positive differences imply an uncertainty appearing in the simulation results attributable to the pressure distribution and contact friction assumptions in the proposed motion model. And so, given the evident difference in interval widths, it is desired to modify the simulation intervals.

**Table 3-1 Comparison of interval widths, Simulation vs. Experimental.**

Contact Parameter ( $d$ )	Simulation Bands, $\theta_f$	Simulation Bands' Width	Experimental Bands, $\theta_f$	Experimental Bands' Width	Bands' Width Difference
-0.3	(-127° -109°)	18°	(-123° -117°)	6°	12°
	(2° 27°)	25°	(4° 19°)	15°	10°
	(147° -172°)	40°	(154° 173°)	19°	21°
-0.1	(9° 20°)	11°	(10° 18°)	8°	3°
	(157° 175°)	18°	(162° 167°)	5°	13°
	(-123° -117°)	6°	(-119° -116°)	3°	3°
0.1	(5° 23°)	18°	(6° 21°)	15°	3°
	(160° 170°)	10°	(160° 169°)	9°	1°
	(-63° -57°)	6°	(-58° -56°)	2°	4°
0.3	(-6° 33°)	39°	(7° 26°)	19°	20°
	(153° 178°)	25°	(160° 173°)	13°	12°
	(-71° -53°)	18°	(-60° -55°)	5°	13°
0.4	(-8° 40°)	47°	(-1° 37°)	38°	9°
	(148° 176°)	27°	(155° 178°)	23°	4°
	(-77° -49°)	28°	(-63° -53°)	10°	18°
0.7	n/a n/a	n/a	(-7° 16°)	23°	n/a
	(127° 157°)	30°	(143° 162°)	19°	11°
	(-101° -61°)	40°	(-71° -55°)	16°	24°

### 3.4 – Adjusting the Bands' Interval Widths

A comparison between the bands' widths of the simulation and experimental configuration maps, Figure 3-6 and Figure 3-7 respectively and Table 3-1 revealed the simulation bands are wider than its experimental counterparts. Having attributed the differences to the pressure distribution and contact friction assumptions in the simulation, the simulation bands' widths are adjusted via a simple method using the bands' interval mean ( $m$ ) of all the elements in the simulation set  $B_j$  and the corresponding standard deviation ( $\sigma$ ) values of the same set  $B_j$ :

$$B_{j\text{ adjusted}} = m_{B_j} \pm \sigma_{B_j} \quad (3-2)$$

Thereby removing some of the uncertainty found in the bands' widths. This method is motivated by the fact that using the mean and the standard deviation of the set  $B_j$  to construct the adjusted set  $B_{j\text{ adjusted}}$  takes into consideration the weighting of all the elements in the set. Now, since it is desirable that these adjusted intervals are close to the experimental results, the adjusted intervals are then compared against the experimental intervals. The adjusted simulation bands are plotted below in Figure 3-8.

Figure 3-8 shows the smaller adjusted band intervals  $B_{j\text{ adjusted}}$  plotted in a similar fashion to that of Figure 3-6 with all the contact parameters in the horizontal axis and the  $\theta_f$  bands in the vertical axis. The overall width of the bands has been reduced; and the relation between the magnitude of  $d$  and the final orientation bands still hold true, that is, as  $|d|$  increases the width of  $B_{j\text{ adjusted}}$  increases and vice-versa.

Comparison differences between the adjusted intervals and the experimental bands (Figure 3-8 vs. Figure 3-7) are tabulated in Table 3-2 and show that the adjusted interval widths are now closer to the experimental results. Also, the adjusted intervals are still larger than the experimental intervals, thus indicating that the experimental bands in this case are still seen as subsets of the simulation bands. In rare cases we found the

opposite, and therefore, using the adjusted intervals  $B_{j\text{adjusted}}$  to seek for a solution in the planning strategy outlined in the next chapter can be justified.

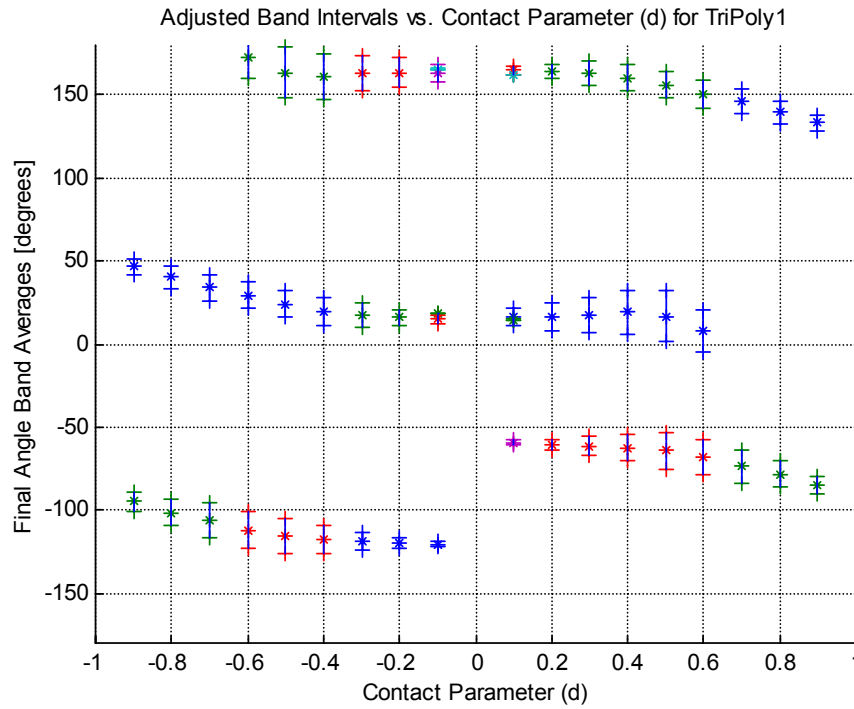


Figure 3-8 Adjusted band intervals vs. contact parameter .

### 3.5– Effects of Friction

In addition to creating configuration maps to represent the quasi-static motion of the triangular polygons studied, it was desired to briefly explore the effects of friction at both the surface ( $\mu_s$ ) and the contact ( $\mu_c$ ) interfaces and verify hypothetical notions.

#### 3.5.1– Surface Friction

According to Peshkin and Sanderson [17], the surface friction does not affect the overall motion of the sliding part. Hence, to verify the proposed motion model and the proper response from the Matlab simulation two random sets of trials were executed. The

results are outlined in Table 3-3 showing that the final angle  $\theta_f$  is indeed the same regardless of the value of the surface friction coefficient  $\mu_s$ .

**Table 3-2 Comparison of interval widths, Adjusted vs. Experimental**

Contact Parameter ( $d$ )	Simulation Bands' $\theta_f$ Means ( $m$ )	Simulation Bands' $\theta_f$ Standard Deviation ( $\sigma$ )	Adjusted Bands	Adjusted Bands' Widths	Bands' Widths Differences
-0.3	-119°	5.53°	(-125° -113°)	11°	5°
	17°	7.17°	(10° 24°)	14°	-1°
	162°	10.65°	(151° 173°)	21°	2°
-0.1	15°	2.71°	(12° 18°)	5°	-3°
	165°	5.32°	(160° 170°)	11°	6°
	-121°	1.52°	(-123° -119°)	3°	0°
0.1	17°	5.30°	(12° 22°)	11°	-4°
	165°	2.72°	(162° 168°)	5°	-4°
	-59°	1.52°	(-61° -57°)	3°	1°
0.3	17°	10.34°	(7° 27°)	21°	2°
	163°	7.01°	(156° 170°)	14°	1°
	-61°	5.59°	(-67° -55°)	11°	6°
0.4	19°	13.24°	(6° 32°)	26°	-12°
	160°	8.15°	(152° 168°)	16°	-7°
	-62°	8.38°	(-70° -54°)	17°	7°
0.7	n/a	n/a	n/a n/a	n/a	n/a
	146°	7.65°	(138° 154°)	15°	-4°
	-74°	10.34°	(-84° -64°)	21°	5°

**Table 3-3 Effects of varying the friction coefficient at the surface interface.**

Surface Friction ( $\mu_s$ )	Contact Parameter ( $d$ )	Initial Angle, $\theta_i$	Rotated Angle, $\Delta\theta$	Final Angle, $\theta_f$
0.05	0.1	0°	20.4799°	20.4799°
0.50	0.1	0°	20.4799°	20.4799°
0.95	0.1	0°	20.4799°	20.4799°
0.05	0.1	45°	117.9312°	162.9312°
0.50	0.1	45°	117.9312°	162.9312°
0.95	0.1	45°	117.9312°	162.9312°

### 3.5.2 – Contact Friction

To investigate the effects of varying the coefficient of friction at the point of contact ( $\mu_c$ ) a number of simulation trials were executed for individual initial angles  $\theta_i$ . Table 3-4 outlines these results. The notion of a larger  $\mu_c$  implies a larger friction cone which further implies more sticking occurring between the pin and the part.

Hence, the results of varying  $\mu_c$  show that the amount of rotation, labeled *Rotated Angle* ( $\Delta\theta$ ), is directly affected by the contact coefficient of friction. In short, a larger contact coefficient of friction forces a larger amount of rotation  $\Delta\theta$  of the part against an overhead pin because of an enlarged friction cone, while a smaller coefficient allows for more slipping along the pin resulting in less rotation of the polygon throughout the entire period of contact between the polygon and the pin.

**Table 3-4 Effects of varying the coefficient friction at the point of contact.**

Contact Friction ( $\mu_c$ )	Contact Parameter ( $d$ )	Initial Angle, $\theta_i$	Rotated Angle, $\Delta\theta$	Final Angle, $\theta_f$
0.25	0.1	45°	-29.4044°	15.5956°
0.50	0.1	45°	117.9312°	162.9312°
0.75	0.1	45°	115.9378°	160.9378°
0.25	-0.1	0°	17.9290°	17.9290°
0.50	-0.1	0°	-119.9347°	-119.9347°
0.75	-0.1	0°	-115.0143°	-115.0143°
0.25	-0.1	135°	29.4297°	164.4297°
0.50	-0.1	135°	-117.8473°	17.1527°
0.75	-0.1	135°	-115.5383°	19.4617°
0.25	-0.1	225°	-62.2784°	162.7216°
0.50	-0.1	225°	-62.3447°	162.6553°
0.75	-0.1	225°	-64.2205°	160.7795°

### 3.6 – Discussion and Conclusions

This chapter has looked at the results of the quasi-static motion using the proposed model from Chapter 2 and carried out a comparison with the results obtained through numerous

experimental trials. The last section of this chapter also explored briefly the effects of friction at the sliding surface interface as well as at the contact point.

First, the motion of the given polygonal part about its COR loci tips was assessed against the motion resulting about the minimum energy CORs. A comparison with equivalent experimental trials led to the conclusion that the motion of the part cannot be constrained to behave as if it rotated about the loci tips, but instead the part will choose to move about the point representing the least amount of dissipated energy due to sliding about the support surface. Therefore, using the loci tips is not a realistic approach towards modeling the motion of the polygon moving against an overhead stationary pin.

Then, configuration maps were created to represent the motion of the part for any given contact configuration, that is, any initial orientation  $\theta_i$  and any contact parameter  $d$ . Configuration maps were created again, for motion about the COR loci tips, the minimum energy CORs, and the equivalent experimental trials. Comparison of the bands' widths in all these configuration maps led to the conclusion that the simulation bands  $B_j$  using the minimum energy CORs showed larger widths than their experimental equivalents, and these differences were attributed to the idealistic assumptions of *normal pressure distribution* and *constant contact friction*, where no distinction is made between static and dynamic friction. Therefore, a simple empirical method to adjust the simulation bands  $B_j$  to fit more closely to the experimental results was devised and implemented.

Lastly, effects of friction were observed through simulation runs. First, it was confirmed that friction at the surface interface between the part and the supporting/sliding surface did in fact not affect the motion of the part as presented in [17]. Then, the friction effects were observed at the contact interface between the part and the pin. Here, it was noted that a larger coefficient of friction led to greater amounts of rotation, while smaller coefficient values led to a greater amount of slip of the part with respect to the pin which also corresponds to less rotation overall.

# Chapter 4

## Planning

This chapter explores the development of the planning strategy for the purpose of part orienting using overhead pins. Part orienting was defined as the process of aligning a batch of parts to be assembled in a desired or unique configuration from an unknown initial configuration as illustrated in Figure 1-1 and shown here again for convenience in Figure 4-1.

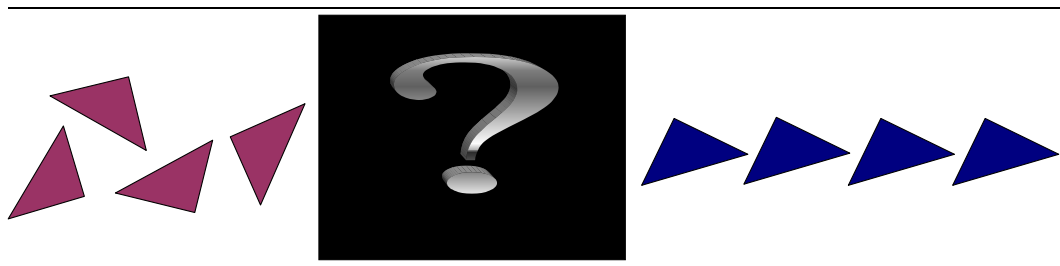


**Figure 4-1 (Copy of Figure 1-1) Orienting parts from unknown initial to final unique configuration.**

In this study, the goal of planning is to find a sequence of pins that will orient a given polygonal planar part from a random initial state to a final orientation set as illustrated in Figure 4-2. Thus, in this chapter a planning strategy is developed and implemented. For this purpose, configuration maps are used, as they encapsulate the physics of an operation, such as a part contacting a pin. Planning with configuration maps was introduced in [18], where series of interactions are mapped by combining the maps corresponding to each individual operation. Here, the development of the search tree used in the planning process is explained, its implementation presented and the results outlined.



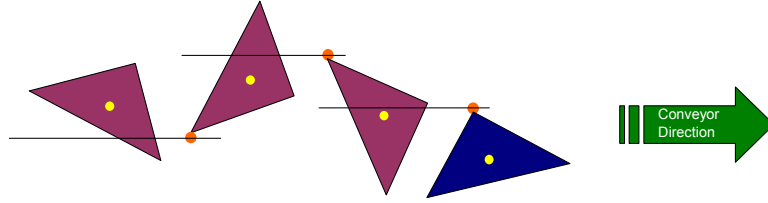


Figure 4-2 (Copy of Figure 1-3) Orienting with overhead pins: the concept.

#### 4.1– Planning with Configuration Maps

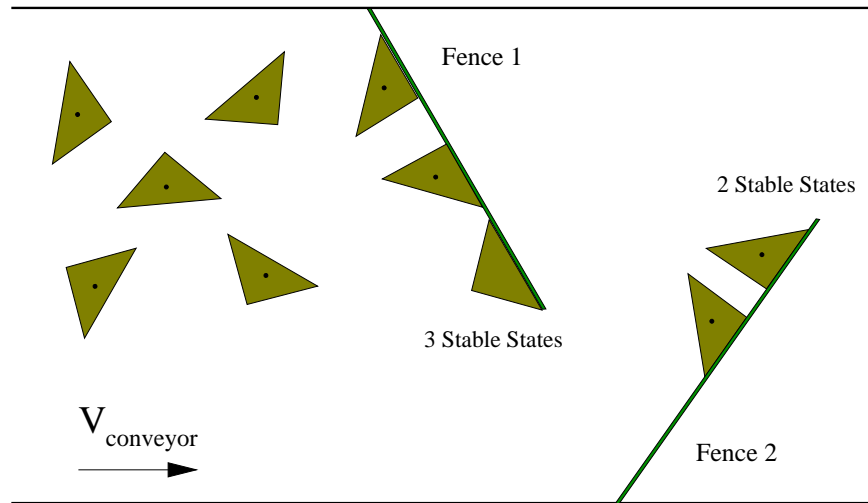
Each configuration map represents a single action pertaining to the overall behaviour of the part, where a single action corresponds to the part contacting a single pin at an initial orientation  $\theta_i$  and resulting in a final orientation  $\theta_f$  at the end of contact. Then, the interaction of a polygonal part with a series of obstacles such as pins (or fences as in [18],[21] and illustrated in Figure 4-3) can be amalgamated into a single configuration map as first presented by Peshkin and Sanderson. This new map is represented by the combination of the individual maps representing the individual obstacles. For example, from [18] and [21], if the part contacts a fence with map  $M_1$  and then a fence with map  $M_2$ , the combined map after the two fences is given by

$$\begin{aligned} M_{21}(\phi_i, \phi_f) &= M_2 M_1 \\ &= \vee_{\beta} \{M_2(\beta, \phi_f) \wedge M_1(\phi_i, \beta)\} \end{aligned} \quad (4-1)$$

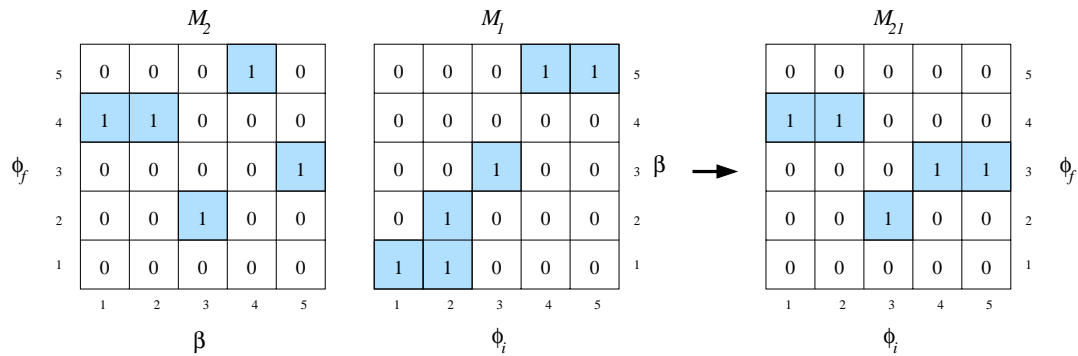
Where both  $M_1$  and  $M_2$  are binary maps<sup>1</sup>,  $\wedge$  is logical intersection,  $\vee$  is logical union and  $\beta$  is an index to facilitate the binary multiplication [21].

Figure 4-4 illustrates an example of two maps represented as 5x5 arrays that combine as per expression (4-1).

<sup>1</sup> A binary map is composed of rectangular bands  $B_j$  and  $K_j$ , where for a given initial orientation  $\theta_i$ , a range of possible (1-possible, 0-not possible) final orientations are computed [21].



**Figure 4-3** Illustration of orienting with fences, where random initial orientations are reduced to three stable orientations on the first fence and later reduced to two orientations on Fence 2. Fence 1 may be represented by configuration map  $M_1$  and Fence 2 as map  $M_2$  in expression (4-1).



**Figure 4-4** Sample illustration of map combination as described in expression (4-1). The resultant map  $M_{21}(\phi_i, \phi_f)$  is a composition of maps  $M_1(\phi_i, \beta)$  and  $M_2(\beta, \phi_f)$ .

Moreover, the search plan developed by Peshkin and Sanderson is applicable to fences because all initial random orientations are guaranteed to contact the first fence, and reduced to the number of *bands* as in map  $M_1$ . Then through the consecutive sequence of fences, success is reached when a configuration map with a single band is found indicating that all initial orientations result in the same final orientation.

Unfortunately, orienting with overhead pins cannot take advantage of the planning strategy presented in [18]. Complications arise due to uncertainty in the COM

positioning of each part and to the contact parameter that affects the interaction between polygonal parts and the overhead pins, and thus a different approach must be taken.

Furthermore, following the principle of using configuration maps for part orienting from [18], the main difference lies in the fact that in this study the combined maps for each tree represents only the transition of one initial state to a final orientation as opposed to all the combined initial states to a final orientation.

#### 4.1.1 – Complications due to COM Positioning and the Contact Parameter

Orienting with fences offers the guarantee that all parts at initial unknown configurations (positions and orientations) contact the first fence and are reduced to a set of stable equilibrium states (refer to Section 2.18) on this fence (Figure 4-3), which is represented by the  $\theta_f$  bands on map  $M_f$ . However, orienting with pins does not offer that guarantee.

Orienting with pins does not offer the ability to reduce all initial random configurations to one set of bands as do fences because any position of the first pin over the conveyor belt does not guarantee to contact every part; thus leaving the uncertainty of initial part configuration still at large after one pin. Then, even if the first pin in the sequence is placed as to offer the guarantee that any initial random configuration contacts this pin, the range of results is dependent on the location of the point of contact with respect to the part's COM. That is, the  $\theta_f$  results after the first pin will depend on the contact parameter of the given contact configuration. Since the contact parameter can be anywhere within the specified values  $[0.1, 0.9]$  and  $[-0.1, -0.9]$ , the possible  $\theta_f$  outcome may correspond to any of the bands  $B_j$  in any of the configuration maps for each respective value of  $d$ . Thus, instead of reducing the uncertainty initially present due to the unknown random initial configurations this approach increases the uncertainty. Consequently, orienting with pins poses the difficulty that to determine the outcome after contact with a pin, it is necessary that the initial configuration be known or approximated. More specifically, it is of interest to approximate the part's COM location so as to

approximate the perpendicular distance to the pin locations, and hence determine the contact parameter  $d$  and its corresponding configuration map to use in the planning phase. It is therefore essential to know or at least limit the range of contact configurations initially possible.

#### 4.1.2 – Reducing the Random Initial Configurations

All polygons possess stable equilibrium states dependent on the polygon's geometry corresponding to the minimum points in the radius function plots as seen in Figure 2-15(c) and (d). Thus, to reduce the initial uncertainty due to the initial random  $\theta_i$  and unknown COM positioning, the stable equilibrium states of the given part are used as the “initial states” measured from a common starting point. Further, this common point will serve as the global zero reference from which pins and the parts' COMs are measured throughout the planning search. For illustration purposes, these states can be attained by using a curved fence as designed by Brokowski et al in [7], and shown in Figure 4-5 reducing the asymmetrical triangular polygon TriPoly2 to its three stable equilibrium states. Note that the use of such a fence would demean this study and it is thus not intended for implementation.. In the future development of a part orienter using overhead pins, an array of pins to either “capture” or “guide” the random parts into their stable equilibrium states need be used.

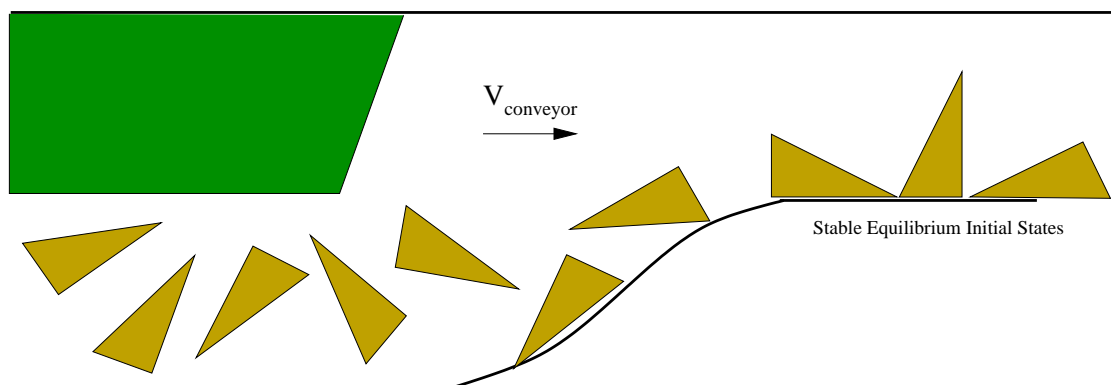


**Figure 4-5** Curved fence used to reduce the part's initial random orientations to natural resting states.

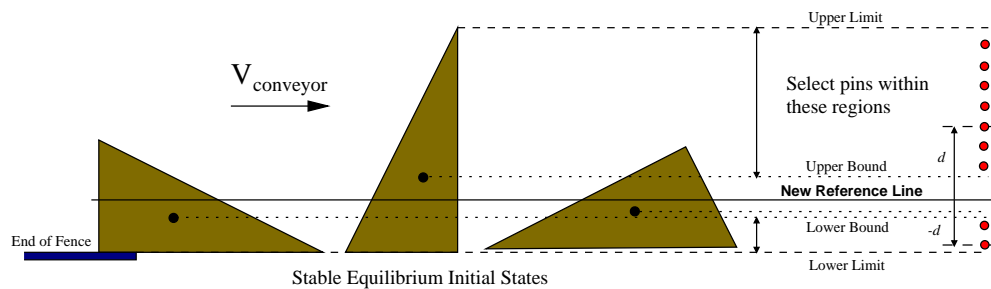
## 4.2 – The Search Tree

For the orienting process it is assumed that parts are fed one at a time and that any one of the initial stable equilibrium states, as in Figure 4-5, each with a different COM position with respect to the zero reference point, can occur. Thus, any planning strategy developed must be a common solution to any of the part's initial states for a given polygonal part.

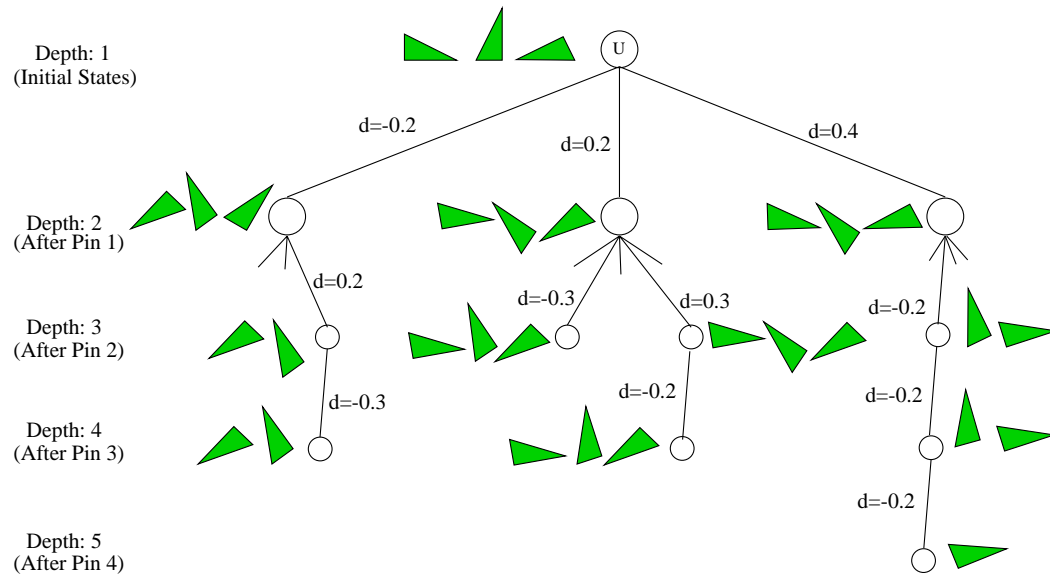
### 4.2.1 – The “Moving” Pins Method: Following Peshkin and Sanderson's Approach

Figure 4-6 illustrates the three initial states for TriPoly2 with their respective COM positions. Here, grouping all three initial states requires that a new reference line of all the possible COM positions is used, where this reference line is determined by calculating the average of the all the COMs bounded within the COM intervals of each state. This reference line, labeled “New Reference Line” in Figure 4-6, is then used to approximate pin locations and hence determine the appropriate values of  $d$  and their corresponding configuration maps to be used for all three initial states.

In the search for a solution, a single tree is then expanded where the parent node includes all three initial states and each branch represents the approximated contact parameters as illustrated in Figure 4-7. Each child node that follows shows the orientations of all states, and success found when a node shows all three states with the same final orientation, also represented by a configuration map with a single band.



**Figure 4-6 Combining initial states of polygon TriPoly2. Note the large bounded region by the upper and lower positions of the part's COMs as well as the resulting error in the “New Reference Line” due to the averaging of the COMs positions.**



**Figure 4-7** Tree expansion illustrating the adaptation of Peshkin and Sanderson's method combining all initial states.

This search method follows the principles introduced by Peshkin and Sanderson in [18]. An addition required for this problem however, is that in order to guarantee the prediction of CW or CCW rotation of the part, it is desired that any pin considered be located strictly “above” or “below” the part's COMs. Thus, a region bounded above by the “highest” COM and below by the “lowest” COM is used to select the pins (see Figure 4-6), and only those pins outside this region are considered.

Preliminary work done by exploring this method grouping all initial states together in the search for a map with a single band, quickly led to the conclusion that it does not suit the problem. Figure 4-6 showed the approximation of a common reference line for the COM positions of all initial states. Now, Figure 4-8 illustrates how the implementation of this method can lead to incorrectly approximating the perpendicular distance between the part's COM and the possible pin location, which in turn leads to incorrectly selecting the contact parameter  $d$ . Here, if the contact parameter  $d$  is wrongly selected, then the corresponding configuration map to be used in the search is also

incorrectly incorporated in the planning strategy. And in the end, the search results can provide invalid solutions that will lead to failure in the part orienting process.

Therefore, it was concluded that due to the varying COM positioning for each initial state of a given polygon, it is not possible to adapt the search method used in [18] pursuing a configuration map with a single band when orienting with overhead pins.

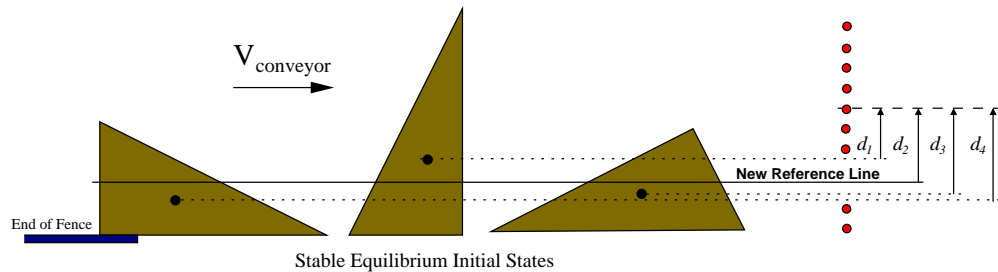


**Figure 4-8** Referencing the pins from the “New Reference Line” for all states shows how the determining the contact parameter can lead to incorrect approximations. Here,  $d_2$  is the value used for all three states, while the values of  $d_1$ ,  $d_3$  and  $d_4$  are quite distinct. Improper referencing leads to improper use of configuration maps in the planning search.

#### 4.2.2 – The “Fixed Pins” Method

In this section a new search method is explored after having rendered the notion of a configuration map with a single final orientation band inappropriate for the planning strategy using overhead pins. For this purpose, a breadth search method referred to as the “fixed pins” method is chosen. Please note that this search method is a “brute-force” search method which explores all possibilities. Also, this is a non-deterministic planner in the sense that it expands to a prescribed depth rather than stopping upon finding a solution. Lastly, due to the variation in COM positioning for the polygon's initial states, two key items are noted:

1. A separate tree must be expanded for each stable equilibrium initial state as illustrated in Figure 4-9. This is done for the purpose of avoiding the incorrect selection of contact parameter values by using an approximated single reference

line for all the combined COM positions of a given part as in the previous method. Thus, by dealing with each initial state separately the uncertainty from the combined COM locations is reduced.

2. The pins selected in the successful orienting sequence must be common to all the initial states of the given polygon. Because each initial state is handled separately at first, the possible locations of the pins must be common to all initial states of the given polygon. Thus, the pins must be assigned global locations over the conveyor belt and hence be common to all initial states as in Figure 4-10. The distance between one pin and another adjacent pin (e.g. pin labels 6 vs. 7) is equivalent to the discretized value of the contact parameter, that is, the equivalent distance to  $d = 0.1$ . To ensure that indeed the correct contact parameter is used in the search process because of the perpendicular distance estimation between the part's COM and possible pin location, the value of  $d$  must be finely discretized. In this study, the value remains at 0.1.

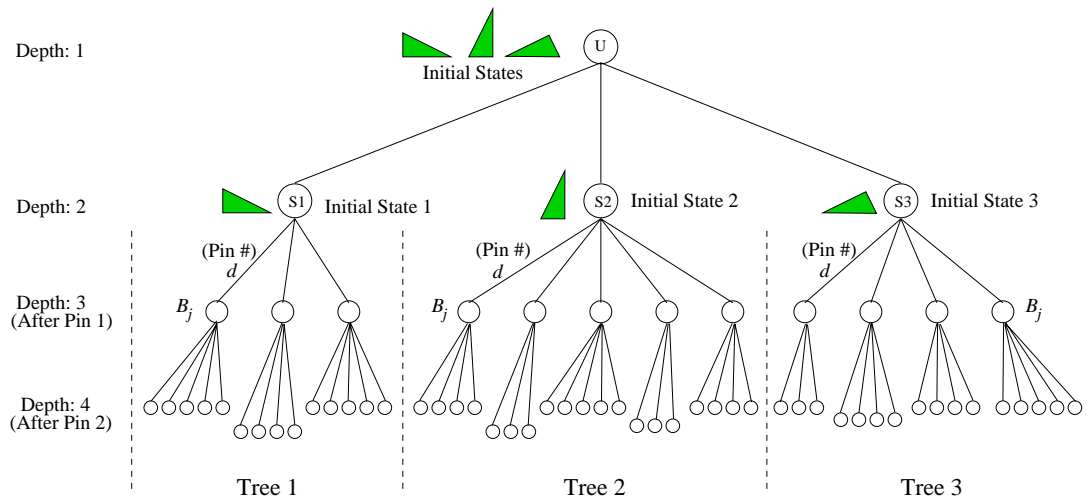


**Figure 4-9 Combined tree after expanding separately for each initial state. The nodes represent the part's orientations throughout the orienting process, particularly, nodes labeled S1, S2 and S3 represent the three initial states of the given polygon (TriPoly2). The branches on the other hand, indicate each possible contact parameter value pertaining to a pin's position that can contact the part and take it from an initial orientation to a final orientation.**



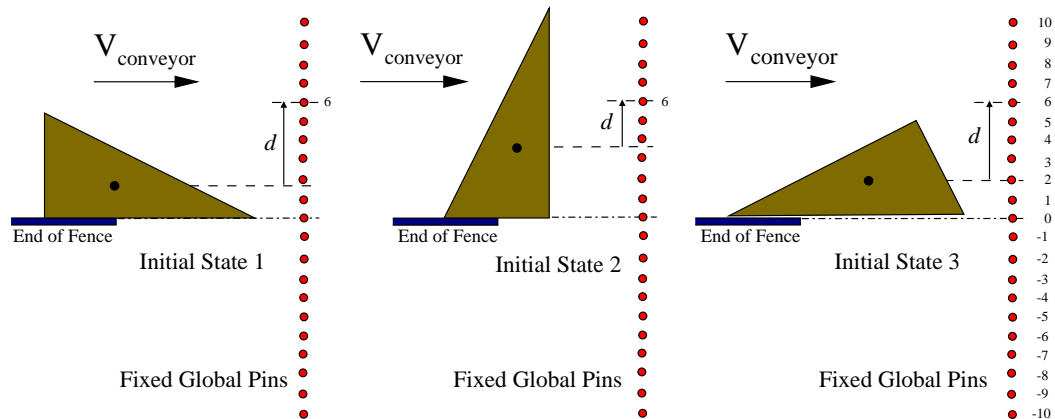


**Figure 4-10 Initial states for triangular polygon and fixed global pins.** For each initial state shown in the figure, the “Fixed Global Pins” represent the possible locations of the pins common to each state.

#### 4.2.2.1 – Expanding the Trees

A key item in the “fixed pins” method is that a tree is expanded for each initial state.

Thus, for the case of TriPoly2 as illustrated in Figure 4-9, three initial states exist and consequently three trees are separately expanded. Note that all trees are expanded to a prescribed depth, as follows:

1. For each initial state, determine the part’s initial orientation  $\theta_i$  prior to contact with the first pin. For the cases other than the first pin that follow in the pin sequence, determine the  $\theta_i$  orientation range.
2. Then, for each state, determine the interval  $COM_j$  (as defined in equation (2-18)) corresponding to the orientation of the part.
3. Calculate the COM reference line for this state by averaging the upper and lower bounds of the COM interval  $COM_j$ .
4. From the COM reference line measure the approximate perpendicular distances to all pin locations, selecting only those outside the  $COM_j$  bounded region as illustrated in Figure 4-11 to guarantee that the pin contacts the part

strictly “above” or “below” its COM, and hence guarantee a prediction of a CW or CCW rotation.

5. Use the approximated pin distances to select the representative contact parameter values (i.e.  $[0.1, 0.9]$  and  $[-0.1, -0.9]$ ), and hence the representative configuration maps. These contact parameter values represent the selected pins that correspond to the branches in each tree extending to a corresponding child node from the parent node.
6. For each configuration map match the initial state  $\theta_i$  interval with the initial orientation intervals  $K_j$  (as defined in equation (2-17)) and find the resulting final orientation outcome range,  $B_j$  (as defined in equation (2-16)), as illustrated in map  $M_I$  of Figure 4-12, where  $\theta_i$  matches with  $K_3$  and the resulting final orientation set is  $B_3$ .
7. Having established the final orientation band  $B_j$ , calculate the resulting COM range  $COM_j$  pertaining to  $B_j$ , and record the part's and pins' positions globally with respect to the initial zero reference point to be later compared against the data of the other initial states' trees.

For expansion of the tree to the next depth level, the final orientation interval  $B_j$  is used as the orientation input in Step 1 while the resulting  $COM_j$  is used for determining the new local COM reference line in Step 3.

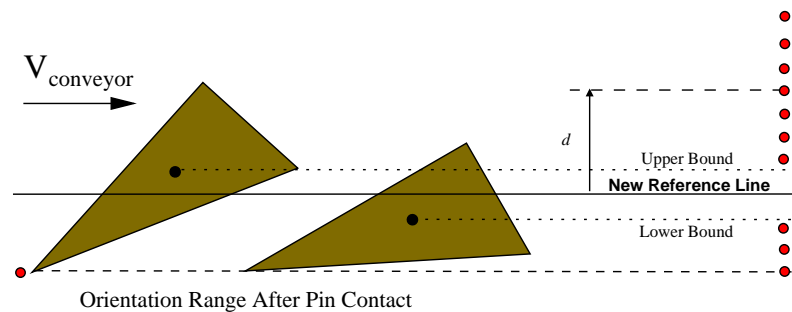


**Figure 4-11 Bounding the COM region to select pins resulting from the range of  $\theta_j$  orientations after pin contact.**

As stated in Step 4, as the tree is expanded, pins are selected so that they are guaranteed to be located “above” or “below” the possible COMs given the width of the COM position interval  $COM_j$  as in the following expression:

$$|da| > \frac{|COM_j(\max) - COM_j(\min)|}{2} \quad (4-2)$$

Where the distance  $da$  was defined in Section 2.13 as the true perpendicular distance between the COM and the pin, and it is dependent on the geometry of the polygonal part.

The purpose of selecting pins outside this bounded region, as illustrated in Figure 4-11, is to avoid cases where the part's motion is incorrectly predicted. For example, referring to Figure 4-11, if a pin was selected between the reference line and the upper bound, and a CCW rotation was predicted (i.e. part moves “under” the pin) because the pin is located “above” the COM reference line, when in fact the actual COM position is at or near the upper bound, then the motion of the part would be a CW (i.e. part moves “over” the pin). Since within this region the exact position of the COM is not known, the part could rotate either CW or CCW without certainty, resulting in the motion of the part being incorrectly predicted.

The principle of using configuration maps for part orienting follows from [18], the difference being that the resulting combined map for each tree represents only the transition of one initial state to a final orientation as opposed to all the combined initial states to a final orientation. The process of matching and combining configuration maps is depicted in Figure 4-12.

Also, special cases of the planning process in this work are instances in which the part does not make contact with the polygon. In such cases  $\theta_i = \theta_f$ , and their ranges are  $NC_j$  as in expression (3-1). The process of combining configuration maps in the presence of  $NC_j$  ranges is illustrated in Figure 4-13.

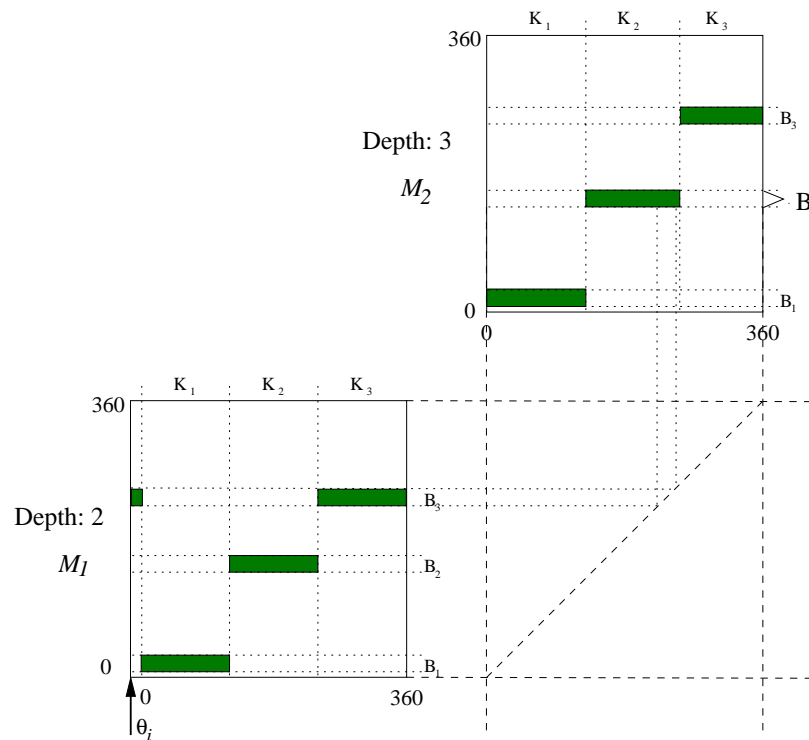


**Figure 4-12** Combination of configuration maps  $M_1$  and  $M_2$  given an initial state of  $\theta_i$  resulting in an outcome of orientation set  $B_2$ .

### 4.2.3– Searching for a Solution

After expanding each tree individually, these trees are then combined into one single larger tree as in Figure 4-9. The set of initial states of the polygon are contained in the parent node of this larger tree from where the branches, each being the separate tree for each initial state, expand. The purpose of combining the trees into a single larger one is to search for a solution that satisfies the task of part orienting from all initial states to one single final orientation.

#### 4.2.3.1 – Defining the Solution

A solution exists when a sequence of pins, common to all initial states, is found such that it drives all given initial states into the same single final orientation set.

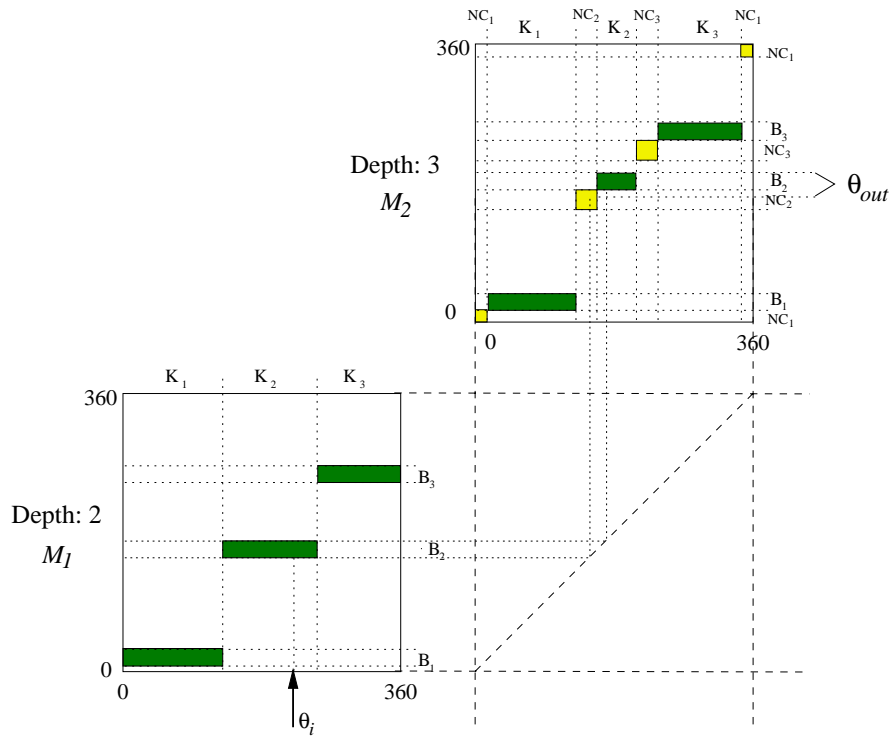


**Figure 4-13** Combination of configuration maps  $M_1$  and  $M_2$  given an initial state of  $\theta_i$  resulting in an outcome of orientation set  $\theta_{out}$  that is a combination of the no-contact region  $NC_2$  and the band  $B_2$

#### 4.2.3.2– Searching by Backtracking

Having expanded all the trees in a “brute” manner, that is, exploring all possibilities, all final nodes of the prescribed depth must be investigated to search for a solution within all these allowed possibilities. To start, a set of criteria is used to filter any unwanted nodes.

1. Eliminate any nodes that have a final orientation band with a width greater than  $30^\circ$ . A width of  $30^\circ$  was decided upon after observing the band widths in Table 3-1 and Table 3-2. Based on the numbers in these tables, the average width of the tabulated intervals without adjustment (Table 3-1) is  $24^\circ$ , while the average width of the tabulated adjusted intervals (Table 3-2) is  $13^\circ$ . A width of  $30^\circ$  allows for the combination of bands from the various configuration maps corresponding to each pin in the sequence. This width is still a rather large width, but it is representative of the limitations that orienting with overhead pins presents.

2. Eliminate any nodes that have a final orientation band identical to their initial orientation. This case implies that the part never contacted a pin; hence, defeating the purpose of orienting with pins.

After filtering the unwanted nodes, then referring to Figure 4-14, the search for a solution is carried out as follows:

1. For the prescribed depth (i.e. Depth 6 in the figure) search all the remaining final nodes. According to the known orientation bands (i.e.  $B_j$ , where  $j=1,2,3$ ) for the given polygon as explained in Section 3.3, nodes having equal or similar final orientation intervals are selected and grouped together. Each node is flagged with the corresponding  $j$  set number (i.e.  $j=1,2,3$ ) regardless of what tree they are present in. For example, the shaded nodes at Depth 6 in the figure belong to the final orientation band  $B_1$ , referred to from here on as “Orientation 1”.
2. For each grouped set  $B_j$  verify that nodes with the same flag number do indeed exist in all the expanded trees. Cases in which a particular  $B_j$  is found only some of the trees but not all are discarded because this particular orientation is not achievable by all initial states, and it is therefore not a solution. For example, Orientation 2 in the figure is found in the first two trees, but not the last one, and since this orientation is not possible for Initial State 3, the process of part orienting in this cases is not successful. Keep those nodes present in all trees with the same flag number, and then backtrack for each one.
3. After backtracking for each set  $B_j$ , search for the same sequence of pins from initial state to final orientation throughout each tree that yield the same orientation set  $B_j$ . In Figure 4-14, the sequence of pins (7,0,3,7) is found in all trees and result in the final orientation, Orientation 1.

And thus, as per the definition of the solution above: *a solution exists when a sequence of pins, common to all initial states, is found such that it drives all given initial states into*

the same single final orientation set. Figure 4-14 illustrates the parent tree for TriPoly2 with the selected nodes outlining the successful sequence of pins, all these are shaded.

### 4.3– Planning Results

Implementing the “fixed pins” method described in the previous sections yielded successful results to orient a given polygonal part from all its initial states to a single orientation set. However, this search method also yielded only partial results for the case of a polygon with some geometrical symmetries where two orientation sets were found, but not a single one. This section presents the successful and partial planning results obtained for TriPoly2 and TriPoly1 respectively. Also, experimental results are tabulated to validate the operation of the selected pin sequences.

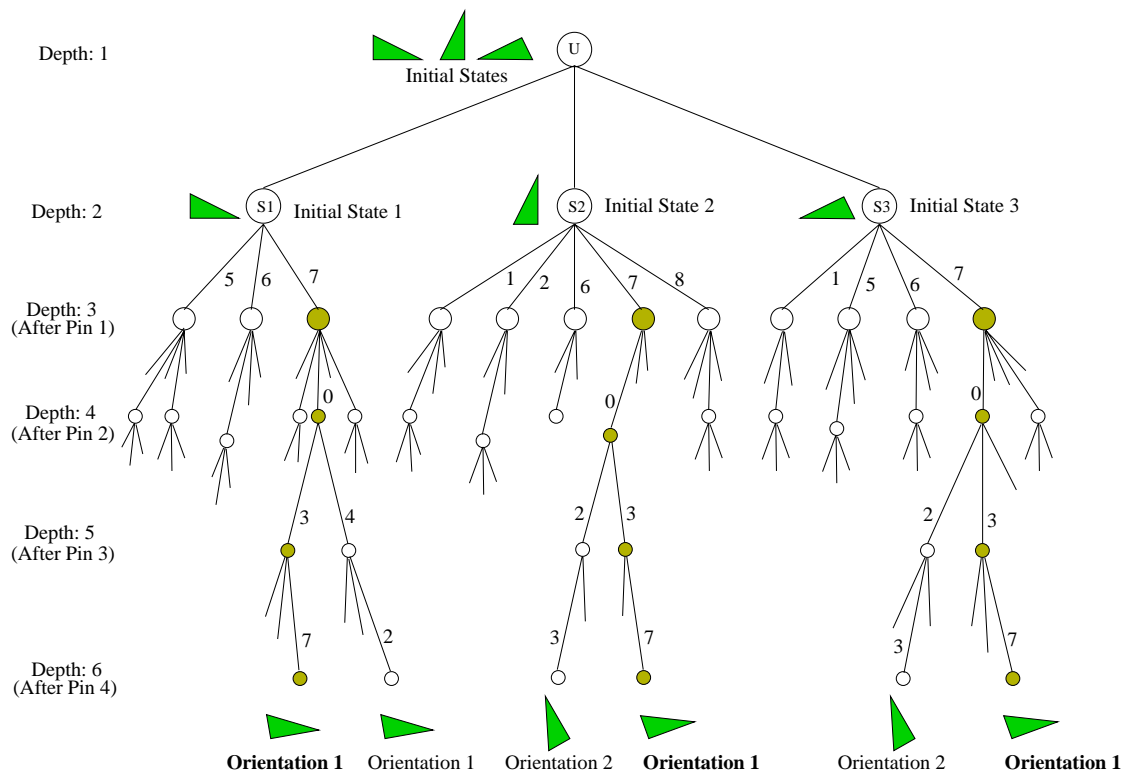


**Figure 4-14** Expanded tree showing selected (shaded) nodes after backtracking. The numbers assigned next to the node represent the global pin labels of the pin sequence.

### 4.3.1– Successful Results

Figure 4-15 shows the successful results for all three initial states of the given asymmetrical triangular polygon, TriPoly2, using a sequence of four pins. Note that the final orientations of the polygons are contained within the corresponding  $B_j$  interval, labeled “Orientation 1”. Thus, they are seen as belonging to a final orientation set rather than a unique orientation, where the final width of this band was found to be  $[14^\circ, 36^\circ]$ .

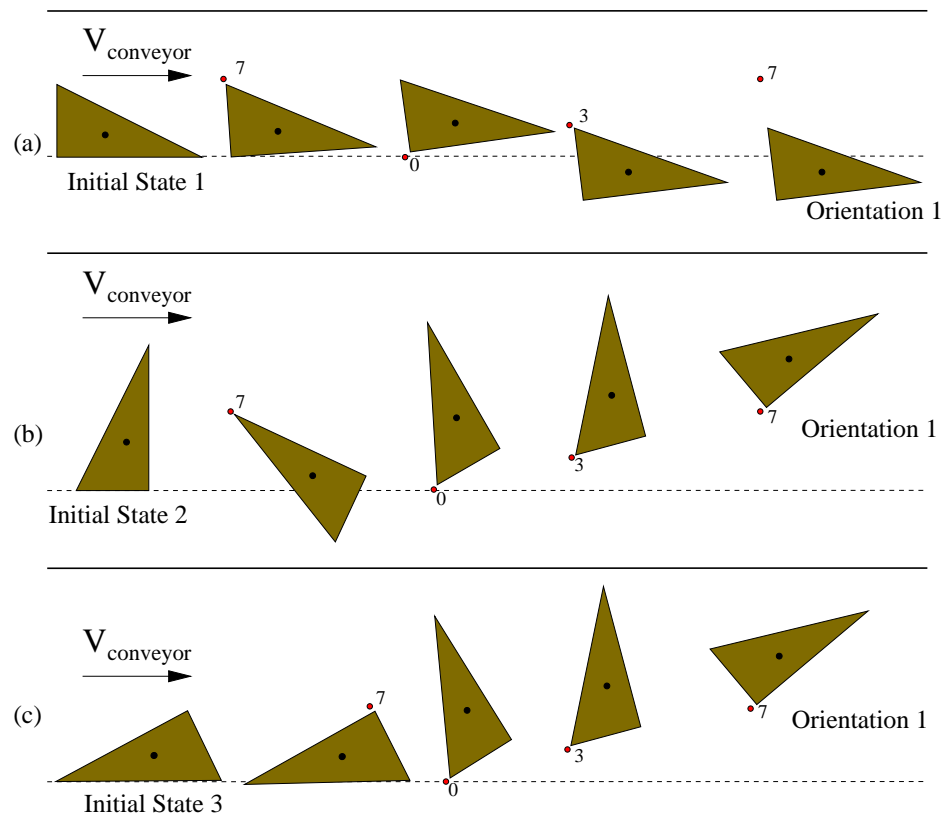


**Figure 4-15** Pin sequence used to orient TriPoly2 from its three initial states to a final orientation. The pin labels are global labels indicating the common selected pins used to orient all initial states.

A search for less than four pins yielded partial solutions only, that is, yielded solutions for two initial states ending in the same final orientation, but not all three. Consequently, a search for less than four pins failed to find a full solution, and four pins



is seen as the shortest sequence found to orient the given polygon from its set of initial states to one final orientation set.

#### 4.3.2 – Partial Results

On the other hand, if a part has certain symmetries, a single final orientation band may not be found. This was the case found for TriPoly1 illustrated in Figure 4-16 where two final orientation bands, labeled “Orientation 1” and “Orientation 2” in the figure, were found using a sequence of three pins. A search with four pins yielded similar results and no solution towards a single orientation set. Searches greater than four pins were not possible due to the massive size of the brute-search tree expansion.

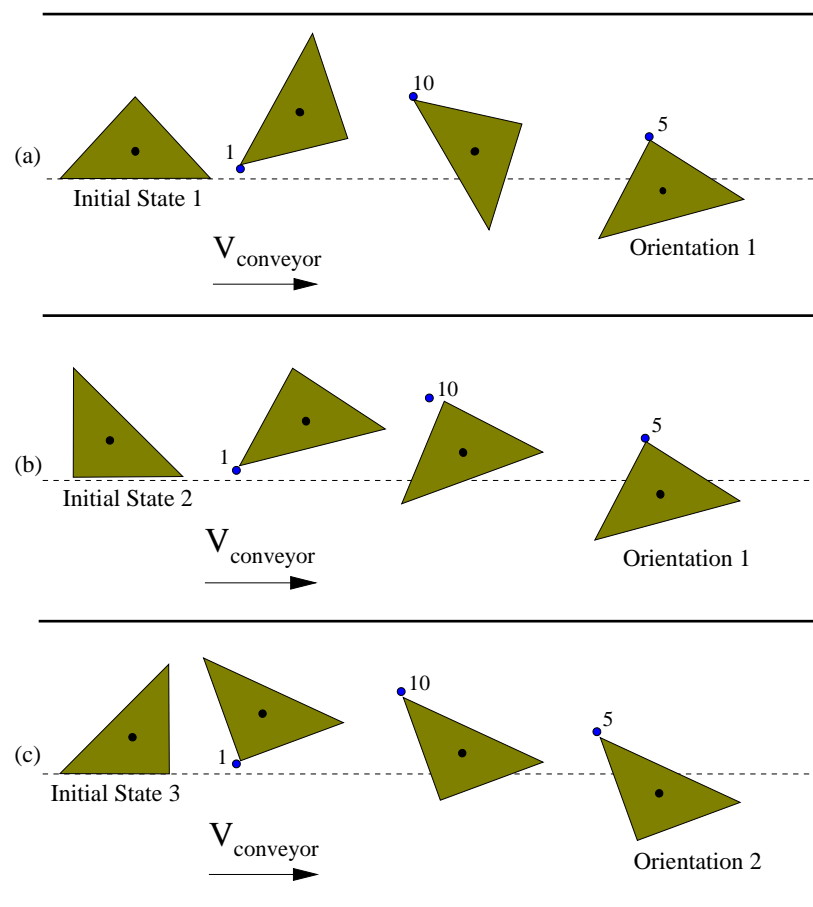


**Figure 4-16** Pin sequence orienting symmetric triangular polygon TriPoly1 from its three initial states to two final orientations, Orientation 1 in (a) and (b) and Orientation 2 in (c).

### 4.3.3 – Experimental Trials

The planning results for both TriPoly2 (Figure 4-15) and TriPoly1 (Figure 4-16) polygons were verified experimentally. Where verification indicates that the pin sequence found through the planning search was tested experimentally, and the final orientation of the polygon fed through this sequence was measured and inspected. For each initial state of each polygon 10 trials were carried out using the experimental setup depicted in Figure 3-4, and all arrived to the same orientation  $\theta_f$  within  $\pm 3^\circ$ .

More specifically, the experimental trials for TriPoly2, revealed that the final orientation  $\theta_f$  for Initial State 1 (Figure 4-15(a)) averaged  $11^\circ$ , while Initial States 2 and 3 (Figure 4-15(b) and (c), respectively) averaged  $36^\circ$  and  $37^\circ$ . Given the  $\pm 3^\circ$  uncertainty in the angle measurements during the experimental trials these averaged values marginally correlate with the interval  $[14^\circ, 36^\circ]$  obtained in the planning search.

Similarly, TriPoly1, showed differences within the same orientation, Initial State 1 (Figure 4-16(a)) resulted in an averaged orientation angle of  $36^\circ$  while Initial State 2 (Figure 4-16(b)) averaged  $10^\circ$ . The other final orientation for Initial State 3 (Figure 4-16(c)) averaged  $152^\circ$ .

Table 4-1 below summarizes the experimental trials carried out for both TriPoly2 and TriPoly1.

Table 4-1 Pin sequences experimental results

Polygon	Trials	Successes	Failures	Reason
TriPoly2	10 x 3	29	1	Pin caught vertex
TriPoly1	10 x 3	30	0	n/a

Therefore, TriPoly2 was successfully oriented to one single orientation set. The only failure in the trials occurred when one of the part's vertices came into contact with the pin as opposed to the planned edge and rotated in the opposite direction than

expected. This case of vertex vs. edge contact is treated in the following chapter as an empirical study to distinguish between the two.

Furthermore, having reduced the initial states of TriPoly1 to two possible final orientations, it is now of interest to distinguish the final orientations obtained in Figure 4-16, and hence find out the final result. For this purpose the use of a force/torque sensor to be discussed in the following chapter is explored.

#### **4.4 – Discussion and Conclusions**

This chapter has shown that planning a sequence of passive static overhead pins to orient a given polygonal planar part is possible. Here, a solution was found for the triangular polygon TriPoly2 to orient the part from all its initial states to a single orientation set. Also, partial results were found for the symmetrical triangular polygon TriPoly1, where its initial states were reduced to two final orientation sets. Typical lengths of pin sequences found in this study for successful and partial results varied between 3 and 4 pins.

In conclusion, the process of planning along with the study of the part's motion against an overhead pin is a contribution of this thesis towards the future development of a more complete hybrid mechanics-based part feeder. Of future interest is the notion of reducing the sequence length by introducing active (i.e. pins with sensing) as well as dynamic (i.e. moving) pins.

In addition, it must be noted that the brute-search non-deterministic planner presented in this chapter poses weaknesses. Most importantly, since a tree must be expanded for each initial state of the given polygon, the search grows immensely making it memory expensive and time consuming. Therefore, for a polygon with  $n$  stable equilibrium initial states,  $n$  trees would be needed to carry out a full brute-search as proposed by the Fixed Pins method. This is clearly inefficient to implement, and for

future development of a part feeder using overhead pins it would be of interest to reduce the search breadth of the presented method.

Also, as future work the development of an online planning strategy is recommended in conjunction with the incorporation of sensing as will be discussed in the chapter to follow. For this purpose, it is necessary to delineate which items need to be solved offline and which can be solved online. Using the offline information and the continuous gathering of data online, the system can be developed so that the overhead pins can intelligently collaborate with each other towards the common goal of part orienting. Furthermore, in terms of a holonic system, groups of pins serving as layers rather than individual pins can be used to gather information, thereby “training” the system to become an intelligent more capable system.

## Chapter 5

### Introducing the Force/Torque Sensor

The objective of this chapter is to investigate the use of force/torque sensing information for the purpose of orienting with overhead static pins to complement the planning search results obtained in Chapter 4. Particularly, it is of interest to use this sensing information to distinguish final orientations where partial results are obtained as in Section 4.3.2.

First, this chapter describes the approach taken in using the force/torque sensor to complement partial planning results, more specifically, how the sensing information is gathered based on speculated expectations due to contact interaction between the given polygon and the *active* (i.e. sensorized) pin. Then, an empirical method is developed for comparing the sensor results with simulation results, and thus determining the final orientation(s) of the polygon. Finally, the force/torque sensor is used to distinguish between two different possible types of contact, that is, whether the part contacts the pin along an edge or on a vertex. This investigation stems from the experimental results in Chapter 4 where one trial failed to reach its final orientation because the part contacted on a vertex and rotated in the opposite direction than expected.

#### 5.1– Purpose and Approach

It is hypothesized that the force/torque (F/T) profiles, the plots of the resulting forces and torques, over the period (i.e. duration) of contact between the part and the pin can provide information on the motion of the part against the pin. The sensor used in this study is the *Intelligent Multi-Axis (Nano) Force/Torque Sensor System – Model FT3629* from ATI – Industrial Automation [33]. This sensor was selected for its high sensitivity necessary for

measurements of force and torque throughout the contact interaction between the polygonal part and the pin in a quasi-static environment.

In this study, the F/T sensor is used where a single final orientation is not found using the proposed search method described in the previous chapter for geometries with certain symmetries, but the possible final orientations are known. Therefore, it is of interest to develop the ability to detect and distinguish either the possible final orientations of a given polygon or the initial states that result in any of these final orientations; hence, identifying which final orientation will result. For this purpose, the F/T profiles depicting the part and pin contact interaction are investigated.

The F/T profiles depend on the geometry, pressure distribution and motion of the part, as well as its orientation prior to contact with the pin. Thus, for a given polygonal part with constant and even pressure distribution and constant friction coefficient  $\mu_c$  at the point of contact, distinct profiles are expected due to the part's diverse motion following different contact parameter values and initial orientations. Figure 5-1 illustrates the force  $\mathbf{F}$  (same as force  $\vec{F}$  in Table 2-1) acting on the pin and measured by the sensor. This measured force, direction and magnitude, dependent on the contact configuration between the part and the pin, generates the shape of the force/torque profiles to be used in this study.

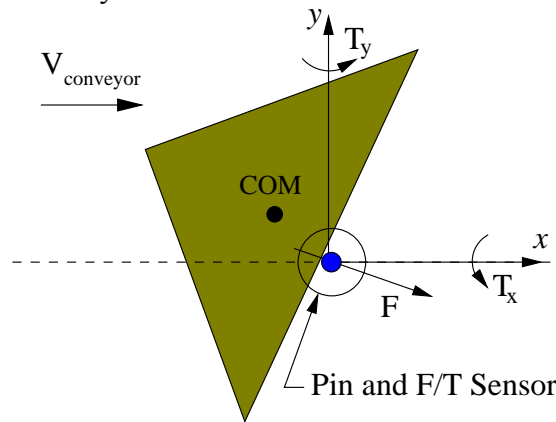


**Figure 5-1 Applied force  $\mathbf{F}$  resulting from part contacting pin with sensor, and the respective torques about the  $x$ - and  $y$ -axes.**

The setup for this exercise consists of the F/T sensor mounted on a pin as depicted in Figure 5-2(b); thus, making the pin an *active* pin (i.e. sensorized). Figure 5-2(c) illustrates the setup used for data collection in the experimental trials, and Figure 5-2(a) illustrates a typical overhead passive pin without a sensor for comparison purposes.

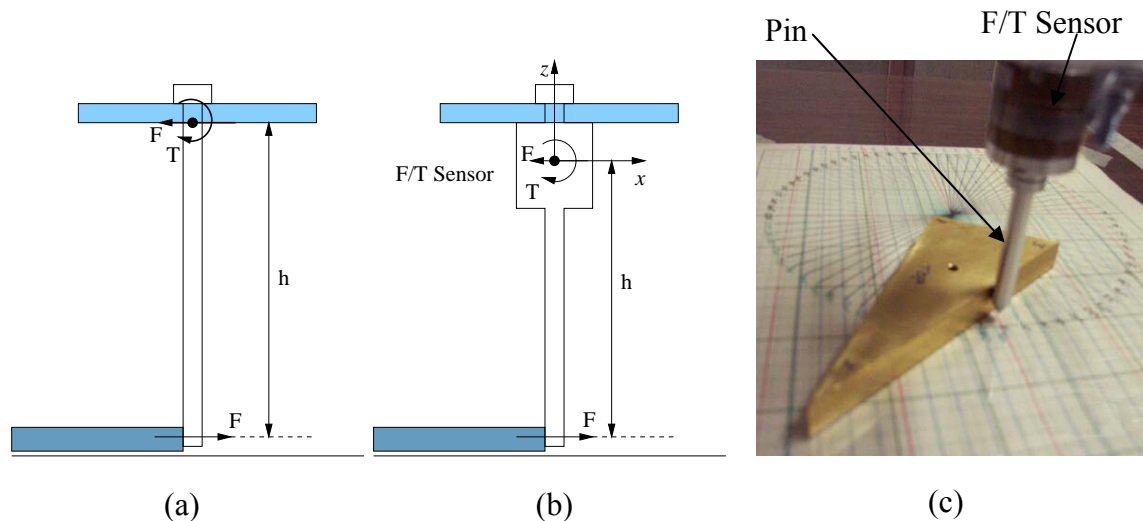


**Figure 5-2** Side-view schematics of pin without sensor in (a) and with F/T sensor in (b). Also, (c) depicts pin and sensor setup used in the experimental trials.

## 5.2 – Force/Torque Profiles

The direction of the applied force  $\mathbf{F}$  depends primarily on the orientation  $\alpha$  of the edge to make contact with the pin, as well as the coefficient of friction,  $\mu_c$ , at the point of contact. In theory however, it is usually not possible to tell the precise direction of the applied force. Thus, start by assuming that the force acts normal to the edge in contact with the pin, this is the case when no friction at the point of contact exists. However, in the presence of friction,  $\mu_c > 0$ , the results vary and two situations are possible as previously described in Section 2.10. The part either sticks and rotates against the pin at the contact point or the part slides past the pin, up or down, depending on the direction of rotation. When the part slips, the force acts along one of the friction cone extremes. On the other hand, when the part sticks, the force will act anywhere within the friction cone.

### 5.2.1 – Approximating the Direction of Force

In order to approximate the direction of the instantaneous applied force on the static pin, some observations are made. It is noted that in the frictionless case, the direction of force is perpendicular to the contact edge and since this edge is parallel to the instantaneous COR locus tip vector  $\vec{r}_{tip}$  as previously shown in Figure 2-4(a); hence, the force is also perpendicular to the instantaneous COR locus tip vector  $\vec{r}_{tip}$ . On the other hand, for cases where  $\mu_c > 0$ , it is further observed that when the part slips up or down with respect to the pin, the direction of force is parallel to the corresponding friction cone limit  $f_{up}$  or  $f_{down}$ , which in turn is perpendicular to the corresponding COR locus tip  $\vec{r}_{tip}^{up}$  or  $\vec{r}_{tip}^{down}$ , as previously shown in Figure 2-12. Finally, in the cases where the part sticks and the instantaneous COR lies on the sticking line (see Figure 2-12), the force is assumed perpendicular to the sticking line and thus the force lies inside the friction cone as expected; subsequently, the force is perpendicular to the vector  $\vec{r}$  between the part's COM and the COR.

The observations outlined above lead to the assumption that the applied force  $\mathbf{F}$  is perpendicular to the vector  $\vec{r}$ . Therefore, for the purpose of creating a force profile representing the motion interaction of the part against the static pin, let the instantaneous applied force  $\mathbf{F}$  at the contact point be perpendicular to the instantaneous vector  $\vec{r}$  in the presence of friction due to the infinitesimal rotation  $\delta\theta$ , and so,

$$\mathbf{F} \perp \vec{r} \quad (5-1)$$

Figure 5-3(a) illustrates the direction of  $\mathbf{F}$  for the depicted contact configuration without friction, and (b) illustrates the assumed direction of  $\mathbf{F}$  in the presence of friction in the slip condition, while (c) illustrates the sticking case.



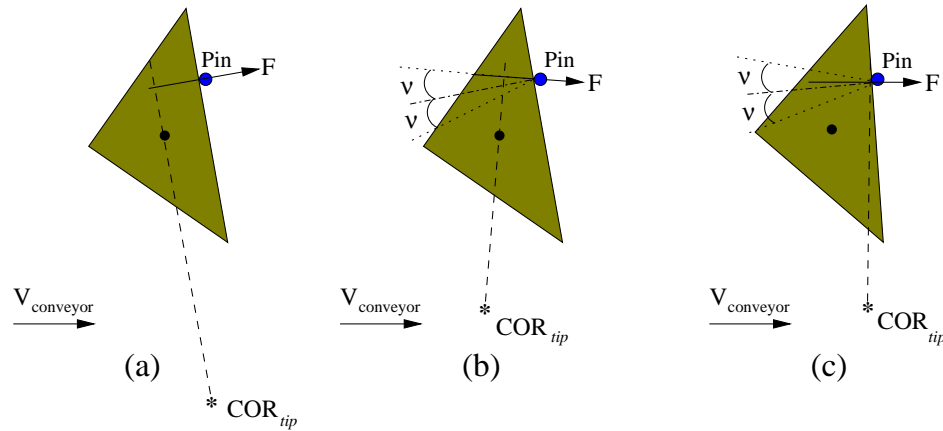


**Figure 5-3** Approximated direction of applied force at the point of contact, (a) without friction and (b) with friction.

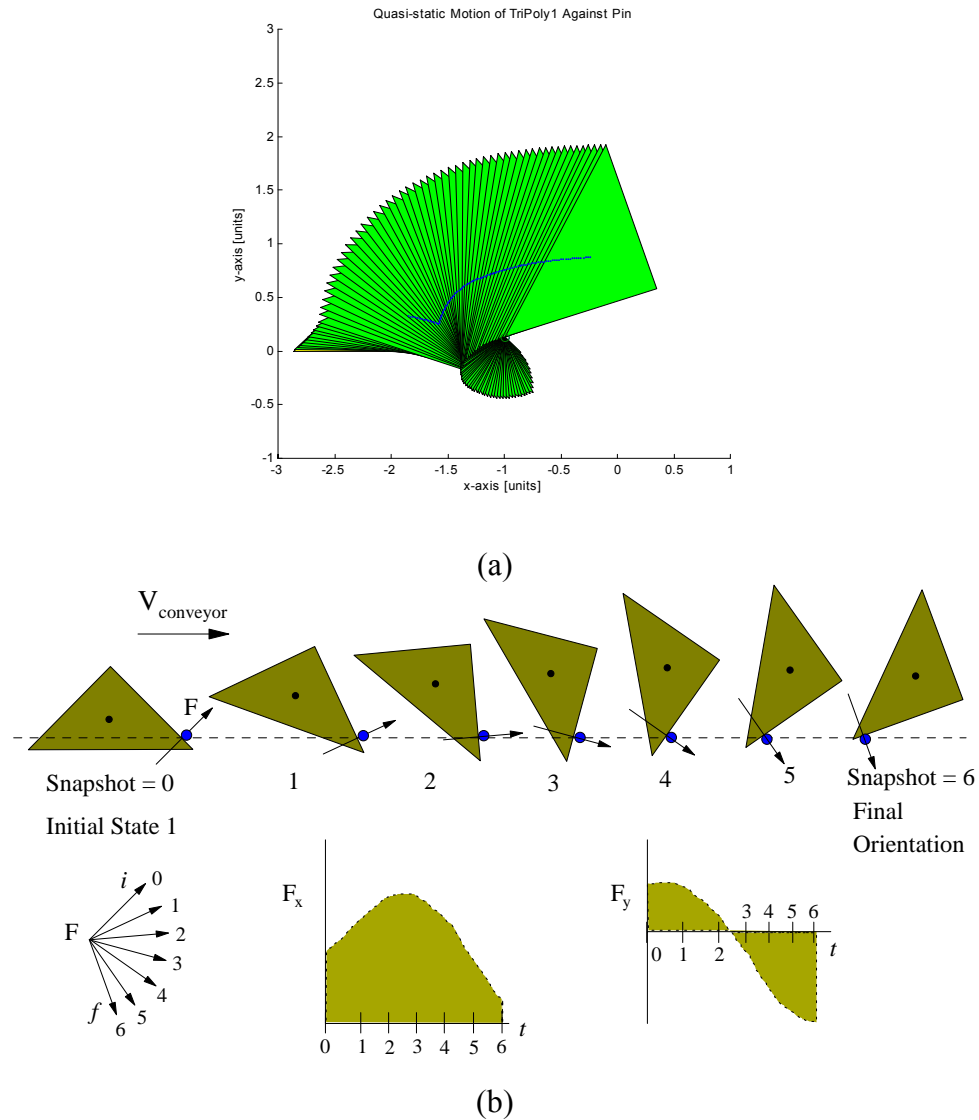
### 5.2.2 – Expectations due to Contact Interaction

Figure 5-4(a) illustrates the motion of TriPoly1 against a static passive pin as the conveyor carries the part in the positive  $x$ -direction. Figure 5-4(b) shows “snapshots” of this motion along with the expected direction of the instantaneous forces resulting from the interaction between the part and the pin throughout the period of contact. Figure 5-4(b) also depicts the expected force profiles as a result of the change in direction of the  $x$ - and  $y$ -force components over the period of contact.

At this point, it must be emphasized that the key interest in this study are the F/T profiles outlining the motion of the part against the pin. More specifically, of interest are the shapes of these plots representing the change in force/torque direction and magnitude as a result of the part moving against the overhead pin. Since the exact magnitude values are not of concern then all F/T magnitudes are normalized.

Moreover, using the force direction assumption, simulations to approximate the instantaneous applied forces throughout the period of contact were executed for numerous impact parameter values. These simulations follow the same quasi-static motion simulation procedure outlined in Chapter 2 and implemented in Chapter 3 where configuration maps were generated. The results from these simulations were then used to

create the desired F/T profiles by plotting the  $x$ - and  $y$ - components of the instantaneous forces and corresponding torques over the period of contact.



**Figure 5-4 (a) Motion of part against pin. (b) Snapshots of part motion (labeled 0 through 6) from initial ( $i$ ) to final ( $f$ ) illustrating instantaneous direction of force  $F$  at the distinct contact configurations and the expected force profiles,  $F_x$  and  $F_y$ .**

### 5.3– Static Active Simulation Results

This section presents F/T profiles obtained from simulation results. These simulations investigate the  $x$ - and  $y$ - components of the applied force only because no effects on the

$z$ -direction are expected. Figure 5-5 illustrates the pertinent force/torque profiles for a contact configuration with an initial state of  $\theta_i = 0^\circ$  and a contact parameter  $d = -0.2$  for the given polygon TriPoly1.

Overall, F/T profiles were constructed for all three initial states of TriPoly1, (i.e.,  $0^\circ$ ,  $135^\circ$  and  $225^\circ$ ) as well as its averaged four possible final orientations obtained from Section 3.3 (i.e.,  $20^\circ$ ,  $160^\circ$ ,  $240^\circ$  and  $300^\circ$ ) and using two distinct contact parameter values,  $d = 0.2$  and  $d = -0.2$ .

The simulation results seen here are not real-time; thus, the horizontal axis in each plot does not represent time but the number of iterations. Nonetheless, for comparison against the experimental results, the total number of iterations refers to the “period of contact” between the part and the pin.

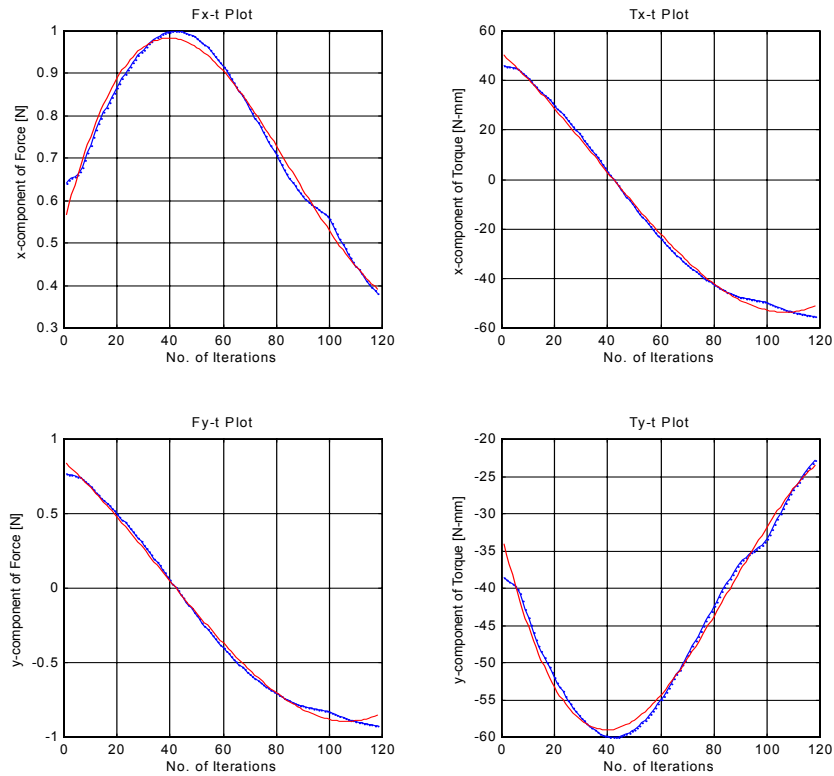


**Figure 5-5** Simulation force/torque profiles for TriPoly1 ( $\theta_i = 0^\circ$  and  $d = -0.2$ ).

## 5.4– Static Active Experimental Results

Having setup (see Figure 5-6) and calibrated the F/T sensor (see Appendix C for the F/T sensor specifications), experimental trials were performed for all initial states and other known orientations of TriPoly1. For each orientation trials using a selected positive contact parameter ( $d = 0.2$ ) and the equivalent negative contact parameter ( $d = -0.2$ ) were performed.

For the experimental trials all six sensor readings available,  $F_x$ ,  $F_y$ ,  $F_z$ ,  $T_x$ ,  $T_y$ , and  $T_z$  were plotted. From these six, of most interest are  $F_x$  and  $F_y$  as well as  $T_x$  and  $T_y$ .  $F_z$  is expected to show noise only and no clear pattern, as ideally no force component will act along the  $z$ -axis.  $T_z$  though could be useful. Given the amount of friction at the contact point, the resulting frictional forces opposing the sticking and slipping motion throughout the period of contact might yield a small amount of torsion on the pin. This torsion translates to a moment about the  $z$ -axis indicating the part's sense of rotation about the pin. Figure 5-7 shows the plots created using the experimental data for all six available sensor readings obtained for the contact configuration  $\theta_i = 0^\circ$  and  $d = -0.2$ .

Of concern is the high level of noise present in the experimental F/T raw data used to plot the profiles in Figure 5-7. A great deal of this noise can be attributed to sensor bias as well as the manual operation of the conveyor belt (i.e. manual turning of the wheel driving the Mylar film canister) resulting in uneven and inconsistent motion. Nonetheless, noticeable trends appear in these plots and it is of interest to “smooth out” the data to plot the changes of force and torque directions as the part moves against the pin. Thus, for the profiles to show visible trends the Moving Averages method (see appendix D1) was applied to “smooth out” the sensor data. Figure 5-8 depicts the force/torque profiles plotted using the smoothed experimental data for the same  $\theta_i = 0^\circ$  and  $d = -0.2$ . Focus is placed on  $F_x$  and  $F_y$  as well as  $T_x$  and  $T_y$ , while  $F_z$  and  $T_z$  are discarded.

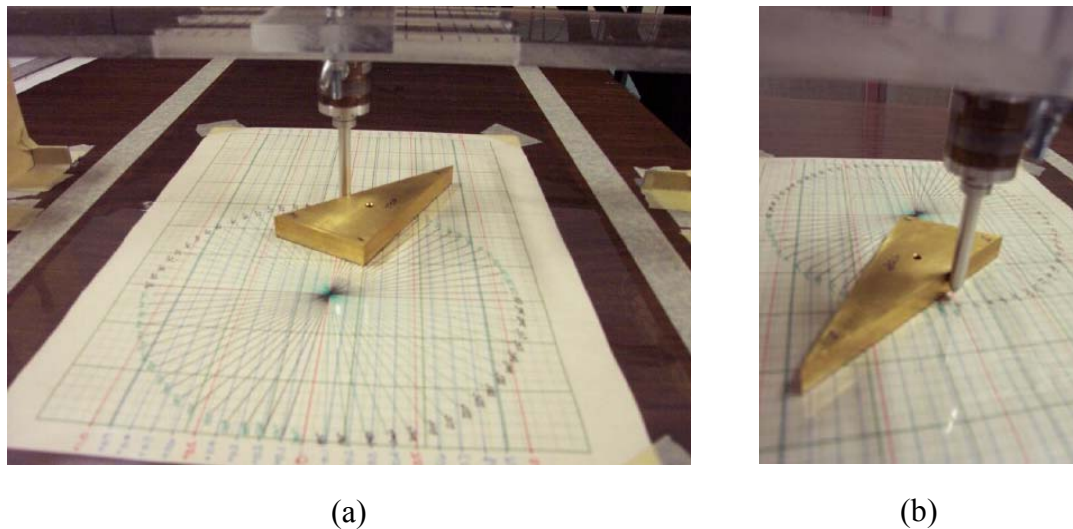
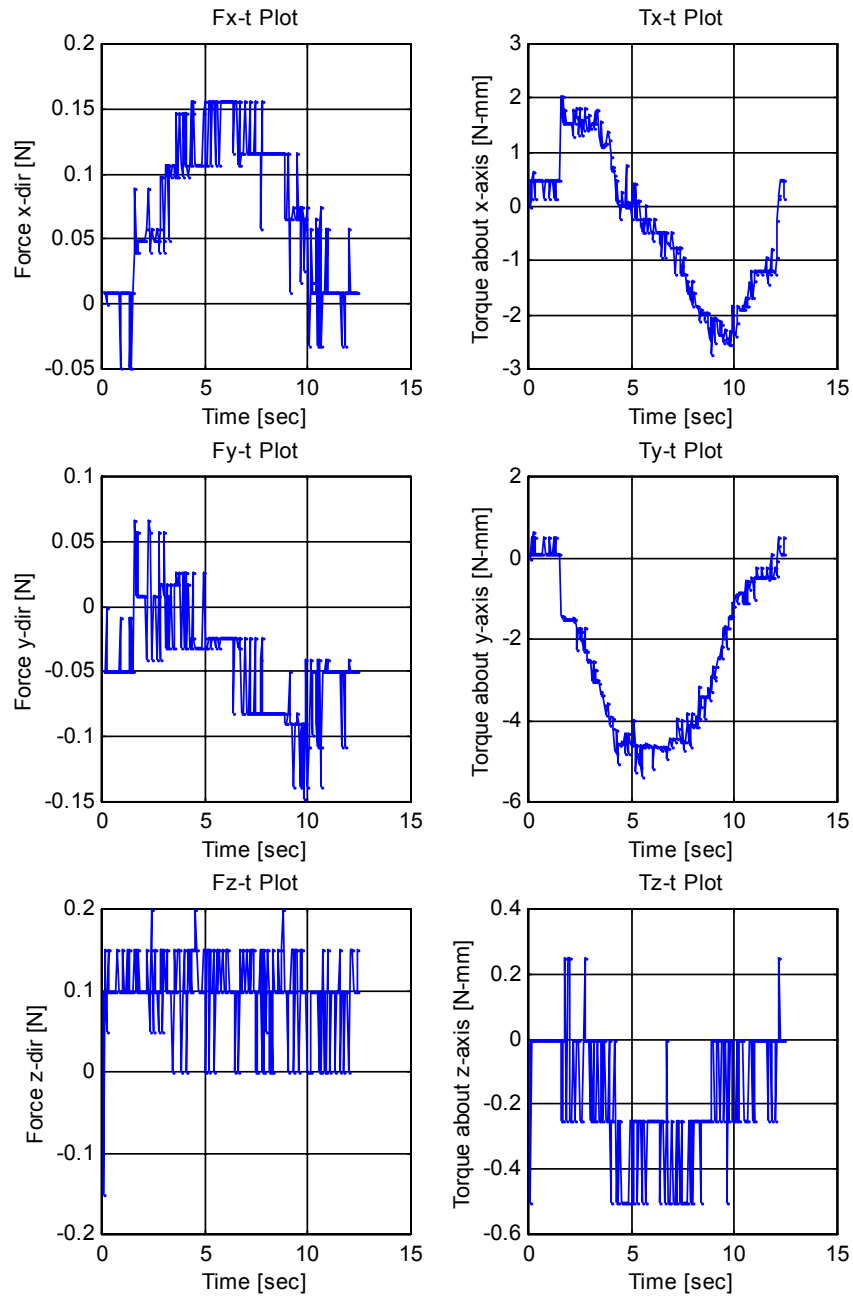


**Figure 5-6** Experimental setup using the F/T sensor on the static pin.

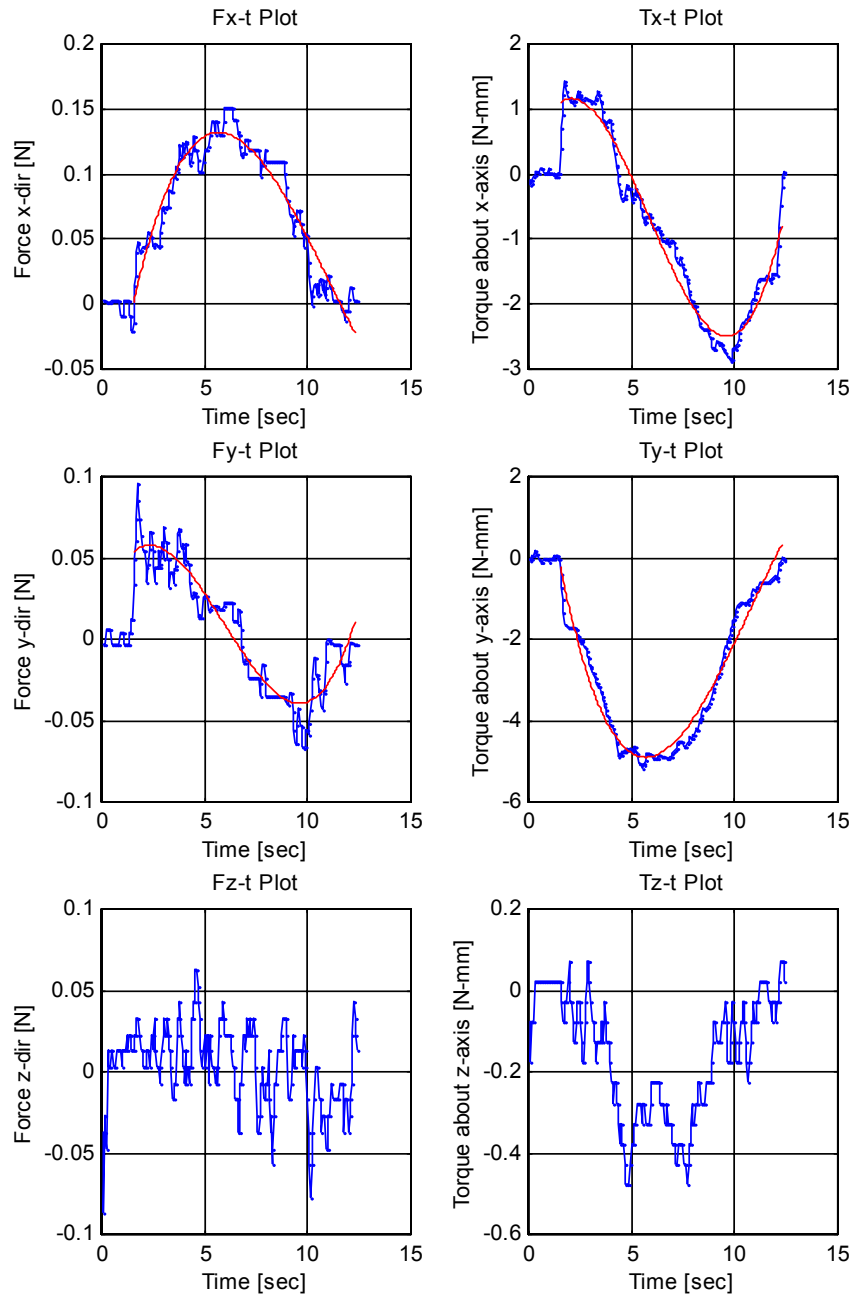
### 5.5– Simulation vs. Experimental F/T Profiles Comparison

After plotting F/T profiles for data obtained through both simulations and experiments it is now of interest to compare their trends. Comparing the trends it is expected that the corresponding contact configuration will be discovered and hence the initial state of the given polygon will be known. For this purpose an empirical method has been devised.

Ideally, in the case of a hybrid part feeder where passive and active pins may be used, the F/T sensor is used to help identify the state and outcome of a polygonal part contacting the static active overhead pin. The proposed plan is such that through the (online) planning process, a set of F/T profiles for an unknown initial state but known contact parameter would be obtained from the active (i.e. sensorized) pin and compared against all equivalent simulation profiles to determine which initial state is present. Depending on the contact configuration between the part and the pin, a single initial state may be found, or the number of unknown possible states simply reduced.

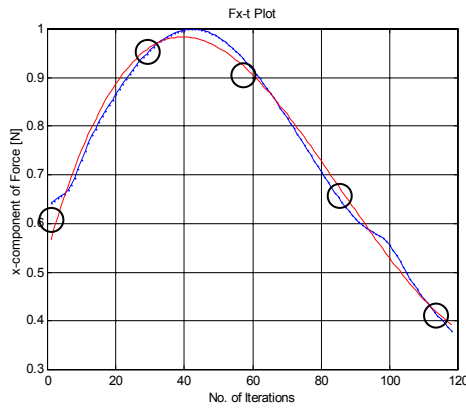
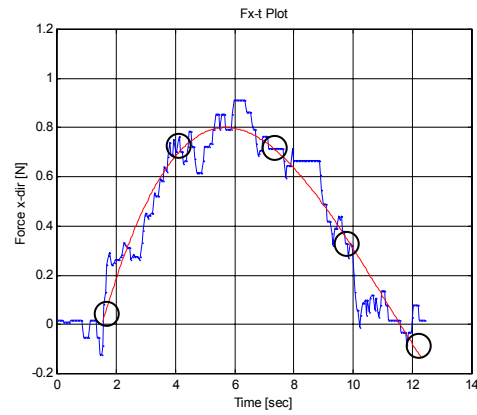
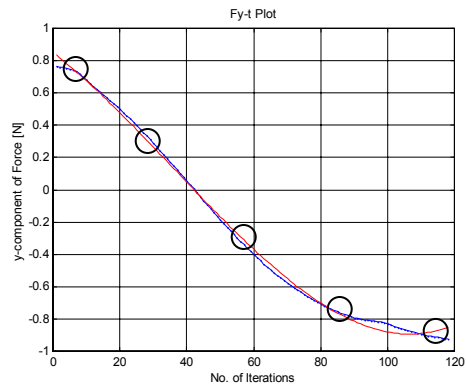
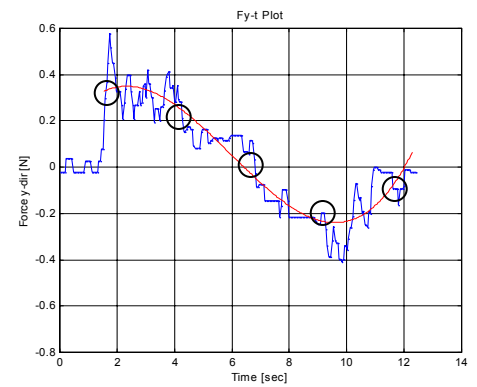


**Figure 5-7 F/T profiles from raw experimental data (  $\theta_i = 0^\circ$  and  $d = -0.2$  )**



**Figure 5-8** Smoothed F/T profiles from experimental data ( $\theta_i = 0^\circ$  and  $d = -0.2$ ) using the Moving Averages method.

Thus, to compare experimental against simulation F/T profiles, polynomials (dotted curves in Figure 5-9(a-d)) are curve-fitted to the plots using the least-squares method (see Appendix D2). Cubic polynomials are chosen and used here for their ability to outline inflection points as well as maximum/minimum points. Furthermore, the 1<sup>st</sup>, 2<sup>nd</sup> and 3<sup>rd</sup> gradients of the fitted polynomials are calculated.

(a) Simulation  $F_x$ (b) Experiment  $F_x$ (c) Simulation  $F_y$ (d) Experiment  $F_y$ 

**Figure 5-9** Force profiles and fitted cubic polynomials for simulation (a,c) and experimental (b,d) for contact configuration:  $\theta_i = 0^\circ$  and  $d = -0.2$ . The bubbles indicate the approximate five regions in each profile used to determine the signs in the first row of matrix  $[S]$ . The actual sign values for both the experimental and simulation matrices are tabulated in Table 5-1.



Then, five distinct regions of points within each curve, as depicted in Figure 5-10, are selected (also shown in Figure 5-9), averaged and the signs of these averaged values resolved. Here, a “sign matrix”  $[S]$  (Equation (5-2)) is generated where the elements are the signs of the averaged values from each of the five selected regions of the  $F_x$  and  $F_y$  profiles and their respective gradients. Hence, this matrix denotes the changes in the force profiles for a part's given contact configuration represented by selected regions throughout the period of contact between the part and the pin.

The sign matrix  $[S]$  is defined as follows:

(5-2)

$$[S] = \text{sign} \begin{bmatrix} (F_x)_1 & (F_x)_2 & (F_x)_3 & (F_x)_4 & (F_x)_5 & (F_y)_1 & (F_y)_2 & (F_y)_3 & (F_y)_4 & (F_y)_5 \\ \nabla(F_x)_1 & \nabla(F_x)_2 & \dots & \dots & \nabla(F_x)_5 & \nabla(F_y)_1 & \nabla(F_y)_2 & \dots & \dots & \nabla(F_y)_5 \\ \nabla^2(F_x)_1 & \dots & \nabla^2(F_x)_3 & \dots & \nabla^2(F_x)_5 & \nabla^2(F_y)_1 & \dots & \nabla^2(F_y)_3 & \dots & \nabla^2(F_y)_5 \\ \nabla^3(F_x) & 0 & 0 & 0 & 0 & \nabla^3(F_y) & 0 & 0 & 0 & 0 \end{bmatrix}$$

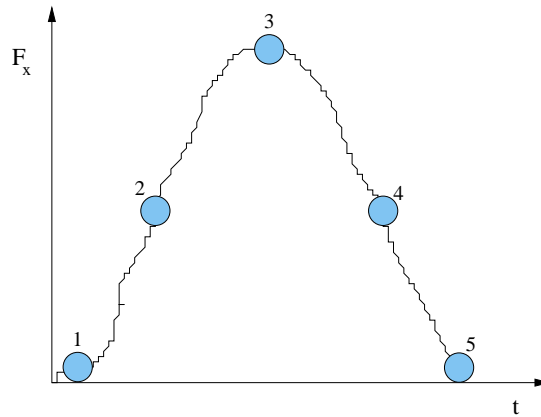


**Figure 5-10** Selected five regions in force profiles used to evaluate curve trends

Having created sign matrices for both simulation and experimental results, a scoring system is then established. Each element of these matrices are compared, and a point is assigned for each matching element describing the curves' behaviour, which in

turn describes the motion of the polygonal part against the static pin. Subsequently, a score out of 40 points is tabulated, where the number of “matches” indicates that the corresponding matrices’ elements were the same for both the simulation and the experimental cases, while the number of “misses” indicates that the compared elements were not equal. As a result, it is of interest to select those cases with higher scores because they are indicative of the same F/T trends profiling the contact and motion of the interaction between the part and the pin. Table 5-1 outlines the comparison between the experimental matrix vs. the simulation matrix corresponding to the profiles shown in Figure 5-9 for contact configuration  $\theta_i = 0^\circ$  and  $d = -0.2$ . The resulting score of this comparison is 35 matches and 5 misses, which when compared to the other scores indicates a good match. The complete comparison results between experimental cases with the possible simulation counterparts are tabulated in Table 5-2, labeled "Exp" and "Simulation" respectively.

**Table 5-1 Experimental vs. Simulation matrix matching comparison. The sign values in the first row of each matrix were obtained from the regions shown in the profiles in Figure 5-9, the rest correspond to the 1<sup>st</sup>, 2<sup>nd</sup> and 3<sup>rd</sup> gradients of the fitted profile curves.**

Experimental ( $d = -0.2$ and $\theta_i = 0^\circ$ )	$\begin{bmatrix} 1 & 1 & 1 & 1 & -1 & 1 & 1 & -1 & -1 & 1 \\ 1 & 1 & -1 & -1 & -1 & 1 & -1 & -1 & 1 & 1 \\ -1 & -1 & -1 & -1 & 1 & -1 & -1 & 1 & 1 & 1 \\ 1 & 0 & 0 & 0 & 0 & 1 & 0 & 0 & 0 & 0 \end{bmatrix}$
Simulation ( $d = -0.2$ and $\theta_i = 0^\circ$ )	$\begin{bmatrix} 1 & 1 & 1 & 1 & 1 & 1 & 1 & -1 & -1 & -1 \\ 1 & 1 & -1 & -1 & -1 & -1 & -1 & -1 & 1 & 1 \\ -1 & -1 & -1 & 1 & 1 & -1 & -1 & 1 & 1 & 1 \\ 1 & 0 & 0 & 0 & 0 & 1 & 0 & 0 & 0 & 0 \end{bmatrix}$

**Table 5-2 Comparison of matching scores from force/torque profiles. “Match” indicates the number of matching elements between Experimental (Exp) and Simulation profiles, and “Miss” indicates the number of non-matching elements.**

Exp		Simulation		Score (/40)		Exp	Simulation		Score (/40)	
$\theta_i$	$d$	$\theta_i$	$d$	Match	Miss	$d$	$\theta_i$	$d$	Match	Miss
$0^\circ$	$-0.2$	$0^\circ$	$-0.2$	35	5	$0.2$	$0^\circ$	$-0.2$	27	13
		$135^\circ$	$-0.2$	35	5		$135^\circ$	$-0.2$	27	13
		$225^\circ$	$-0.2$	28	12		$225^\circ$	$-0.2$	28	12
		$0^\circ$	$0.2$	25	15		$0^\circ$	$0.2$	38	2
		$135^\circ$	$0.2$	24	16		$135^\circ$	$0.2$	27	13
		$225^\circ$	$0.2$	26	14		$225^\circ$	$0.2$	31	9
$135^\circ$	$-0.2$	$0^\circ$	$-0.2$	37	3	$0.2$	$0^\circ$	$-0.2$	31	9
		$135^\circ$	$-0.2$	37	3		$135^\circ$	$-0.2$	31	9
		$225^\circ$	$-0.2$	30	10		$225^\circ$	$-0.2$	26	14
		$0^\circ$	$0.2$	24	16		$0^\circ$	$0.2$	28	12
		$135^\circ$	$0.2$	23	17		$135^\circ$	$0.2$	29	11
		$225^\circ$	$0.2$	25	15		$225^\circ$	$0.2$	31	9
$225^\circ$	$-0.2$	$0^\circ$	$-0.2$	32	8	$0.2$	$0^\circ$	$-0.2$	27	13
		$135^\circ$	$-0.2$	32	8		$135^\circ$	$-0.2$	27	13
		$225^\circ$	$-0.2$	33	7		$225^\circ$	$-0.2$	24	16
		$0^\circ$	$0.2$	23	17		$0^\circ$	$0.2$	36	4
		$135^\circ$	$0.2$	26	14		$135^\circ$	$0.2$	29	11
		$225^\circ$	$0.2$	28	12		$225^\circ$	$0.2$	33	7

Note the left half of Table 5-2, here the experimental initial states with negative impact parameters ( $d = -0.2$ ) are compared against the simulations' initial states with the same contact parameter. For both experimental initial states of  $0^\circ$  and  $135^\circ$ , a high score was calculated when compared against either the  $0^\circ$  or  $135^\circ$  simulation cases indicating good match ups. In the third case, for  $\theta_i = 225^\circ$ , also a slightly higher score was noted when compared against its simulation equivalent. Thus, using the F/T sensor on the first pin with a negative impact parameter value allows for the distinction of either  $0^\circ$  or  $135^\circ$  from  $225^\circ$ . Thereby reducing the number of possible initial states.

On the other hand, the comparisons of the experimental cases with positive impact parameters on the right half of the table don't prove to be conclusive. The initial state of  $\theta_i = 0^\circ$  is the only case in which a good high score match occurs. The other two

have tabulated scores that would lead towards a wrong conclusion or an unclear decision. No known reason could be attributed for this discrepancy. However, this empirical method showed that for a negative contact parameter the initial states can indeed be separated into two groups, and hence, reducing the part's initial orientation uncertainty. Thus, in the planning process a pin sequence that can take advantage of this finding must be selected so as to yield a solution to the orienting problem, and further contribute towards the overall design of a more complete hybrid mechanics-based part feeder. Overall, the comparison of F/T profiles can help in the part orienting process as first hypothesized.

### 5.5.1 – Indistinguishable Orientation States

It was shown that the initial states of TriPoly1 can be reduced to two groups, but a question arises: why can't Initial State1 ( $\theta_i = 0^\circ$ ) and Initial State 2 ( $\theta_i = 135^\circ$ ), be identified apart? The answer to this question is attributed particularly to the angle  $\alpha$  that each contact edge makes with the action line and the resulting direction of the applied force  $\mathbf{F}$  at contact. Figure 5-11 illustrates these two orientations; note the similarities in angles and direction of forces at the point of contact. Moreover, due to the contact configuration between the part and the pin, the motion that follows the initial contact (i.e. CW or CCW rotation) is the same for a given  $d$ . And as a result, the F/T profiles, illustrated in Figure 5-12(a-d), exhibiting the motion and contact interaction for both  $\theta_i = 0^\circ$  and  $\theta_i = 135^\circ$  are alike, and consequently, they cannot be differentiated using the empirical comparison method proposed.

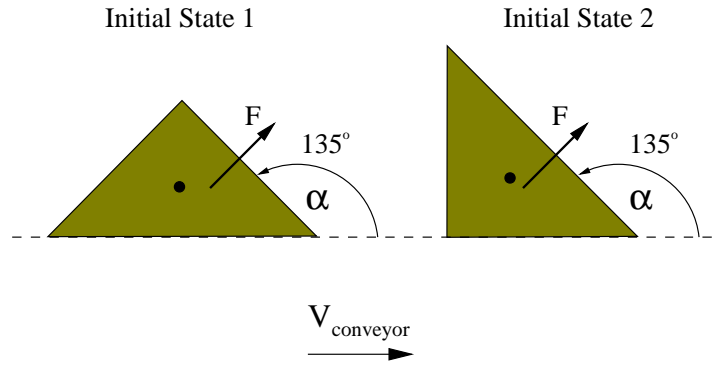


**Figure 5-11** Contact configuration similarities between Initial States 1 and 2 for TriPoly1.

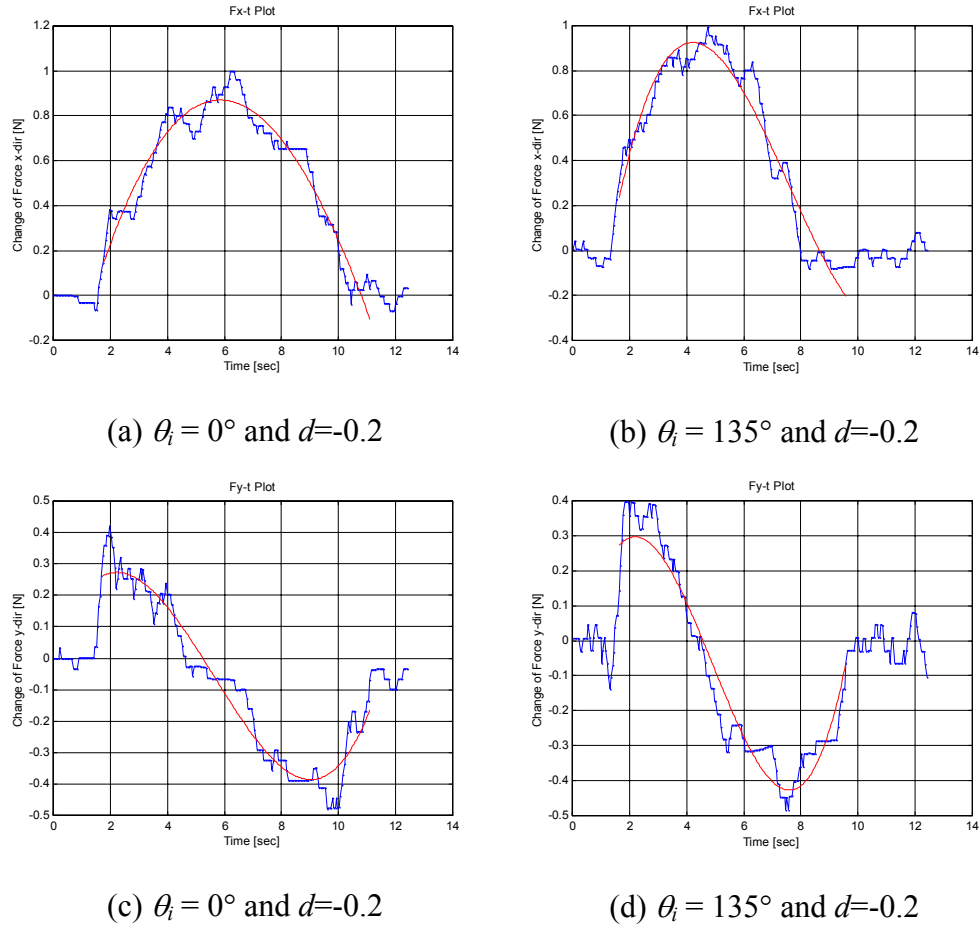


**Figure 5-12** Similar  $F_x$  and  $F_y$  profiles for  $\theta_i = 0^\circ$  and  $\theta_i = 135^\circ$ .

In addition, an alternative approach to the orienting plan for polygonal parts with certain symmetries as TriPoly1 is to pass the polygonal part through a selected sequence of static passive pins knowing that the final orientation will be either Orientation 1 ( $\theta_f \approx 20^\circ$ ) or Orientation 2 ( $\theta_f \approx 160^\circ$ ). Then add the static active (i.e. sensorized) pin following the last static passive pin in the sequence so as to record the F/T profile of either final orientation and distinguish it. This alternative however, also fails to yield a clear result due to the part's geometry. Figure 5-13 illustrates the two averaged final orientations possible for TriPoly1, where the angles  $\alpha$  of contact edges clearly show similarities between the two orientations. And again, for a given  $d$  the motion to follow is equivalent for both orientations. Hence, the F/T profiles are alike, and the orientations cannot be distinguished as it was for initial states 1 and 2.

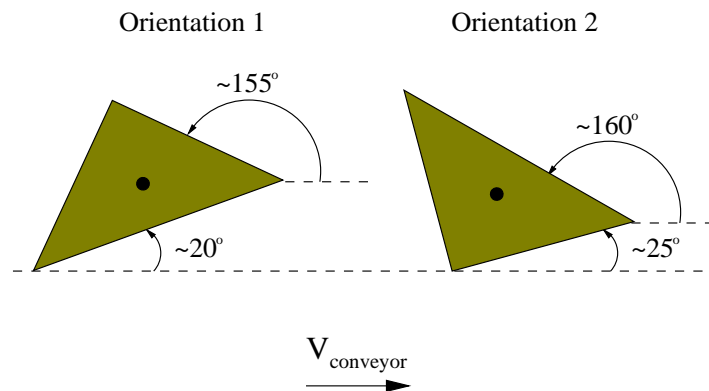


**Figure 5-13** Contact configuration similarities between final orientation sets 1 and 2 for TriPoly1.

## 5.6 – Planning with F/T Sensor

In Chapter 4, the existence of pin sequences for TriPoly1 was investigated. The planner yielded various solutions for any two initial states ending in one common final orientation, or solutions for all three initial states ending in two common final orientations, but no solution was found to yield one single orientation set starting with all three initial states. This is due to the symmetry of the polygon's geometry. Therefore, to

distinguish the final orientations of TriPoly1 by knowing which initial state is present the results from the F/T sensor are incorporated into the planning stage.

Comparing the force profiles for TriPoly1 using the sign matrix  $[S]$  demonstrated that initial states 1 and 2 can be distinguished from 3, but not 1 from 2, as it was outlined in Table 5-2, where the experimental profiles for each initial state were compared against all the simulation profiles, and the higher scores selected. Using this information along with the planner results yielding two final orientations, a pin sequence is selected as outlined in Table 5-3 and previously illustrated in Figure 4-16 such that initial states 1 and 2 yield Orientation 1 while initial state 3 yields Orientation 2. Now it is possible to determine which of the two possible final orientations will result for any initial state of the given polygon, TriPoly1.

**Table 5-3 Pin sequence for TriPoly1 yielding Final Orientations 1 and 2.**

Initial States	Final Orientation	Pin 1	Pin 2	Pin 3
0° and 135°	Orientation 1	1	10	5
225°	Orientation 2	1	10	5

Hence, in combination with the known planner results and the F/T sensor set up on the first pin of the sequence as depicted in Figure 5-1, the objective to distinguish between the initial states of the polygon, which in turn indicates which of the possible final orientations will result, contributes to the orienting process, and further contributes to the development of a hybrid part orienter.

## 5.7 – Vertex/Edge Contact Detection

Having successfully revealed a sequence of pins to orient the asymmetric TriPoly2 in Chapter 4 and then introduced the F/T sensor in the previous section to complement the

final solution for the symmetric TriPoly1 by distinguishing between the two final orientations, it is of interest to further explore the use of the F/T sensor to contribute to the planning process of a hybrid part orienter. For this purpose, the focus is placed on whether it is possible to make a distinction between vertex and edge contact using the F/T sensor. This section presents the motivation, hypothesis and results of the vertex/edge contact detection empirical exercise.

The motivation for this exploration lies in the preceding chapter. Previously, in the experimental verification of the pin sequence for TriPoly2 outlined in Table 4-1, one case failed to yield the final expected orientation. The cause of this failure was due to a vertex of the polygon “catching” the pin and rotating in the opposite direction than expected. Therefore, it is of interest to investigate the possible detection of such cases that can lead to the unsuccessful orientation of a given polygon. This empirical exercise is also a contribution towards the overall design of a hybrid mechanics-based part feeder.

It is hypothesized that the F/T profiles obtained from a vertex contact will yield noticeably distinct plots from those obtained from edge contacts. Edge contacts showed a “smooth” transition within their profiles, that is, a steady increase/decrease of force and torque throughout contact was noted over time. Vertex contacts on the other hand, are expected to show a discontinuity at the beginning of the profiles, more precisely, show a “spike” within their plots due to expected longer contact between the part's vertex and the pin as a result of friction. This occurs when the vertex “catches” the pin and “hovers” until the part slips onto an edge.

The random nature of vertex slip and resulting rotation is dependent on the part's contact configuration, the pressure distribution, and the contact friction. However, in a simplified model such as the one in this thesis, where a constant and uniform pressure distribution is assumed, Mason's rotation sense may be enough to approximate the slip/rotation of the part. Nonetheless, for the purpose of this exercise, the interest lies in whether a distinction between contact types can be made using the F/T sensor. Thus, an



empirical exercise is deemed sufficient to provide the basic information needed to answer the question posed.

### **5.7.1 – Experiment**

Using the same experimental setup as illustrated in Figure 5-6, numerous trials were carried out for distinct contact configurations of TriPoly2 such that the part contacted the pin either on a vertex or an edge. Overall, 30 vertex trials and 30 edge trials were performed.

Throughout the vertex trials the following observations were noted: vertex contacts the pin, sticks while the part slides over the conveyor, thus continuously “pushing” on the pin in the direction of motion (positive  $x$ -direction); then, the vertex eventually begins to rotate and/or slip onto an edge at which point the part behaves as if an edge contact had occurred, continue to slip and rotate against the pin about the respective instantaneous CORs until losing contact.

The contact configurations tested, particularly the orientations selected were based on the expected orientations at which the part is most likely to contact the pin. The selected orientations are the three initial states of TriPoly2 (i.e.,  $0^\circ$ ,  $90^\circ$ , and  $204^\circ$ ) as well as three averaged possible final orientations (i.e.,  $10^\circ$ ,  $130^\circ$ , and  $240^\circ$ ). For each one of these six orientations selected, 5 trials were completed, and the data compiled. Sample profiles of one vertex contact trial are shown in Figure 5-14.

### **5.7.2– Detection Method**

By observing the F/T profiles obtained for the vertex contact cases, the presence of the expected “spikes” is noticed. Also, with the presence of the spikes it is noted that the curves depict a series of maximum/minimum points not present in the curves of the edge contact profiles. In essence, the spikes add a maximum point followed by a quick drop to a minimum point, before the curve begins to slope up again and follow the rest of the profile outlining the interaction between the part and the pin.

To make distinctions between vertex and edge contact a method of evaluation must be set. For that purpose, polynomials are curve-fitted again to the F/T profiles using the least-squares method (dotted lines in Figure 5-14(a,c)), but this time polynomials of degree 6 are chosen by trial and error to allow greater flexibility in outlining the numerous slope changes.

Then, to identify the changes in slope in the curves and the corresponding maximum/minimum points the first derivative of each fitted polynomial is calculated (see Figure 5-14(b,d)). Here, the points of interest are the zero crossings, or the changes in slope from positive to negative or vice-versa indicating the presence of a maximum or a minimum point respectively.

It is noted that the edge contact profiles depict only one maximum point, or a maximum→minimum combination, but no more. However, the vertex contact profiles show that at least a maximum→minimum→maximum series of extreme points must be present if a spike is included in the profile. Therefore, an edge contact will show a maximum of two zero crossings in the first derivative plots, while a vertex contact will show a minimum of three. This difference in zero crossings or sign change in the direction of slope is the criteria used to evaluate if a vertex contact or an edge contact has occurred. And so the criteria for a vertex contact is as follows:

$$zero\_cross\_count > 3 \quad (5-3)$$

Where *zero\_cross\_count* is the number of zero crossings in the first derivative plot.

Thus, if *zero\_cross\_count* indicates three or more zero crossings then the profile shows a series of at least three maximum/minimum points, and hence it indicates a vertex contact.

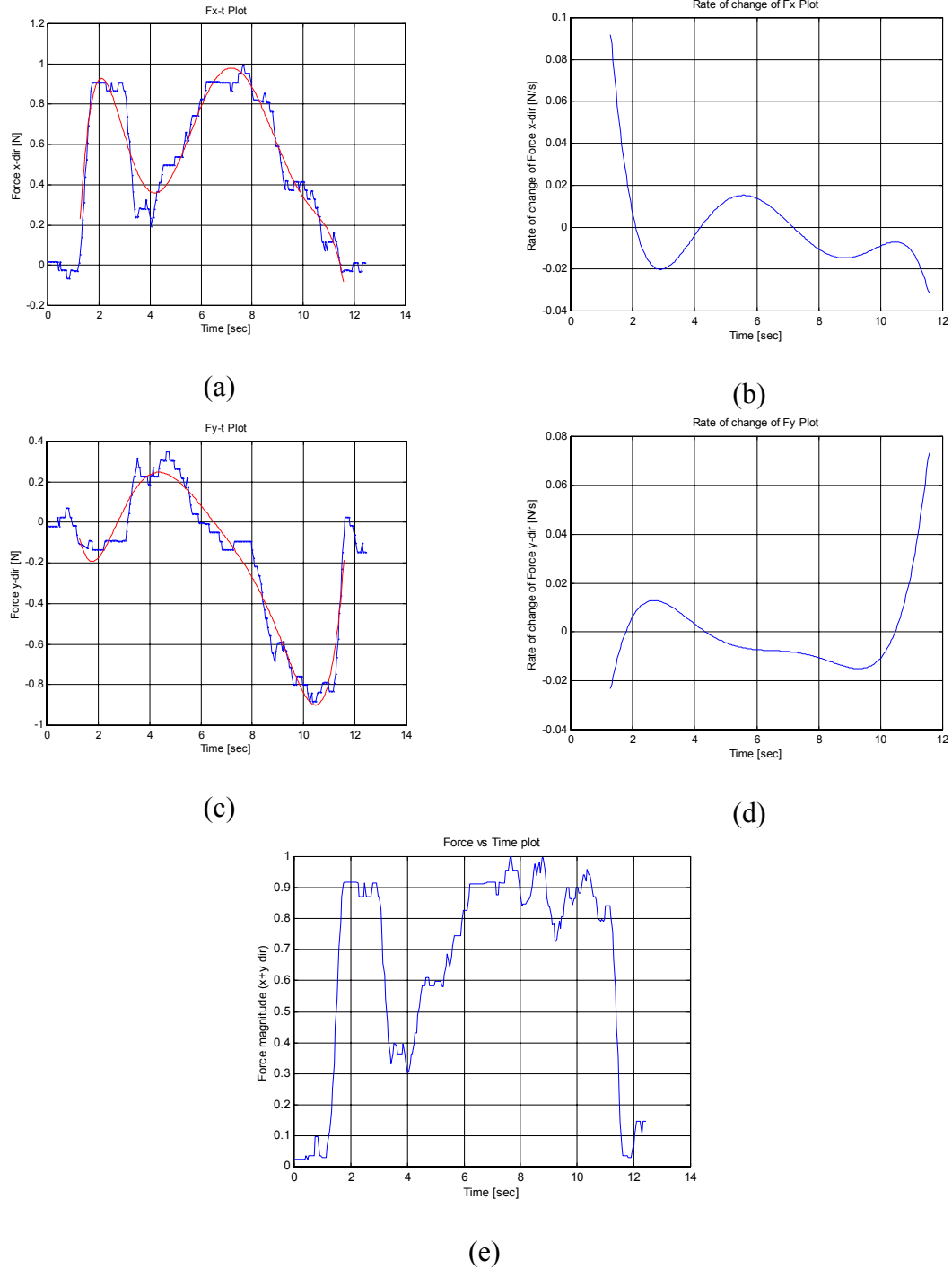


**Figure 5-14** Vertex contact plots for TriPoly2 ( $\theta_i = 0^\circ$ ). (a) shows the spike in the x-dir force and (b) shows its rate of change with three zero crossings. (c) shows the y-dir force with no noticeable difference from the edge contact profiles, (d) shows the y-dir force rate of change. Lastly, (e) illustrates the normalized magnitude of the applied force, where the spike is also highly noticeable.

### 5.7.3– Results

The overall tabulated results for the 30 trials of vertex contact and the 30 trials of edge contact are outlined in Table 5-4, where the detection ratio indicates the number of successful identifications for the expected contact type. Hence, a success ratio of 73% for the vertex contact and 93% for the edge contact attest that a distinction between vertex and edge contact is indeed possible using the F/T sensor.

Therefore, the results in this section confirm the previously stated hypothesis and demonstrate that the inclusion of this exploration in the hybrid part feeder system can assist in identifying parts that may fail to orient for a given pin sequence. In the future, such parts can be redirected by the use of dynamic (moving) pins when applying an online planner.

**Table 5-4 Vertex/edge contact detection results**

Contact Type	Detection Ratio
Vertex Contact	22/30
Edge Contact	28/30

## 5.8 – Discussion and Conclusions

This chapter has demonstrated that the use of an F/T sensor in combination with the overhead pins possesses many benefits. First, the orienting process of parts with certain symmetries such as TriPoly1 is complemented by an empirical comparison exercise where the initial state of the polygon is identified, and hence together with a selected pin sequence identifies the final orientation set. Then, the sensor is used in an exploration to distinguish between vertex and edge contact with the pin thus identifying parts that may fail to orient according to the selected pin sequence due to unpredicted contact

configurations. These findings all contribute to the planning process to orient planar polygonal parts, and are hence, a contribution of this thesis towards the design of a hybrid mechanics-based part feeder.

Moreover, it is the author's interest to point out that using the F/T sensor with 6-axis and only utilizing the force components along the  $x$ - and  $y$ -axis is redundant and expensive. To reduce the cost of utilizing such sensor, it is recommended that a simpler sensing setup is customized by mounting strain gauges along the axis of interest on the overhead pin. Collecting the data from the strain gauges would require an amplifier for the signal which can also be designed and assembled in-house at a low cost. Furthermore, the signals obtained from the strain gauges would be noisy but rich in information pertaining to the contact dynamics. Thus, applying tools for signal processing rich signatures can be extracted and utilized in the planning process.

# Chapter 6

## Conclusions and Future Work

### 6.1 – Conclusions

Motivated by the principle of minimalism, this thesis introduced aspects of an innovative method towards the development of a mechanics-based hybrid part feeder. The applicability and use of *overhead pins* of various classes were investigated and tested, with particular emphasis on static pins, passive and active, that is, stationary pins without and with sensors. This exploratory study showed that overhead pins are indeed capable of orienting planar polygonal parts from a number of initial states to a final orientation set. Limitations however do exist, and it must be noted that using pins increases the complexity of the problem in comparison to using fences. Nonetheless, this being an exploratory study it is too early to rule out the efficiency advantages that pins present by shortening the length of assembly lines. It is possible that using multiple pins instead of single pins will improve the outcome and so they should be explored.

Contributions to the part orienting research community presented in this thesis include the re-examination of the motion of sliding polygonal parts on a flat surface based on minimum power mechanics along with the assumption of a constant and even pressure distribution; and although the exact motion of the part is unknown, a competent approximation is made. As a contribution, a model stemming from and expanding on the results from Peshkin and Sanderson in [17] detailed the motion of the planar polygonal part traveling on a slow moving conveyor and contacting a stationary point obstacle more accurately (see Chapter 2). This model was used to study and understand the behaviour of the part imperative for the successful development of a planner to orient the given part.

Following the investigation of the part's motion against an overhead pin, configuration maps encapsulating the physics of such motion for distinct contact configurations were created in Chapter 3. Here the creation and use of configuration maps representing the interaction of a part and a point obstacle such as a pin for the purpose of part orienting is a first within the research community.

These configuration maps were then utilized in the development and implementation of a planner in Chapter 4 to search for a sequence of pins to orient a given planar polygonal part. This planner, however, due to its brute nature required an extensive breadth expansion because of the limitations presented by the contact parameter  $d$ , and the need to approximate the part's COM at all times. Nonetheless, the planner provided a solution to the problem of part orienting using overhead pins, an innovative method in part orienting.

Lastly, the novel inclusion of a force/torque sensor to the orienting problem using overhead pins to supplement the planner results was investigated in Chapter 5. The outcome proved to be beneficial, and hence a solution was found for cases where a single solution was not found passively (without sensors). Using the F/T profiles constructed from sensor data representing the interaction between the part and the pin a distinction was made between the initial states of the given part via an empirical comparison method. In turn, these empirical results in combination with the planner results pointed towards the resultant final orientation of the given polygon. Hence, helping to identify the final orientation in cases where a single final orientation was not found. In addition, using the same F/T sensor another empirical exercise was carried out, and a distinction between vertex and edge contact with the pin was made. This study sprung from a single case failure to orient TriPoly2 during experimental trials in Section 4.3.3. Subsequently, it is hypothesized that making a distinction between these two contact types can help identify cases where a part may fail to reach its final orientation because of unplanned

motion as the pin “catches” the part’s vertex forcing it to rotate unexpectedly. The addition of this contact distinction to enrich the planner is left as future work.

## **6.2 – Future Work**

A more efficient planner need to be explored. The present planner proved to be timely and memory expensive due to the fact that individual trees must be expanded for each initial state of the given polygon. To start, implement more criteria and further investigate the use of sensing to shorten the breadth of the planning search; thereby, eliminating the “brute” aspect of the current search method. For example, if by using the F/T sensor in the first pin the initial states can be distinguished, then the application of an online planner can find a shorter sequence of pins to take the part to a desired final orientation rather than the longer pin sequence attained without the use of a sensor.

Moreover, it is recommended that the study be expanded to include different general polygons, convex and concave, in order to improve the understanding of polygonal part behaviour moving against a point obstacle. This in turn should provide a better ground for the development of a more comprehensive planner.

Then, to complete the study of the various classes of pins described in the introduction in Chapter 1, the applicability and use of dynamic pins must be investigated. These dynamic or moving pins, as first illustrated in Chapter 1 and shown here again for convenience in Figure 6-1, are intended to possess the ability to move perpendicularly to the direction of the conveyor belt motion. Here, the use of static and moving pins with and without sensors constitutes the creation of a multi-agent system where these pins of various classes are the agents that collaborate towards the same goal, part orienting. In essence, this multi-agent system is the more complete mechanics-based hybrid part feeder towards which the studies in this thesis are a contribution for future development.

Preliminary work on modeling the interaction of a polygonal part and a dynamic pin is appended in Appendix E. Applicability of dynamic pins may be found in cases



where multiple sets of final orientations exist as it was the case for TriPoly1 through passive pins, where two final orientations were identified. Here, dynamic pins can be implemented to further orient the part. Initial simulations have shown that the final orientation 1 of TriPoly1 in Figure 4-16 can be reoriented to final orientation 2; and thus, orienting the part to a single final orientation set.

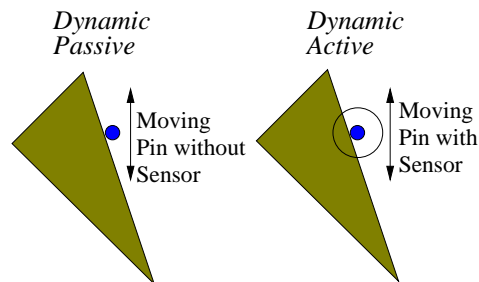


**Figure 6-1 Dynamic pins, as first illustrated in Chapter 1, capable of moving perpendicularly to the direction of conveyor belt motion.**

Another point of interest for further work is the duration of the period of contact between the part and the pin and whether this timing information can assist in orienting a given polygon and in the development of a more efficient planner for the same purpose. This notion is illustrated in Figure 6-2 where a polygonal part is shown at the first instance of contact with the pin ( $t = t_i$ ) and at the end of the contact period ( $t = t_f$ ). It must be noted, that the time length of this period may vary even for the same contact configuration prior to pin contact due to the uncertainty resulting from the actual contact friction. However, it is recommended that this be further investigated. Thus, assuming a known and constant rate of displacement of the conveyor belt, Appendix F tabulates some basic simulation results for various contact configurations. In these results it can be seen that for a given polygon and a known contact parameter, distinct times result for each different initial state. And so, interest lies in whether the timing information can be used to differentiate the initial states more reliably than the F/T sensor profile comparison. If the result is positive, then not only the distinction of initial states may be

more clear and accurate, but also, the sensing mode may be simplified to a contact sensor (i.e. strain gauge) further building on the principle of minimalism.

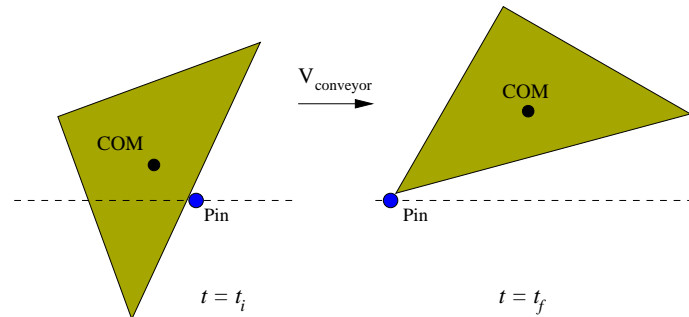


**Figure 6-2 Polygonal part at initial contact ( $t = t_i$ ) and at the end of the contact period ( $t = t_f$ ). The difference in time ( $t_f - t_i$ ) indicates the time length of contact duration.**

The last point of future work to be indicated in this thesis is the diversification of this work from a quasi-static environment to a dynamic environment. In particular, taking from the notion of the array of retractable pins referred to as the “Pachinko Machine” presented in [5], it is of interest to create a setup in which pins are mounted on a slanted board at a desired angle. However, instead of “capturing” the parts as in [5], the intention is to attempt to orient the part as it falls through a sequence or array of static pins. The intention is to create layers of passive and active pins to collect information on the part’s motion to be used throughout the overall system to orient the part. Figure 6-3 depicts the proposed dynamic environment setup. The first layer of agents or pins, consists of static pins that may be equipped with sensors and based on the information gathered here, then a second layer of pins (active pins) that would orient the part to a single orientation can be applied. The second layer may also be composed of a dynamic fence instead to redirect the part in order for it to reach its final orientation. Appendix G presents a prelude on this subject. Here, the motivation, objective, setup, and preliminary results are presented along with the encountered complications.

Results in Appendix G lead to the conclusion that further development is needed on the mechanics-based model for the design of the HGPO, particularly the inclusion of an impact/impulse model such as the ones presented in [6] by Brach, [24] by Stewart, and [25] by Wang and Mason. It is also recommended that sensors with greater sensitivity than foil strain gauges such as semiconductor strain gauges be used in the experimental phase. Lastly, it is advised that planning strategies be investigated for the HGPO and that the dynamic layer be designed.



**Figure 6-3** Notion of proposed dynamic environment setup. The first layer consists of passive pins with sensors while the second layer may consist of a layer of active pins (moving and/or retractable) or an active fence to orient the part after data is gathered in the first layer.

## Appendix A

### Nelder-Mead Simplex Algorithm

The Nelder-Mead (NM) simplex algorithm is a popular direct search method for multidimensional unconstrained minimization, where direct search methods are those that neither compute nor approximate any derivatives of the objective function. The NM algorithm has been presented as a method for finding the minimum value of a real-valued function  $f(x)$  for  $x \in \mathbb{R}^n$  [12], and since the NM algorithm attempts to minimize this real scalar-valued nonlinear function using only function values, without any derivative information, it falls into the direct search method class [12].

The search is based on maintaining at each step a *simplex*, described as a geometric figure in  $n$  dimensions of nonzero volume that is the convex hull of  $n+1$  vertices [12]. Figure A-1 illustrates the simplex in two-dimensional space, where for  $n = 2$ , the resultant geometrical figure is a triangular polygon.

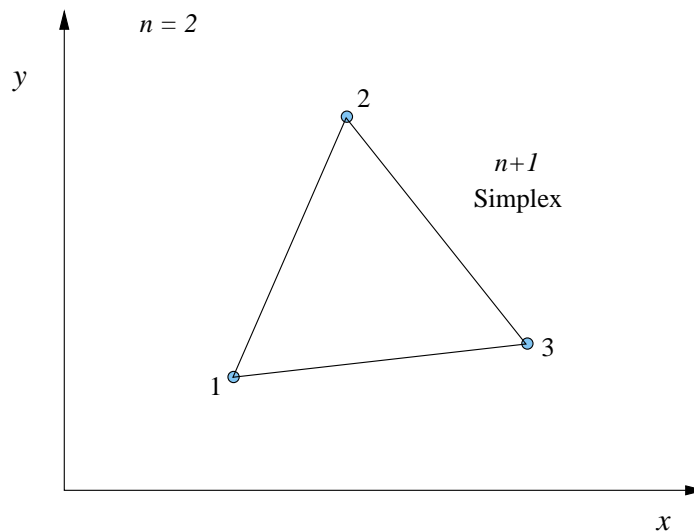


Figure A-1 Two-dimensional simplex.

To execute the search of a given function, four scalar parameters must be specified to define a complete Nelder-Mead method: coefficients of *reflection* ( $\rho$ ), *expansion* ( $\chi$ ), *contraction* ( $\gamma$ ), and *shrinkage* ( $\sigma$ ). These parameters must satisfy:

$$\rho > 0, \chi > 1, \chi > \rho, 0 < \gamma < 1, \text{ and } 0 < \sigma < 1 \quad (\text{A-1})$$

The commonly used values in the *standard* Nelder-Mead algorithm are:

$$\rho = 1, \chi = 2, \gamma = \frac{1}{2}, \text{ and } \sigma = \frac{1}{2}. \quad (\text{A-2})$$

Each  $k$ th iteration,  $k \geq 0$ , begins with a simplex  $\Delta_k$ , specified by its  $n+1$  vertices, each of which is a point in  $\mathfrak{R}^n$ . It is always assumed that iteration  $k$  begins by ordering and labeling these vertices as  $x_1^{(k)}, \dots, x_{n+1}^{(k)}$ , such that  $f_1^{(k)} \leq f_2^{(k)} \leq \dots \leq f_{n+1}^{(k)}$  where  $f_i^{(k)}$  denotes  $f(x_i^{(k)})$ , the value of each  $i$ th vertex point in the function  $f(x)$  of interest for iteration  $k$ . The iteration proceeds by predicting a point at which the function has a more desirable value, and then including this point in the simplex [8]. So, the  $k$ th iteration generates a set of  $n+1$  vertices that define a different simplex for the next iteration, so that  $\Delta_{k+1} \neq \Delta_k$ .

A single generic iteration of the Nelder-Mead Algorithm follows the steps 1 through 5 outlined below as taken directly from Lagarias et al. [12].

1. Order.

Order the  $n+1$  vertices to satisfy  $f(x_1) \leq f(x_2) \leq \dots \leq f(x_{n+1})$ , using the given tie-breaking rules (refer to [12]).

2. Reflect.

Compute the *reflection point*  $x_r$  from

$$x_r = \bar{x} + \rho(\bar{x} - x_{n+1}) = (1 + \rho)\bar{x} - \rho x_{n+1} \quad (\text{A-3})$$

where  $\bar{x} = \sum_{i=1}^n x_i / n$  is the centroid of the  $n$  best points (all vertices except for  $x_{n+1}$ ). Evaluate  $f_r = f(x_r)$ . If  $f_1 \leq f_r < f_n$ , accept the reflected point  $x_r$  and terminate the iteration.

### 3. Expand.

If  $f_r < f_1$ , calculate the *expansion point*  $x_e$ :

$$x_e = \bar{x} + \chi(x_r - \bar{x}) = \bar{x} + \rho\chi(\bar{x} - x_{n+1}) = (1 + \rho\chi)\bar{x} - \rho\chi x_{n+1} \quad (\text{A-4})$$

and evaluate  $f_e = f(x_e)$ . If  $f_e < f_r$ , accept  $x_e$  and terminate the iteration; otherwise (if  $f_e \geq f_r$ ), accept  $x_r$  and terminate the iteration.

### 4. Contract.

If  $f_r \geq f_n$ , perform a *contraction* between  $\bar{x}$  and the better of  $x_{n+1}$  and  $x_r$ .

- a. Outside. If  $f_n \leq f_r < f_{n+1}$  (i.e.,  $x_r$  is strictly better than  $x_{n+1}$ ), perform an *outside contraction*: calculate

$$x_c = \bar{x} + \gamma(x_r - \bar{x}) = \bar{x} + \gamma\rho(\bar{x} - x_{n+1}) = (1 + \gamma\rho)\bar{x} - \gamma\rho x_{n+1} \quad (\text{A-5})$$

and evaluate  $f_c = f(x_c)$ . If  $f_c \leq f_r$ , accept  $x_c$  and terminate the iteration; otherwise, got to step 5 (perform a shrink).

- b. Inside. If  $f_r \geq f_{n+1}$ , perform an *inside contraction*: calculate

$$x_{cc} = \bar{x} - \gamma(\bar{x} - x_{n+1}) = (1 - \gamma)\bar{x} + \gamma x_{n+1} \quad (\text{A-6})$$

and evaluate  $f_{cc} = f(x_{cc})$ . If  $f_{cc} < f_{n+1}$ , accept  $x_{cc}$  and terminate the iteration; otherwise, go to step 5 (perform a shrink).

5. Perform a shrink step.

Evaluate  $f$  at the  $n$  points  $v_i = x_1 + \sigma(x_i - x_1)$ ,  $i = 2, \dots, n+1$ . The (unordered) vertices of the simplex at the next iteration consist of  $x_1, v_2, \dots, v_{n+1}$ .

The result of each iteration is either: 1) a single new vertex replacing  $x_{n+1}$  in the set of vertices for the next iteration; or 2) if a shrink is performed, a set of  $n$  new points that, together with  $x_1$ , form the simplex at the next iteration [12].

The process is terminated when the limiting function values at the vertices of the simplex are the same:  $f_1^* = f_2^* = f_3^*$  or they “collapse” to zero volume, i.e., to either a point or a line segment [12]. For a complete description of the Nelder-Mead simplex algorithm convergence, please refer to the journal paper by Lagarias et al. [12].

Lastly, the Matlab optimization toolbox used throughout the study in this thesis includes the minimizing function **fminsearch**, which uses a Nelder-Mead type simplex search method. The Matlab help window describes **fminsearch** as a function that attempts to return a vector  $X$  being a *local minimizer* of  $F(X)$  near the starting vector  $X_0$ . The return of a local minimizer indicates that the Nelder-Mead algorithm is a local optimizer method.  $F(X)$  should be a real scalar valued function of a vector variable as is the energy equation  $E_r$  (Equation (2-13)). Finally, in accordance to expression (A-2) the minimizing function **fminsearch** in Matlab does indeed use these common values within the function algorithm.

## Appendix B

### Finite Element Methods for Integration

For general geometrical objects no analytical formulation exists to carry out double integrations over their areas. Thus, for general geometric objects, the double integration can only be solved by numerical methods. One possible solution is to partition the object into a number of simple areas such as triangles and then summing up the partial results [15]. Another approach is to convert these general geometrical objects into simpler geometries such as rectangles.

Applicable to the work in this thesis where arbitrary triangular polygons are the objects of study, a series of transformations to convert any triangular area to a more standard triangular area followed by another transformation to a rectangular area are presented in order to make the calculation of double integrals possible, particularly for the quasi-static motion modeling using minimum power mechanics in Section 2.16. In general, much of the mathematical detail for two-dimensional cases is concerned with the evaluation of integrals along curves lying in the  $xy$ -plane (line integrals) and over areas in the  $xy$ -plane (double integrals). Regardless of their intricacies, these integrals can be handled by converting the geometrical figures into standard simpler geometries by the use of finite elements and shape functions. Once they are in standard form the integrals can be evaluated by the method of Gaussian quadrature [13]. Where Gaussian quadrature is a numerical integration method that does not require that a function  $f(x)$  be evaluated at its endpoints. Instead, Gaussian Integration is based on the use of an optimally chosen polynomial to approximate the integrand  $f(x)$  over the interval  $[-1, +1]$ . The detail of Gaussian quadrature is beyond the scope of this work, and it won't be presented here.



For example, the double integral of a function  $f(x, y)$  taken over a two-dimensional area  $A$  on the  $xy$ -plane as illustrated in Figure B-1, is normally evaluated as a repeated integral as follows:

$$\iint_A f(x, y) dy dx = \int_a^b \left( \int_{y=h_1(x)}^{y=h_2(x)} f(x, y) dy \right) dx \quad (\text{B-1})$$

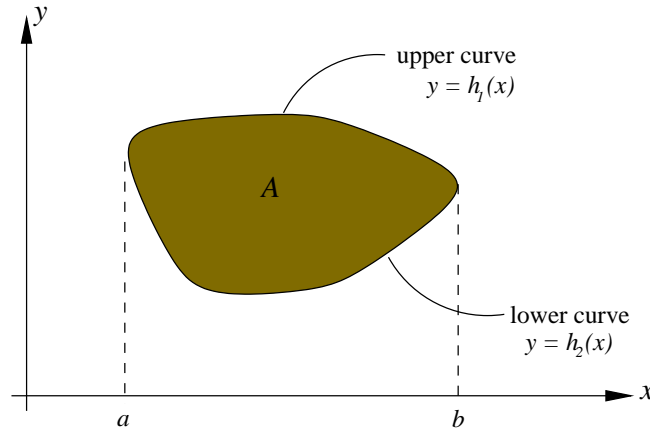


**Figure B-1** Arbitrary area in  $xy$ -plane showing limits of integration.

If the area of interest  $A$  is rectangular, then simple changes of variable can be effected to transform the rectangular area into a standard square with respect to two new variables  $(\xi, \eta)$  [13]. However, if the area is not rectangular then it can be transformed into another standard region such as a standard triangle with vertices  $(-1, -1)$ ,  $(-1, 1)$  and  $(1, -1)$ . Such transformations are performed by a change of variables of the form:

$$\begin{aligned} x &= x(\xi, \eta) \\ y &= y(\xi, \eta) \end{aligned} \quad (\text{B-2})$$

Consider a three-noded triangular element with vertices  $(x_i, y_i)$ ,  $i=1, 2, 3$  as depicted in figure B-2. Then, the transformation:

$$\begin{aligned}
 x &= x_1 \left( -\frac{1}{2}(\xi + \eta) \right) + x_2 \left( \frac{1}{2}(1 + \xi) \right) + x_3 \left( \frac{1}{2}(1 + \eta) \right) \\
 y &= y_1 \left( -\frac{1}{2}(\xi + \eta) \right) + y_2 \left( \frac{1}{2}(1 + \xi) \right) + y_3 \left( \frac{1}{2}(1 + \eta) \right)
 \end{aligned}
 \tag{B-3}$$

maps a triangle with vertices  $(x_i, y_i)$  into the standard triangle in the  $\xi\eta$  plane also illustrated in Figure B-2. The relation between  $(x, y)$  and  $(\xi, \eta)$  is linear so that straight lines in the  $\xi\eta$  plane will remain straight lines in the  $xy$  plane [13].

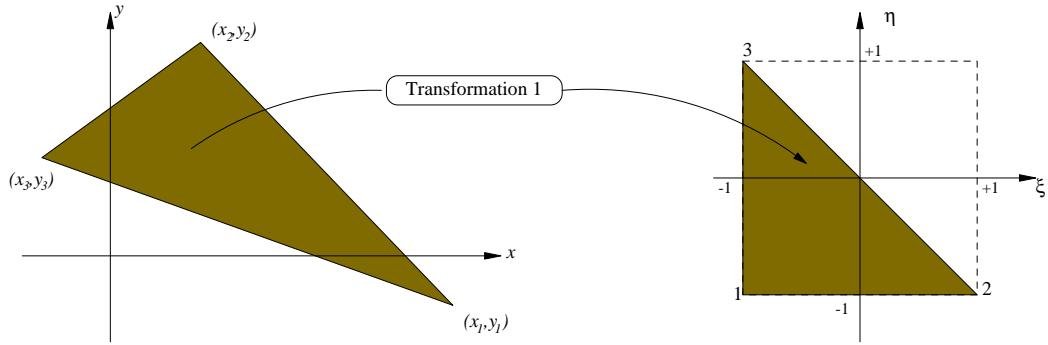


**Figure B-2 Transformation from arbitrary triangle to standard triangle.**

The functions used in the transformation are called linear shape functions for a three-noded triangle [13], and they are as follows:

$$\begin{aligned}
 T_1(\xi, \eta) &= -\frac{1}{2}(\xi + \eta) \\
 T_2(\xi, \eta) &= \frac{1}{2}(1 + \xi) \\
 T_3(\xi, \eta) &= \frac{1}{2}(1 + \eta)
 \end{aligned}
 \tag{B-4}$$

Using these linear shape functions, the transformation in (B-4) can be re-written as:

$$\begin{aligned}
 x &= \sum_{i=1}^3 x_i T_i(\xi, \eta) \\
 y &= \sum_{i=1}^3 y_i T_i(\xi, \eta)
 \end{aligned}
 \tag{B-5}$$

where  $(x_i, y_i)$ ,  $i=1,2,3$ , are the vertices in the general triangle.

Overall, transformations are carried out using a suitable change of variables of the form:  $x = x(\xi, \eta)$  and  $y = y(\xi, \eta)$ . And therefore, with respect to these 'standard' variables,  $\xi$  and  $\eta$ , the double integral can be written as:

$$\iint_A f(x, y) dx dy = \int_{-1}^1 \int_{-1}^{-\xi} g(\xi, \eta) d\eta d\xi \quad (B-6)$$

Where

$$g(\xi, \eta) = f(x(\xi, \eta), y(\xi, \eta)) |J_1| \quad (B-7)$$

are the integrand  $f(x, y)$  re-expressed as  $f(x(\xi, \eta), y(\xi, \eta))$  in terms of the new variables  $\xi$  and  $\eta$ , and the increments  $dx dy$  replaced by the quantity  $J_1$  called the Jacobian of the transformation and  $d\eta d\xi$ . The Jacobian is defined as follows:

$$J_1 = \begin{bmatrix} \frac{\partial x}{\partial \xi} & \frac{\partial y}{\partial \xi} \\ \frac{\partial x}{\partial \eta} & \frac{\partial y}{\partial \eta} \end{bmatrix} = \begin{bmatrix} -\frac{1}{2}x_1 + \frac{1}{2}x_2 & -\frac{1}{2}y_1 + \frac{1}{2}y_2 \\ -\frac{1}{2}x_1 + \frac{1}{2}x_3 & -\frac{1}{2}y_1 + \frac{1}{2}y_3 \end{bmatrix} \quad (B-8)$$

After transforming the general triangular area into a standard triangular area, it is now of interest to transform this standard triangular area to a standard rectangular area as shown in Figure B-3 to further simplify the integration. For this purpose utilize the following linear transformation [15]:

$$\eta = (1 - \xi)\lambda - 1 \quad (B-9)$$

Here, when  $\lambda = 1$ ,  $\eta = -\xi$  and when  $\lambda = 0$ ,  $\eta = -1$ .

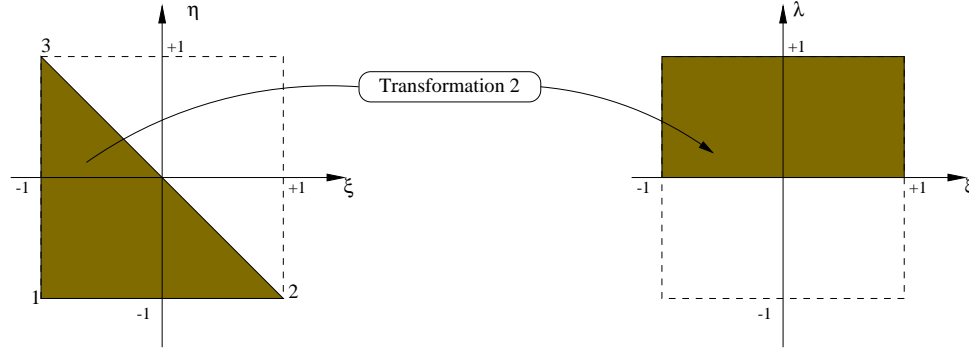


**Figure B-3 Transformation from regularized triangle to regularized rectangle.**

Differentiating this linear transformation, we obtain the following expression to be used in the Jacobian:

$$d\eta = (1 - \xi)d\lambda \quad (\text{B-10})$$

The resulting double integral after this second transformation can be written as:

$$\iint_A f(x, y) dx dy = \int_{-1}^1 \int_{-1}^{-\xi} g(\xi, \eta) d\eta d\xi = \int_0^1 \int_{-1}^1 h(\xi, \lambda) d\xi d\lambda \quad (\text{B-11})$$

Where  $h(\xi, \lambda) = g(\xi(\xi, \lambda), \eta(\xi, \lambda))|J_2|$ , and as before the quantity  $J_2$  is the Jacobian defined here as follows:

$$J_2 = \begin{bmatrix} \frac{\partial \xi}{\partial \xi} & \frac{\partial \eta}{\partial \xi} \\ \frac{\partial \xi}{\partial \lambda} & \frac{\partial \eta}{\partial \lambda} \end{bmatrix} = \begin{bmatrix} 1 & -\lambda \\ 0 & (1 - \xi) \end{bmatrix} \quad (\text{B-12})$$

Consequently, the desired integrals are now in standard rectangular form with constant boundaries and they can be integrated using existing double integral routines such as the Gaussian quadrature [15].

The following three pages (pp.113-115) compose a sample calculation executed in **Maple** outlining the transformation process presented in this Appendix.

Addendum to Appendix B - Finite Element Methods for Integration, FEM sample calculations.  
By: Herbert F. Noriega

Using TriPoly2 at an orientation of 30degrees, carry out the calculation of the integral component in equation 2-13 in Chapter 2.

The resultant is referred to as "dr" by Peshkin and Sanderson [17], and is seen as representing a weighted distance between the COM and the COR.

```
> restart;
> with(linalg):
Warning, new definition for norm
Warning, new definition for trace
Function f(x,y) with respect to the x- and y-components of a point w anywhere on the part (refer to Chapter 2).
```

```
> funcXY := sqrt( (wX-COR[1])^2 + (wY-COR[2])^2 );
```

$$funcXY := \sqrt{wX^2 - 2 wX COR_1 + COR_1^2 + wY^2 - 2 wY COR_2 + COR_2^2}$$

Following are the transformation equations obtained from (B-4).

```
> wX :=
v1[1]*(-0.5*(xi+eta))+v2[1]*(0.5*(1+xi))+v3[1]*(0.5*(1+eta));
wX:=v11(-0.5ξ-.5η)+v21(.5+.5ξ)+v31(.5+.5η)
```

```
> wY :=
v1[2]*(-0.5*(xi+eta))+v2[2]*(0.5*(1+xi))+v3[2]*(0.5*(1+eta));
wY:=v12(-0.5ξ-.5η)+v22(.5+.5ξ)+v32(.5+.5η)
```

Now, the Jacobian expression (B-9), followed by its determinant.

```
> J1 := matrix(2,2,[ diff(wX,xi), diff(wY,xi), diff(wX,eta),
diff(wY,eta) ]);
```

$$J1 := \begin{bmatrix} -.5 v1_1 + .5 v2_1 & -.5 v1_2 + .5 v2_2 \\ -.5 v1_1 + .5 v3_1 & -.5 v1_2 + .5 v2_2 \end{bmatrix}$$

```
> detJ1 := det(J1);
```

$$detJ1 := -.25 v2_1 v1_2 + .25 v2_1 v2_2 + .25 v1_2 v3_1 - .25 v2_2 v3_1$$

The following equation is the equation g(xi,eta), that is, f(x,y) multiplied by the Jacobian determinant as in expression (B-8).

```
> funcXiEta := funcXY*detJ1;
```

$$\begin{aligned} funcXiEta := & ((v1_1(-.5\xi-.5\eta)+v2_1(.5+.5\xi)+v3_1(.5+.5\eta))^2 \\ & - 2(v1_1(-.5\xi-.5\eta)+v2_1(.5+.5\xi)+v3_1(.5+.5\eta))COR_1 + COR_1^2 \\ & + (v1_2(-.5\xi-.5\eta)+v2_2(.5+.5\xi)+v3_2(.5+.5\eta))^2 \\ & - 2(v1_2(-.5\xi-.5\eta)+v2_2(.5+.5\xi)+v3_2(.5+.5\eta))COR_2 + COR_2^2)^{1/2} \\ & (-.25 v2_1 v1_2 + .25 v2_1 v2_2 + .25 v1_2 v3_1 - .25 v2_2 v3_1) \end{aligned}$$

Following are the vertices' coordinates of TriPoly2 at the given orientation obtained from Matlab (locally measured from the part's COM).

```
> v1 := [-0.4107, -0.6220]; v2 := [1.3213, 0.3780]; v3 := [-0.9107, 0.2440];
```

$$v1 := [-.4107, -.6220]$$

$$v2 := [1.3213, .3780]$$

$$v3 := [-.9107, .2440]$$

Also, the coordinates for an arbitrary COR point (locally measured from the part's COM).

```
> COR := [-1.9054, -2.8859];
```

$$COR := [-1.9054, -2.8859]$$

```
> simplify(funcXiEta);
```

$$.00005580000000 (.99995600 \cdot 10^8 \xi^2 + .685263240 \cdot 10^9 \xi + .24998900 \cdot 10^8 \eta^2 + .171316540 \cdot 10^9 \eta + .1467522410 \cdot 10^{10})^{1/2}$$

Now, introduce the linear transformation, expression (B-10).

```
> eta := (1-xi)*lambda-1;
```

$$\eta := (1 - \xi) \lambda - 1$$

Then, the Jacobian for the linear transformation followed by its determinant.

```
> J2 := matrix(2,2,[ diff(xi,xi), diff(eta,xi), diff(xi,lambda), diff(eta,lambda) ]);
```

$$J2 := \begin{bmatrix} 1 & -\lambda \\ 0 & 1 - \xi \end{bmatrix}$$

```
> detJ2 := det(J2);
```

$$\det J2 := 1 - \xi$$

The following equation is the equation  $h(\xi, \lambda)$ , which is the equation  $g(\xi, \eta)$  multiplied by the new Jacobian above. Hence, this completes the transformation process as it appears in expression (B-12) and it is ready for simple integration over a rectangular area.

```
> funcXiLambda := funcXiEta*detJ2;
```

$$funcXiLambda := .5580000000 ((.86600 \xi - .25000 (1 - \xi) \lambda + .45530)^2 + 6.186052800 \xi + 1.546489400 (1 - \xi) \lambda + 12.98986561 + (.50000 \xi + .43300 (1 - \xi) \lambda - .12200)^2)^{1/2} (1 - \xi)$$

Execute first (inner) integral with respect to  $\xi$ , where the limits of integration go from -1 to +1.

```
> first := simplify(int(funcXiLambda, xi = -1..1));
```

$$\begin{aligned} first := & -2000000000 \cdot 10^{-13} (-1288931754 \cdot 10^{12} \sqrt{\%2} \lambda \sqrt{\%1} - 2256627855 \cdot 10^{10} \lambda^3 \sqrt{\%2} \sqrt{\%1} \\ & + .3219638442 \cdot 10^{16} \lambda^2 \sqrt{\%1} + .5501427560 \cdot 10^{16} \lambda \sqrt{\%1} - .5685339675 \cdot 10^{16} \sqrt{\%1} \\ & - .1454207263 \cdot 10^{19} \%4 - .6632031025 \cdot 10^{18} \lambda^3 \%3 + .4112243457 \cdot 10^{19} \lambda^2 \%3 \\ & + .1302196217 \cdot 10^{12} \sqrt{\%2} \sqrt{\%1} - .8344393835 \cdot 10^{11} \sqrt{\%2} \lambda^2 \sqrt{\%1} - .4112243457 \cdot 10^{19} \lambda^2 \%4 \\ & + .5106334555 \cdot 10^{19} \lambda \%3 - .5106334555 \cdot 10^{19} \lambda \%4 + .6632031025 \cdot 10^{18} \lambda^3 \%4 \\ & + .1454207263 \cdot 10^{19} \%3 - .3720000001 \cdot 10^{10} \sqrt{\%2} \lambda^4 \sqrt{\%1}) / ((4 + \lambda^2)^2 \sqrt{\%1}) \end{aligned}$$

```

%1 := 999956. + 249989.  $\lambda^2$ 
%2 := .735937130  $10^9$  + .99995600  $10^8 \lambda^2$  + .242637480  $10^9 \lambda$ 
%3 := ln(.24263602  $10^8 \sqrt{\%1}$  - .4999780  $10^7 \lambda^2 \sqrt{\%1}$  - .6065937  $10^7 \lambda \sqrt{\%1}$  + 999956.  $\sqrt{\%2}$ 
+ 249989.  $\sqrt{\%2} \lambda^2$ )
%4 :=
ln(.44262722  $10^8 \sqrt{\%1}$  - .6065937  $10^7 \lambda \sqrt{\%1}$  + .4589420710  $10^{11}$  + .1147355177  $10^{11} \lambda^2$ )
[ Execute second (outer) integral with respect to lambda, where the limits of integration go from 0 to
+1.
[ > second := evalf( Int( first, lambda = 0..1 ));
                                second := 3.880128224
[ The end result of the integration componenet in equation (2-13) is the scalar value dr.
[ > dr := second;
                                dr := 3.880128224
[ >
[ End of FEM sample calculation.

```

## Appendix C

### Force/Torque Sensor Specifications

Table C-1 outlines the force/torque sensor specifications as directly obtained from [33].

**Table C-1 Specifications for Nano Force/Torque sensor model FT3629.**

Transducer Model	Nano		
Standard Metric Calibrations	50/500	25/250	12/125
Sensing Ranges			
$\pm$ Force $x$ and $y$ range, (N)	50	25	12.5
$\pm$ Force $z$ range, (N)	90	45	22.5
$\pm$ Torque range, (N-mm)	500	250	125
Resolution			
$F_x, F_y$ , (N)	0.05	0.025	0.0125
$F_z$ , (N)	0.10	0.050	0.0250
$T_x, T_y, T_z$ , (N,mm)	0.25	0.125	0.0625
Counts Measurement Value			
$F_x, F_y, F_z$ , (counts/N)	20	40	80
$T_x, T_y, T_z$ , (counts/N-mm)	4	8	16
Overload Protection			
Max. Fxy allowable, ( $\pm$ N)	350		
Max. Fx allowable, ( $\pm$ N)	800		
Max. Txyz allowable, ( $\pm$ N-m)	2.5		

The experiments in Chapter 5 were performed while using the 25/250 metric calibration set.



## Appendix D

# Simple Moving Averages and The Least Squares Method

### D1 – Simple Moving Averages

A moving average is a smoothing technique used to isolate a trend from short term fluctuations [31], and simple moving averages is a form of averaging in which all values of interest are given the same weight, that is, no single value is to affect the resulting average more than others. Also, the effect of this technique is limited to the number of periods in the average. To calculate the new average start with the “oldest” period specified by the degree  $n$ , and then add up the values for the number of periods specified. The sum is then divided by the number of periods [31] as follows:

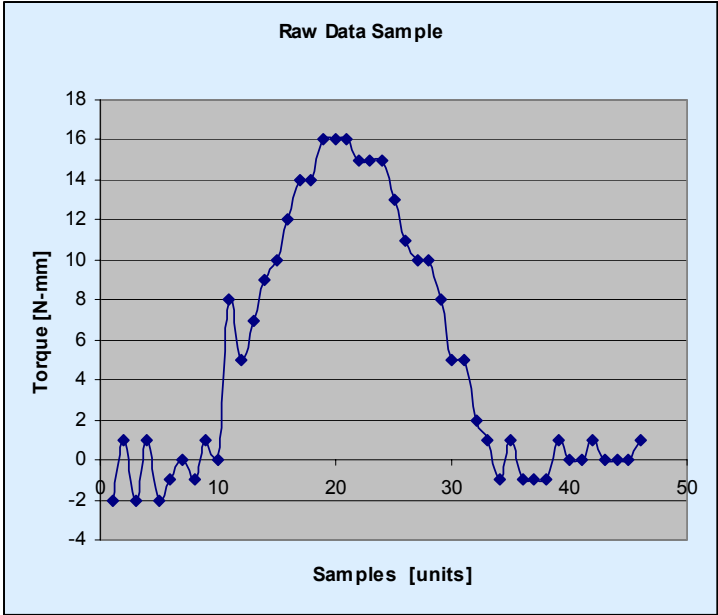
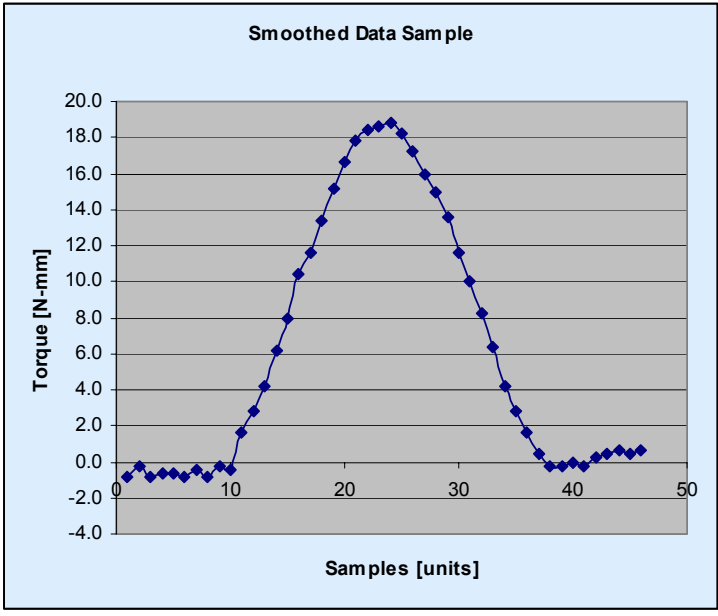
$$MA = \left( \frac{P_t + P_{t-1} + P_{t-2} + \dots + P_{t-n} + 1}{n} \right) \quad (D-1)$$

Where:

- $P_t$  is the selected value of interest
- $P_{t-1}$  is the value of 1 period back
- $n$  is the number of periods (degree)
- $MA$  is the new averaged value of interest replacing the current value of  $P_t$ .

To exemplify the simple moving averages, an arbitrary set of F/T data points were randomly selected. These points are tabulated in Table D-1 below, where calculations are carried out using a degree of  $n = 5$ .

**Table D-1** Sample data depicting the simple moving averages method. The raw data shows  $n$  extra points which are simply repetitions of the first  $n$  points in the list to calculate the smoothed data points. Figure (a) depicts the raw data plot, while figure (b) illustrates the smoothed data plot using degree of  $n = 5$ .

Raw Data	Smoothed Data	
-2	-	
1	-	
-2	-	
1	-	
-2	-	
-2	-1.0	
1	-0.4	
-2	-1.0	
1	-0.4	
-2	-1.0	
-1	-0.8	
0	-0.4	
-1	-0.8	
1	-0.2	
0	-0.4	
8	1.6	
5	2.8	
7	4.2	
9	6.2	
10	8.0	
12	10.4	
14	11.6	
14	13.4	
16	15.2	
16	16.6	
16	17.8	
15	18.4	
15	18.6	
15	18.8	
13	18.2	
11	17.2	
10	16.0	
10	15.0	
8	13.6	
5	11.6	
5	10.0	
2	8.2	
1	6.4	
-1	4.2	
1	2.8	
-1	1.6	
-1	0.4	
-1	-0.2	
1	-0.2	
0	0.0	
0	-0.2	
1	0.2	
0	0.4	
0	0.6	
0	0.4	
1	0.6	

(a)

(b)

## D2 – Least Squares Method

The least squares method is a popular method used for fitting curves to given sets of data points in order to develop an expression that describes the relationship among the variables of the problem. The objective is to find the curve that “best” fits the given data, and hence best approximating the given data. By “best fit” the goal is to minimize the sum of the squares of the distance between the given data points and the curve fitting the data. The procedure [30] is outlined below.

Fit a polynomial  $y(x) = \alpha_0 + \alpha_1 x + \alpha_2 x^2 + \dots + \alpha_{n-1} x^{n-1}$  of  $n$ th order to the set of data points  $(x_1, y_1), (x_2, y_2), \dots, (x_m, y_m)$  where  $m > n$ . The order of the polynomial is chosen depending on the application and accuracy of the fit desired. The function is thus written as:

$$y(x_i) = Ax_i \text{ where } i = 1..m$$

$$\begin{bmatrix} y_1 \\ y_2 \\ \vdots \\ y_m \end{bmatrix} = \begin{bmatrix} 1 & x_1 & x_1^2 & \cdots & x_1^{n-1} \\ 1 & x_2 & x_2^2 & \cdots & x_2^{n-1} \\ \vdots & \vdots & \vdots & \ddots & \vdots \\ 1 & x_m & x_m^2 & \cdots & x_m^{n-1} \end{bmatrix} \begin{bmatrix} \alpha_0 \\ \alpha_1 \\ \vdots \\ \alpha_{n-1} \end{bmatrix} \quad (\text{D-2})$$

Then, the error is calculated as:

$$e_i = y(x_i) - A_i x_i \quad (\text{D-3})$$

And therefore, the total error is:

$$e_t = \sum_{i=1}^n e_i = \sum_{i=1}^n (y(x_i) - A_i x_i) = Y - AX \quad (\text{D-4})$$

Now, the objective is to minimize the encountered error:

$$\min \|e_t\|^2 = \min \|Y - AX\|^2 \quad (\text{D-5})$$

Expand the error expression:

$$\begin{aligned}
 \|Y - AX\|^2 &= (Y - AX)^T (Y - AX) \\
 &= (Y^T - X^T A^T)(Y - AX) \\
 &= Y^T Y - Y^T AX - X^T A^T Y + X^T A^T AX
 \end{aligned} \tag{D-6}$$

Now, differentiate with respect to  $X$  and set to zero.

$$\begin{aligned}
 2A^T AX - A^T Y - A^T Y &= 0 \\
 A^T AX &= A^T Y
 \end{aligned} \tag{D-7}$$

Assuming  $A$  is full rank then  $(A^T A)$  is invertible, solve for the minimizing vector  $X^*$ :

$$X^* = (A^T A)^{-1} A^T Y \tag{D-8}$$

Where  $(A^T A)^{-1} A^T$  is the left inverse of  $A$ .

$X^*$  is therefore the minimizing vector made up of the coefficients  $\alpha_0, \alpha_1, \alpha_2, \dots, \alpha_{n-1}$  corresponding to the polynomial  $y(x) = \alpha_0 + \alpha_1 x + \alpha_2 x^2 + \dots + \alpha_{n-1} x^{n-1}$  that “best” fits the given data points  $(x_1, y_1), (x_2, y_2), \dots, (x_m, y_m)$ .

# **Appendix E**

## **Dynamic Pins**

Dynamic pins are one of the overhead pin classes defined in Chapter 1 of this thesis, and as per definition, dynamic pins are pins capable of moving along the y-axis over the conveyor belt, perpendicular to the direction of motion of the conveyor belt. The purpose of using dynamic or moving pins is to induce a larger amount of rotation to a given part traveling on a conveyor belt in a given contact configuration than by using a static pin; thus, “pushing” the polygon to a different final orientation not reachable by the motion caused by contact with the static pin.

The study of incorporating dynamic pins, with or without sensors, to the mechanics-based hybrid part feeder is left as a recommendation for future work. Thus, the objective of this appendix is to present the notion of using dynamic pins towards the development of the multi-agent system that is the mechanics-based hybrid part feeder. In addition, preliminary work done by the author through basic motion simulations using the model presented in Chapter 2 have demonstrated encouraging results that point towards the positive usability of dynamic pins. Consequently, the results presented here may be seen as introductory work towards the usability of dynamic pins in a part feeder.

### **E1 – Motion Modeling using Dynamic Pins**

To model the motion of a polygonal part traveling over a conveyor belt moving at constant speed and being acted upon by a dynamic pin in a direction perpendicular to the direction of the belt’s motion, the modeling approach presented in Chapter 2 was extended. Here the assumptions of constant and even pressure distribution as well as known and constant contact friction are applicable. And so, the motion of the part due to

the combined effects of the conveyor motion and the movement of the pin, are modeled as two individual pushes on the part perpendicular to each other as illustrated in Figure E-1. For each push, an instantaneous COR is determined by minimizing the energy equation (2-13) as before, and the corresponding amount of rotation about each COR is determined.

Throughout the motion simulation, the infinitesimal rotation and translation amounts corresponding to one instantaneous push (e.g.  $x$ -axis) are added together with the infinitesimal rotation and translation amounts of the second instantaneous push (e.g.  $y$ -axis) in order to formulate the resultant combined motion of the part due to the two pushes. Consequently, the overall motion of the part in contact with the dynamic pin is modeled as a linear combination of the two pushes  $P_x$  and  $P_y$ . In addition, the instantaneous position of the dynamic pin is calculated due to its infinitesimal motion along the  $y$ -axis, and subsequently the new point of contact with the part is determined.

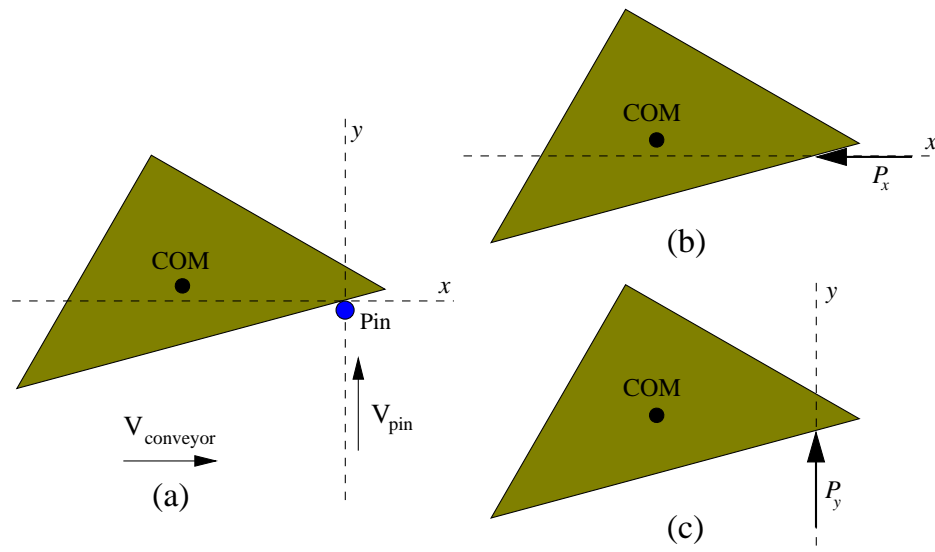
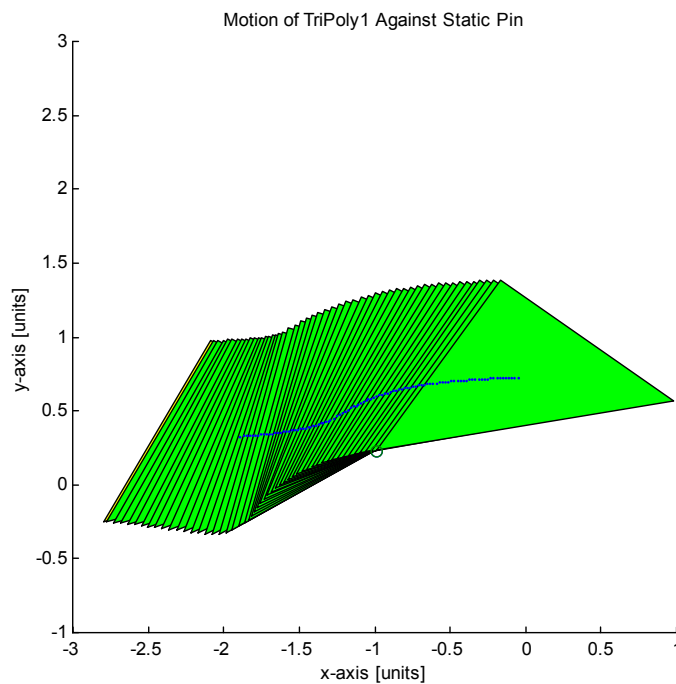


**Figure E-1** (a) Combined conveyor and pin motions, (b) push due to conveyor motion and (c) push due to pin motion.

## E2 – Preliminary Results

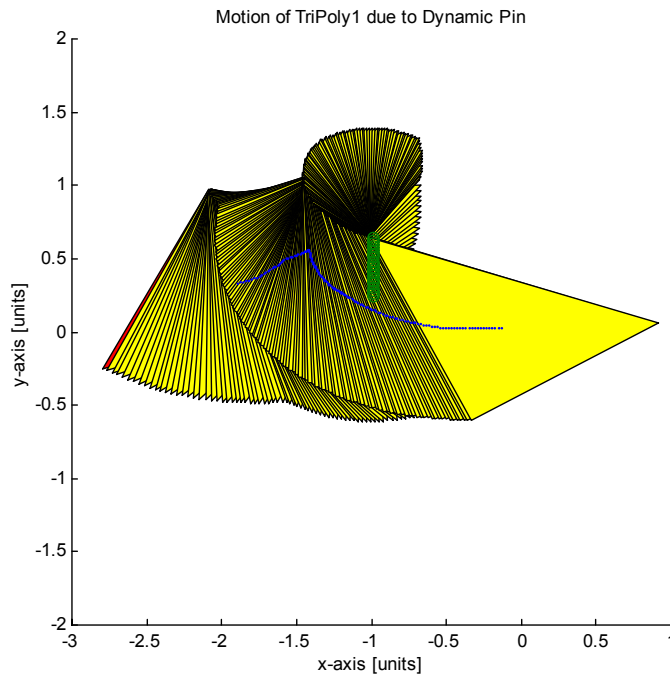
The method of modeling the combined effects of motion described above was applied to the two final orientations of the symmetrical triangular polygon used in this thesis, TriPoly1. The reason behind selecting these two orientations lies on the desire to further orient the part to a single final orientation. After developing a method using a force/torque (F/T) sensor to distinguish which of the two possible orientations, (Orientation 1 or Orientation 2), occurs, now it is of interest to use a dynamic pin to move Orientation 1 into 2 or vice versa and hence obtain a single final orientation.

Figure E-2 illustrates the motion of TriPoly1 against a static pin ( $d = -0.1$ ), where its initial orientation corresponds to that of Orientation 1 at  $\theta_i = 15^\circ$ . At the end of contact, the part has rotated slightly to  $\theta_f = 9^\circ$ , but within the findings in this thesis, this final orientation corresponds to the set of Orientation 1 as well, and has therefore not changed orientation.



**Figure E-2 Motion of TriPoly1 against a static pin - remains in Orientation1**

Figure E-3 on the other hand, shows TriPoly1 in the same initial contact configuration ( $d = -0.1$  and  $\theta_i = 15^\circ$ ), but this time contact occurs against a dynamic pin. The dynamic pin here moves along the positive direction on the  $y$ -axis and is brought to a halt once it has reached the equivalent distance of  $d = 0.15$  “above” the part's COM. At this point, the part is “free” from Orientation 1 and is capable of rotating to a different final orientation. This figure, hence illustrates that using a dynamic pin it may be possible to further orient TriPoly1 from Orientation 1 to Orientation 2. Note that in these simulation trials, it is assumed that the dynamic pin moves at the same slow speed as the conveyor belt, and therefore, the separate effects of motion occur at the same rate.



**Figure E-3 Motion of TriPoly1 due to dynamic pin:  $\theta_i = 15^\circ \rightarrow \theta_f = 163.2^\circ$ .**

Similarly, Figure E-4 and Figure E-5 depict the motion of TriPoly1 initially at Orientation 2 against a static and a dynamic pin respectively. In the case of the static pin,



the part rotates from  $\theta_i = 160^\circ$  to  $\theta_f = 157.1^\circ$ , and therefore shows that the part remains in Orientation 2. However, in the case of the dynamic pin, the part has rotated from  $\theta_i = 160^\circ$  to  $\theta_f = 297.5^\circ$ , indicating that TriPoly1 has moved away from Orientation 2 into another of the possible orientations for the given geometry, and can be oriented further if desired.

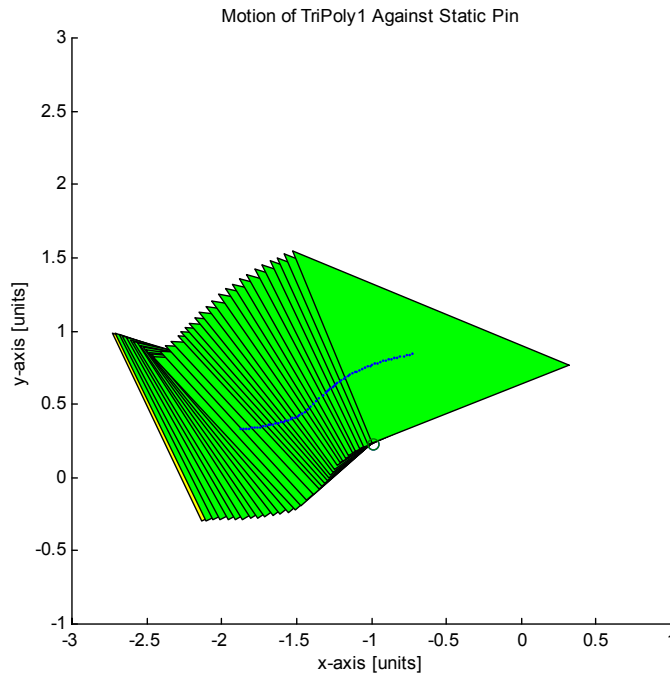


**Figure E-4 Motion of TriPoly1 against a static pin - remains in Orientation2.**

In short, the preliminary work shown in this appendix may be used as introductory work in the study of the applicability of overhead dynamic pins towards the design of a more complete mechanics-based hybrid part feeder. Further, the results presented here can be used to complement the findings in this thesis. For example, in the case of TriPoly1 after using the F/T sensor to find which of the two possible final orientations occurs, a single dynamic pin can be used to further orient all cases of Orientation1 into Orientation 2. And through online planning, whenever a case of

Orientation 2 is detected the dynamic pin at the end of the sequence is relinquished motion thus making it a static pin for that case, and therefore leaving all cases of Orientation 2 unchanged. As a result, TriPoly1 may be oriented to a single final orientation set from any possible initial state.

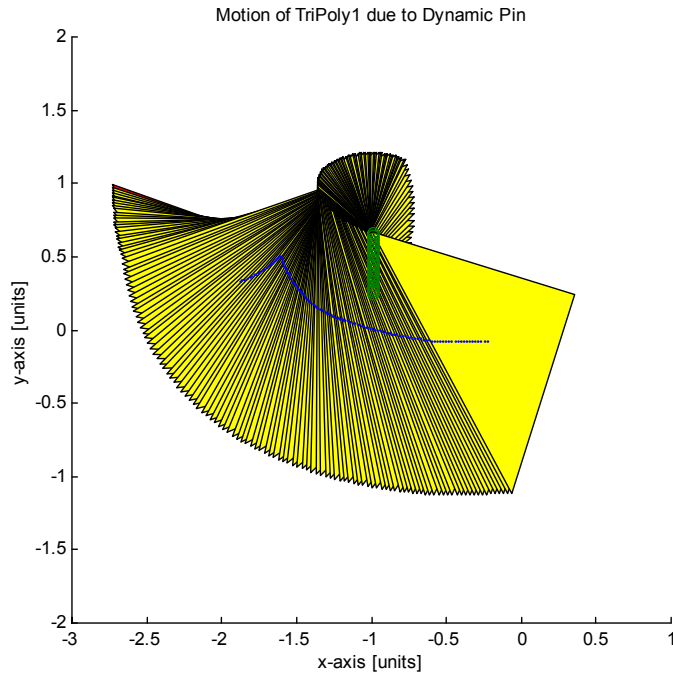


**Figure E-5 Motion of TriPoly1 due to dynamic pin: :  $\theta_i = 160^\circ \rightarrow \theta_f = 297.5^\circ$**

## Appendix F

### Timing Throughout Contact

Another aspect of interest that arose as a discussion topic near the end of this thesis's work, but was left as an indication towards possible future investigation was that of timing throughout the period of contact between the polygonal part and the pin. It was hypothesized that determining the time from the beginning of contact,  $t_i$ , to the end of contact,  $t_f$ , as illustrated in Figure 6-2 could also provide information to assist in the planning process. Thus, it may be asked, can the timing information be used to distinguish the possible states (initial or final) of the part? Or can the sequential timing between static pins be used by the dynamic pins to plan the manipulation movements to orient a given part?

To commence investigating this notion, motion simulations using the model presented in Chapter 2 were executed where the time elapsed throughout the period of contact was calculated. For this purpose, it was assumed that the conveyor belt moves at a slow constant rate of 0.02 m/s to remain within the quasi-static domain.

Table F-1 outlines partial results pertaining to the motion simulations for the three initial states of TriPoly1 ( $0^\circ$ ,  $135^\circ$  and  $225^\circ$ ) and contact parameter values of 0.1, 0.2, 0.3, -0.1, -0.2 and -0.3 (see Figure F-1). In this preliminary study, time differences greater than one second (1 sec) between different initial states are considered large enough to distinguish the initial states. This threshold of 1 sec was selected because referring to the times recorded it constitutes a large portion of their values; hence, any timing values that differ by more than this threshold of 1 sec are considered distinct.

Subsequently, the tabulated results in Table F-1 indicate that for all positive contact parameters explored, distinct time is obtained for each initial state. So, these

distinct times would allow for immediate recognition of the initial state to contact the pin and therefore recognizing its orientation. However, the same is not observed for the negative parameter values in the table. Here, initial states with angles  $0^\circ$  and  $135^\circ$  do not show clearly distinct times from each other, but these are different from  $225^\circ$ . Hence, in a similar fashion to the force/torque sensor introduced in Chapter 5, two of the initial states can be recognized. Thus, for future work, cases where the same timing corresponds to different initial conditions need be investigated and verified experimentally.

**Table F-1 Partial timing results throughout period of contact between part TriPoly1 and the pin for various contact parameter values.**

$d$	Initial Angle, $\theta_i$	Final Angle, $\theta_f$	Time (sec)	$d$	Initial Angle, $\theta_i$	Final Angle, $\theta_f$	Time (sec)
0.1	$0^\circ$	$20.5^\circ$	<b>2.6</b>	-0.1	$0^\circ$	$-119.9^\circ$	<b>6.4</b>
0.1	$135^\circ$	$166.8^\circ$	<b>3.7</b>	-0.1	$135^\circ$	$17.2^\circ$	<b>6.45</b>
0.1	$225^\circ$	$301.5^\circ$	<b>5.65</b>	-0.1	$225^\circ$	$162.3^\circ$	<b>3.7</b>
0.2	$0^\circ$	$21.8^\circ$	<b>2.2</b>	-0.2	$0^\circ$	$-116.5^\circ$	<b>5.95</b>
0.2	$135^\circ$	$167.1^\circ$	<b>3.4</b>	-0.2	$135^\circ$	$19.9^\circ$	<b>6.05</b>
0.2	$225^\circ$	$300.6^\circ$	<b>4.7</b>	-0.2	$225^\circ$	$165.7^\circ$	<b>2.9</b>
0.3	$0^\circ$	$21.8^\circ$	<b>1.95</b>	-0.3	$0^\circ$	$-112.2^\circ$	<b>5.75</b>
0.3	$135^\circ$	$166.3^\circ$	<b>3</b>	-0.3	$135^\circ$	$24.2^\circ$	<b>5.9</b>
0.3	$225^\circ$	$298.5^\circ$	<b>4.25</b>	-0.3	$225^\circ$	$171.7^\circ$	<b>2.4</b>

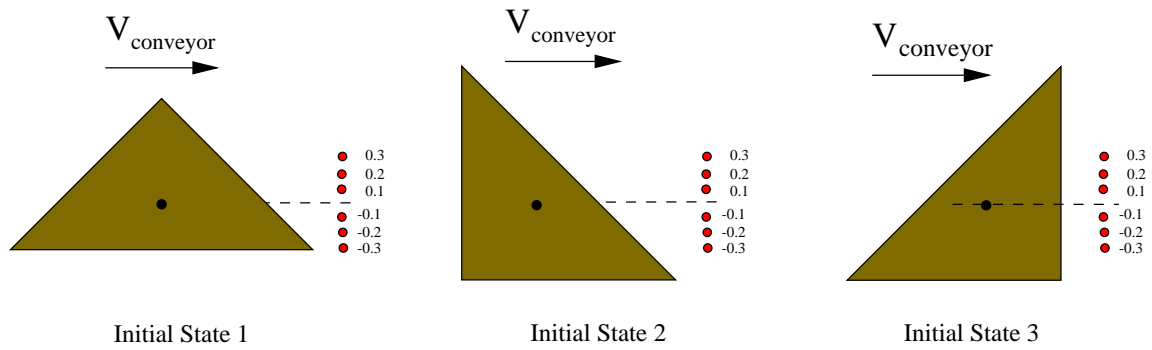


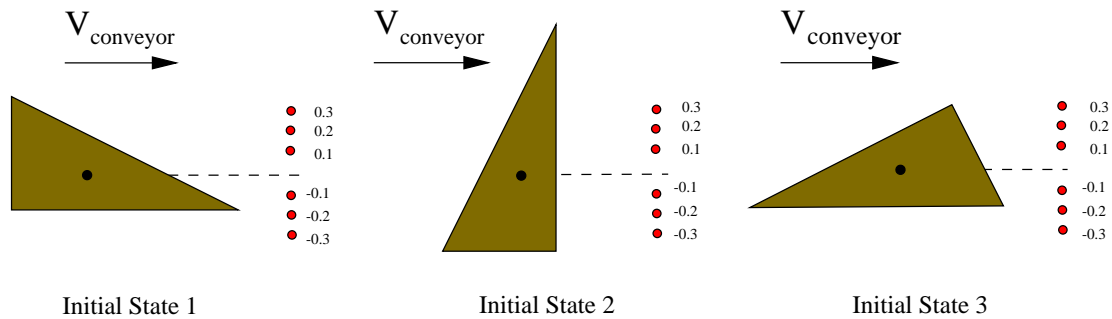
**Figure F-1 TriPoly1 in its three initial states ( $0^\circ$ ,  $135^\circ$  and  $225^\circ$ ) with pins corresponding to the given contact parameter values (0.3, 0.2, 0.1, -0.1, -0.2, 0.3).**

Further, note that for each initial state, say  $0^\circ$ , the time increases as the magnitude of  $d$  decreases. This occurs when the COM of the part is perpendicularly closer to the pin, and hence conforms with earlier findings in this thesis (refer to Chapter 3), that larger amounts of sticking and rotation do indeed occur when the part's COM is perpendicularly closer to the pin, thus extending the period of contact between the pin and the part.

Similar results were tabulated in Table F-2 for TriPoly2, again using contact parameter values of 0.1, 0.2, 0.3, -0.1, -0.2 and -0.3 and the polygon's initial states ( $0^\circ$ ,  $90^\circ$  and  $206^\circ$ ) as the initial contact configurations (see Figure F-2). Again, some cases show clearly distinct times, particularly those of  $\theta_i = 90^\circ$  and positive  $d$ . For the other two initial states the difference in time can be considered not large enough ( $< 1$  sec) to clearly distinguish between the two, but this can only be verified experimentally. On the other side, for negative  $d$  only the first initial state,  $\theta_i = 0^\circ$ , appears to be distinguishable for  $d = -0.1$  and  $d = -0.2$ , while  $d = -0.3$  indicates a no-contact (N/C) scenario. The other two states again don't display a timing difference large enough to clearly distinguish between the two.

**Table F-2 Partial timing results throughout period of contact between part TriPoly2 and the pin.**

$d$	Initial Angle, $\theta_i$	Final Angle, $\theta_f$	Time (sec)	$d$	Initial Angle, $\theta_i$	Final Angle, $\theta_f$	Time (sec)
0.1	0°	13.9°	<b>3.3</b>	-0.1	0°	7.9°	<b>5.3</b>
0.1	90°	167.4°	<b>5.65</b>	-0.1	90°	27.4°	<b>3.75</b>
0.1	206°	234.8°	<b>3.9</b>	-0.1	206°	117.8°	<b>4.3</b>
0.2	0°	15.5°	<b>2.2</b>	-0.2	0°	-139°	<b>9.1</b>
0.2	90°	165.1°	<b>5.25</b>	-0.2	90°	31.4°	<b>3.3</b>
0.2	206°	234.4°	<b>2.95</b>	-0.2	206°	130.1°	<b>3.55</b>
0.3	0°	12.5°	<b>1.75</b>	-0.3	0°	N/C	<b>N/C</b>
0.3	90°	161.9°	<b>4.9</b>	-0.3	90°	37.6°	<b>2.7</b>
0.3	206°	233.9°	<b>2.05</b>	-0.3	206°	N/C	<b>N/C</b>

**Figure F-2 TriPoly2 in its three initial states (0°, 90° and 206°) with pins corresponding to the given contact parameter values (0.3, 0.2, 0.1, -0.1, -0.2, 0.3).**

As for finding a solution towards the problem of part orienting, another possibility is to use the timing values obtained here for the given and various contact configurations sequentially. That is, use the timing value against one static pin followed by the timing value against another static pin and so on, in order to narrow the possible sets of final configurations and then use dynamic pins to orient the part. Again, this notion is a recommendation and is left as future work.

Finally, the data presented here shows that the concept of contact timing may be used in the planning process, but requires further investigation, particularly experimental

trials. The main possible limitation observed here lies in the fact that even for the same contact configurations, the actual timing data obtained for different experimental trials might show discrepancies because in theory it is nearly impossible to tell whether the part sticks or slips. In the simulations, consistent data is obtained because the part's motion is modeled using a strict set of criteria indicated in Chapter 2 that in turn dictates the object's behaviour. But, in actuality these criteria may vary due to unknown factors such as the pressure distribution of the object, the frictional distribution at the object-surface interface, and varying friction at the point of contact due to irregularities on the part's edges and the pin. All of which have been assumed as known and constant in this study.

Of importance however, is to note that if the timing proves to be beneficial, a simpler mode of sensing can be used instead of the F/T sensor. Contact sensing can be carried out by much simpler sensors such as strain gauges and the data processing would not require empirical methods like the ones used in conjunction with the F/T sensor; hence, returning to the initial motivation of minimalism. Thus, it is recommended that experimental trials are carried out to test the usability of the timing information.

## Appendix G

# Preliminary Work Toward the Design of the Hybrid Gravity Part Orienter (HGPO)

As an extension to the work in this thesis, the novel idea of using pins mounted on a vertically slanted board and gravity as the main driving force to orient polygonal convex parts was briefly investigated. This notion of part orienting gave way to the conceptual beginning of the hybrid gravity part orienter (HGPO), which hypothetically relies on using two layers of pins to orient a polygonal part. The first layer of pins is comprised of fixed sensorized (static) pins and the second layer consists of moving and/or retractable (dynamic) pins with or without sensors. As a planar convex polygon at an unknown initial configuration is dropped/released at the top of the feeder so as to travel down in between the pins, the part is subjected to contact with the static pins, causing it to rotate, slide and “bounce” off the pins. Thereby, the first layer of pins gathers information pertaining to the motion of the part, more specifically, the sensors (e.g. strain gauges) detect which pins the part contacts and the time in between contacts. Ideally, this information collected through the first layer of static pins will be used in a planner that will control the layer of dynamic pins; hence, providing the final “push” to the part in order to achieve its final configuration.

As preliminary work towards the development of the HGPO, this appendix investigates the part's motion through the layer of static pins. Here, the time duration of *events*, where events are defined as the part's behaviour in between pins, is determined and studied. The events are timed from the instance the part contacts a pin followed by its motion (i.e. rotation/translation) against that pin, breaks away from it and freely slides down the board until another pin is contacted. It is hypothesized that the expected timing



variables representing the events' timing can be used towards planning the actions by the layer of dynamic pins in order to orient the polygonal part.

In the sections to follow, the development of the mechanics-based modeling and simulation is presented along with a brief discussion of the resultant timing in between contacts for various configurations of the part falling between the static pins.

In reference to previous related work, the only other part orienting device known to have a similar setup using an array of retractable pins mounted on a vertical board is that of the “Pachinko Machine” by Blind et al. [5]. But in their work the part dynamics are not studied and hence the preliminary work in this appendix is seen as the beginning of what may be a contribution to part orienting under the effect of gravity.

## **G1 – Modeling**

First, the assumptions applicable to the work in this appendix are as follows:

1. Motion is dynamic (driven by gravity).
2. Friction is modeled as Coulomb friction at all interactions.
3. Coefficient of friction  $\mu_s$  over the sliding surface is constant.
4. Coefficient of friction  $\mu_c$  at the point of contact between the part and the pin is known and constant throughout the period of contact.
5. Parts are polyhedral of constant polygonal cross sectional area
6. Pressure distribution is constant and uniform over the entire cross sectional area of the polygonal part.
7. The objects and pins are rigid.
8. Locations of the part vertices and center of mass (COM) are known.

Then, the setup of the first layer of pins used in this study is introduced and depicted in Figure G-1. Here, the global coordinate **G** and the moving local frame **L** used in the simulation are shown, as well as the intermediate frame **P**. **P** is applied

whenever the part is in contact with any of the pins and serves as an intermediate frame between **G** and **L**.

Contact between the part and the pin occurs at a single point (tangential to the surface of the pin), referred to as the *point of contact*, point  $P$ , also the point where the frame **P** is centered. Once the part comes into contact with a pin (ignoring the impact phase for now), two outcomes are possible: 1) clockwise (CW) rotation with or without sliding and 2) counter-clockwise (CCW) rotation with or without sliding. The outcome depends on the position of the part's center of mass COM with respect to the pin as well as the momentum (linear and angular) of the part prior to contact. The event outcomes from pin contact are tabulated in Table G-1, also labeled in Figure G-1. The distance between pins is decided such that only a one-point contact is possible at any given time. Thus, the distance must be greater than the maximum diameter of a given part, where the diameter is the distance resulting from capturing the part with two parallel plates, or the maximum distance between any two vertices on the part.

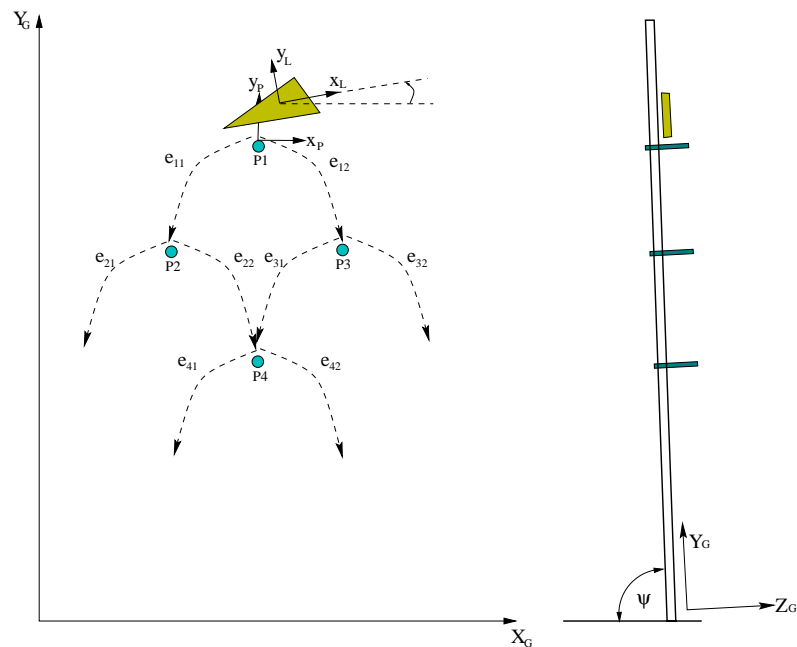


**Figure G-1 Setup of passive pin arrangement with coordinate frames and possible events. Left: Front view. Right: Side view.**

**Table G-1 Possible events per pin (refer to Figure G-1). Subscript notation:  $e_{ij,edge}$  where  $i$ , refers to the pin number;  $j$  refers to the rotation sense (1=CCW, 2=CW); *edge* refers to the edge the part was initially in contact with. The labels P1-P4 refer to the pins and the label “out” indicates when a part falls outside of the area of the pins and can no longer contact any of them.**

Pin 1:	$e_{11,edge} = P1 \rightarrow P2$ (CCW rotation) $e_{12,edge} = P1 \rightarrow P3$ (CW rotation)
Pin 2:	$e_{21,edge} = P2 \rightarrow \text{out}$ (CCW rotation) $e_{22,edge} = P2 \rightarrow P4$ (CW rotation)
Pin 3:	$e_{31,edge} = P3 \rightarrow P4$ (CCW rotation) $e_{32,edge} = P3 \rightarrow \text{out}$ (CW rotation)
Pin 4:	$e_{41,edge} = P4 \rightarrow \text{out}$ (CCW rotation) $e_{42,edge} = P4 \rightarrow \text{out}$ (CW rotation)

Subsequently, a mechanics-based modeling and simulation is developed and implemented to study the part's motion through the layer of passive pins. The part can undergo various modes of motion as follows:

1. Free-fall
2. Impact with pin (assumed to be minimal for now)
3. Rotation only about pin
4. Rotation and sliding about pin
5. Break away from pin – move to free-fall.

When a part first comes into contact with a pin and the event commences, it can either “stick” rotating only about the point of contact or it can begin to slip and thus, rotate and slide along the pin until losing contact with the pin and hence return to free fall until contacting another pin and begin another event.

Amongst one of the variables that dictates the motion of the part upon contacting the pin is the angle of board inclination,  $\psi$ . The angle of inclination affects the effect of gravity ( $F_g$ ) on the part as well as the effect of friction ( $F_f$ ), between the part and the

board on which it slides. Assuming a known and constant coefficient of sliding friction  $\mu_s$ , the direction is always parallel but in opposite direction to the direction of motion.

### G1.1 – Rotation About a Fixed Pin

Figure G-2 illustrates the Free Body Diagram (FBD) of the triangular polygon used in the modeling scenario of rotation about a fixed pin. When the amount of friction at the point of contact is larger than the resulting forces at that point, that is, when  $|f| \geq \mu_c |N|$  then the part rotates about the pin without slipping. Where  $f$  is the contact friction component parallel to the edge in contact with the pin,  $\mu_c$  is the coefficient of friction at the point of contact, and  $N$  is the normal force at the same point.

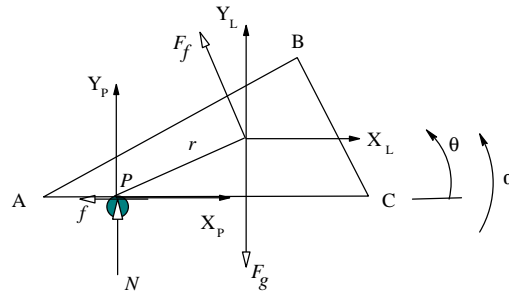


**Figure G-2 FBD of triangular polygon experiencing pure rotation against pin.**

The rotational motion of the triangular polygon in Figure G-2 is described by the second order differential equation:

$$\Sigma^{\mathbf{P}} \mathbf{M}_P = (\vec{F}_g \times \vec{r}) + (\vec{F}_f \times \vec{r}) = I_P \ddot{\theta} \quad (\text{G-1})$$

Where the upper-left superscript indicates the frame in reference, thus  $\mathbf{M}_P$  is in reference with frame  $\mathbf{P}$ . Also,  $I_P$  is the moment of inertia about the contact point  $P$  using the parallel axis theorem:  $I_P = I_{com} + mr^2$ , where,  $I_{com}$  is the moment of inertia about the part's COM and the force of friction,  $F_f$ , is directed parallel but in opposite direction to that of motion.

Furthermore, the position, velocity, and acceleration of the COM are calculated using the polar coordinates  $x = r \cos \theta$  and  $y = r \sin \theta$  with respect to the frame **P** as follows:

$$\begin{aligned}\vec{u} &= x\hat{i} + y\hat{j} = r \cos \theta \hat{i} + r \sin \theta \hat{j} \\ \dot{\vec{u}} &= \dot{x}\hat{i} + \dot{y}\hat{j} = -r\dot{\theta} \sin \theta \hat{i} + r\dot{\theta} \cos \theta \hat{j} \\ \ddot{\vec{u}} &= \ddot{x}\hat{i} + \ddot{y}\hat{j} = r\ddot{\theta}(-\sin \theta \hat{i} + \cos \theta \hat{j}) + r\dot{\theta}^2(-\cos \theta \hat{i} - \sin \theta \hat{j})\end{aligned}\tag{G-2}$$

Then to determine the instant at which the part begins to slide about the point of contact, it is necessary to calculate the normal and friction forces during the rotation phase. This is done using the following equations:

$$\begin{aligned}\Sigma^P \mathbf{F}_x &= N_x + f_x + F_{f_x} = m\ddot{x}_P \\ \Sigma^P \mathbf{F}_y &= N_y + f_y + F_{g_y} + F_{f_y} = m\ddot{y}_P\end{aligned}\tag{G-3}$$

Where  $\mathbf{F}_x$  and  $\mathbf{F}_y$  are in reference with frame **P**.

Making substitutions into expression (G-3), solve for  $N$  and  $f$ :

$$N = \cos \theta (m\ddot{y}_P - F_g - F_{f_y} - \tan \theta (m\ddot{x}_P - F_{f_x}))\tag{G-4}$$

$$f = \frac{-N \sin \theta + F_{f_x} - m\ddot{x}_P}{\cos \theta}\tag{G-5}$$

When friction reaches the slip threshold:  $|f| \geq \mu_c |N|$ , where  $\mu_c$  is the known static coefficient of friction at the point of contact, move onto the rotating and sliding model.

Thus, when  $|f| < \mu_c |N|$  slipping begins.

### G1.2 – Rotation and Sliding

When the slip-friction threshold is reached the part begins to slip past the point of contact along the pin, and the part instantaneously slides in the direction tangent to the pin while continuing to rotate, at this point  $f = \mu N$ . Figure G-3 depicts the FBD for the rotation and sliding situation.

The subsequent sum of forces resulting from the FBD with respect to the local frame **L** are as follows:

$$\begin{aligned}\Sigma^L \mathbf{F}_x &= -f + mg \sin \theta = m\ddot{x}_L \\ \Sigma^L \mathbf{F}_y &= N - mg \cos \theta = m\ddot{y}_L\end{aligned}\tag{G-6}$$

However, the sliding constraint allows only for motion parallel to the point of contact tangent along the local  $x$ -axis. Thus,  $\ddot{y}_L = 0$ , and so  $N = mg \cos \theta$ , and as a result,  $\ddot{x}_L = \frac{\mu N + mg \sin \theta}{m}$ . The linear acceleration is therefore, in vector form, with respect to the local frame **L** due to sliding:  ${}^L\vec{a}_L = [\ddot{x}_L \quad \ddot{y}_L \quad 0]$ . This must be mapped to the reference frame **P** about the pin, therefore, the acceleration due to rotation only with respect to frame **P** is:  ${}^P\vec{a}_p = [\ddot{x}_p \quad \ddot{y}_p \quad 0]$ . Thus, the overall acceleration is:  ${}^P\vec{a} = {}^P\vec{a}_p + {}^P\mathbf{R}^L\vec{a}_L$ . Where **R** is the rotation matrix that maps the acceleration about local frame **L** to the reference frame **P**.

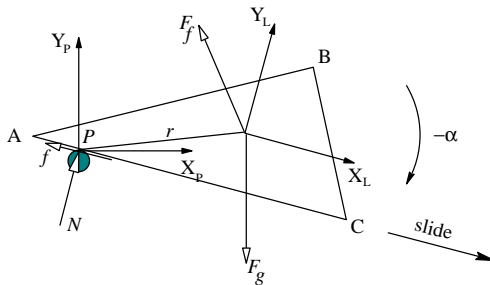


Figure G-3 FBD of triangular polygon experiencing rotation and slip against pin.

The part rotates and slides along the pin until separation between the part and the pin occurs. At that instance the part continues to translate in free fall until a new pin is contacted and the process repeated.

As for the determination of the timing variables, these are resolved using the dynamic equations of motion. In the proposed model, the part starts at rest in contact with a static pin, so time is calculated from the instance the part begins to rotate on this pin, also representing the beginning of an event, slides, free-falls and contacts another pin. At the instance of contact with the new pin, the timing of the event is complete and a new timing variable for a new event is initialized.

## **G2– Simulation Results**

Implementing the modeling equations from the previous section in Matlab yielded the plots found in Figure G-4, in which the part rotates about the first pin, then slides past it and finally separates continuing its motion in free falling mode until contacting a new pin (Pin2 on the left or Pin3 on the right). The time variables under study correspond to the time between motion initiation on the present pin and contacting a new pin. The known parameters in the study are: distance between pins, pin contacted (P2 or P3), and angle of sliding surface inclination, as well as the starting configuration of the part.

In the simulation trials three starting configurations were used. The initial conditions are set so that the initial angular and linear velocities are both zero, and the position and orientation of the part are set so that one of its three stable edges (i.e. edges AC, CB, BA) rests on the first pin and is parallel to the global  $x$ -axis. Then, for different simulation contact setups the position is varied by moving the part along the  $x$ -axis on both positive and negative directions; hence, moving the COM away from the point of contact  $P$ .

After some simulation runs, it was found that as the COM's position was moved away from the contact point at the pin, the resultant values for the time variables, that is,

the time duration of the events as the part traveled from one pin to the next, decreased. This time reduction is clearly justified by the fact that the angular acceleration increases by increasing the moment arm (distance  $r$ ), hence increasing the effect of gravity on the part.

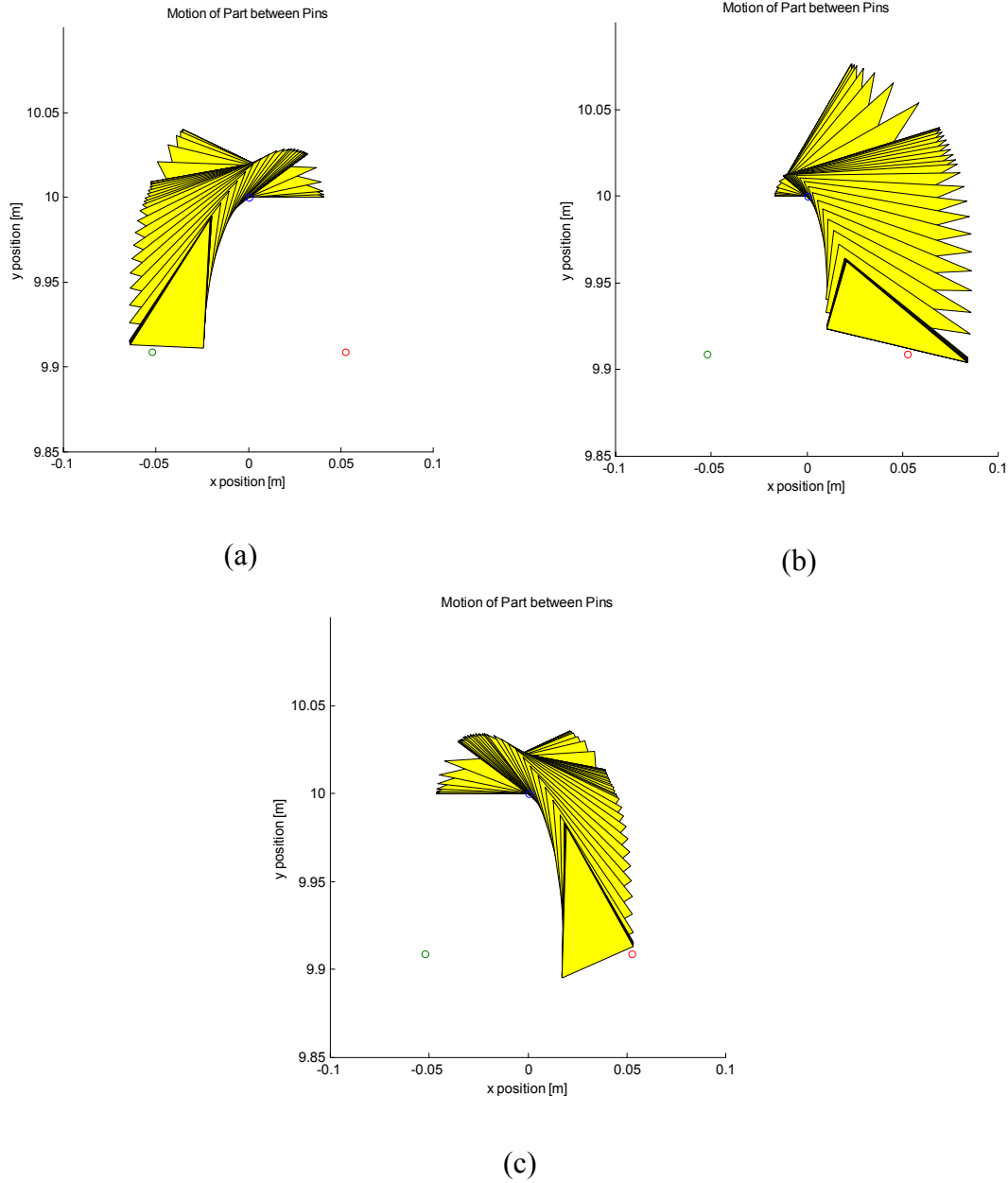


**Figure G-4 Polygon rotating, sliding and free falling about a pin with edge BA in (a), edge BC in (b), and edge AC (c) initially in contact with Pin 1.**



More specifically, studying the data obtained for starting edge CB, it was noted that rotation to the right (CW), event  $e_{12,CB}$ , reaches the second pin faster than when the part rotates to the left (CCW), event  $e_{11,CB}$ . This is supported by the fact that  $t_{11,CB} > t_{12,CB}$ , where the timing variables' are written in a similar fashion to that of the events. For each event  $e_{ij,edge}$  the corresponding timing variable is written as  $t_{ij,edge}$ , where  $t$  is the time,  $i$  refers to the pin number in contact with at the beginning of the event,  $j$  is the rotation sense, and  $edge$  refers to the edge of the part initially in contact with pin  $i$ .

Similarly, for starting edge BA, rotation to the left (CCW), event  $e_{11,BA}$ , reaches the second pin faster than when rotating to the right (CW), event  $e_{12,BA}$ , and this is supported by  $t_{11,BA} < t_{12,BA}$ . The time differences correspond to the order of 1/10 second, and it depends on the geometry of the part, the friction at the sliding surface, as well as the contact configuration with the pin at the beginning of the event. In comparison with the timing studied in the quasi-static domain in Appendix F the differences will be much smaller because in the dynamic environment the part travels at a higher speed.

Also, when comparing the timing data for the three edges as the part rotates CCW it was noted that the second pin was reached faster when edge BA was initially in contact with P1. The time variables are ordered as follows:  $t_{11,BA} < t_{11,AC} < t_{11,CB}$ . Similarly, when rotating CW the second pin is reached faster when edge CB is in contact with P1. The time relation in this case is:  $t_{12,CB} < t_{12,BA}$ , disregarding data for  $e_{12,AC}$  because numerous cases did not contact the second pin and are hence considered inconclusive.

Other than the timing variables' results, other observations were noted. Of interest are the amount of rotation from pin to pin as well as the part's edge to contact the second pin. For each event, a noticeable trend was seen. In most cases the part's edge to contact the second pin was the same throughout the event regardless of the angle  $\psi$  and the COM's position from the point of contact  $P$  with pin P1. However, for some cases discrepancies were noticed. In some cases the part would fall and rotate without contacting a pin on the second row at all, and in some cases the edge to contact the

second pin varied. The variation of edges here is referred to as *phase changes*, in which for a particular event as the distance between the center of mass and the contact point is varied the amount of rotation varies and hence causes a different edge to contact the second pin. This phenomenon is illustrated in Figure G-5.

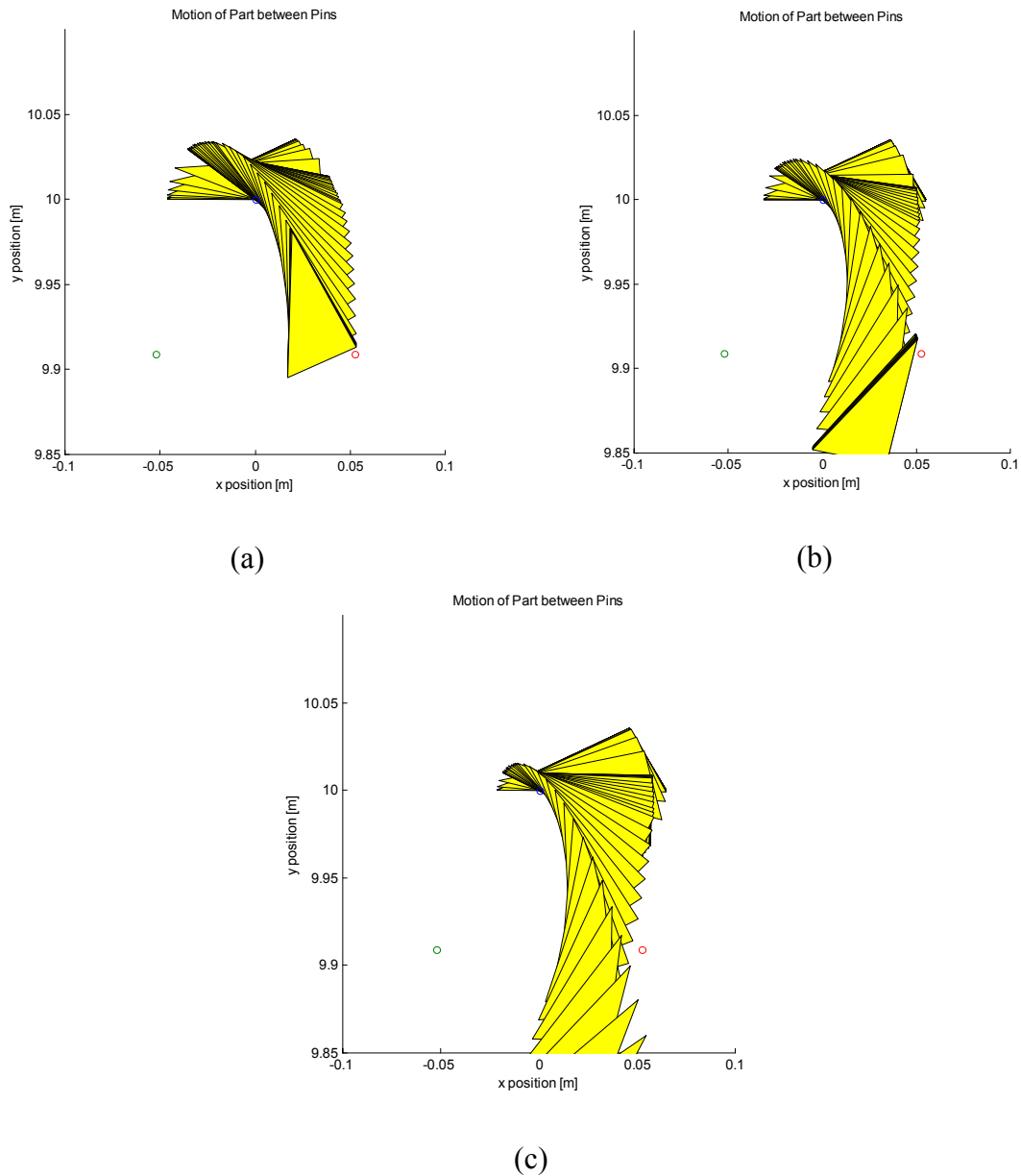


**Figure G-5** Phase changes illustrated by polygon rotating, sliding and free falling for event  $e_{12,AC}$ . Here, edge AC is initially in contact with pin P1. In (a) the polygon contacts P3 with edge BC, in (b) the polygon contacts pin P3 with edge BA, and in (c) the polygon does not contact either pin P2 or P3.

### G3 – Experimental Results

An experimental test-bed was developed using Plexiglas as the sliding surface and consisting of an array of aluminum alloy static pins with foil strain gauges as contact sensors as depicted in Figure G-6. Basic experimental trials were performed with the purpose of verifying the behaviour of the part as well as the resulting timing variables.

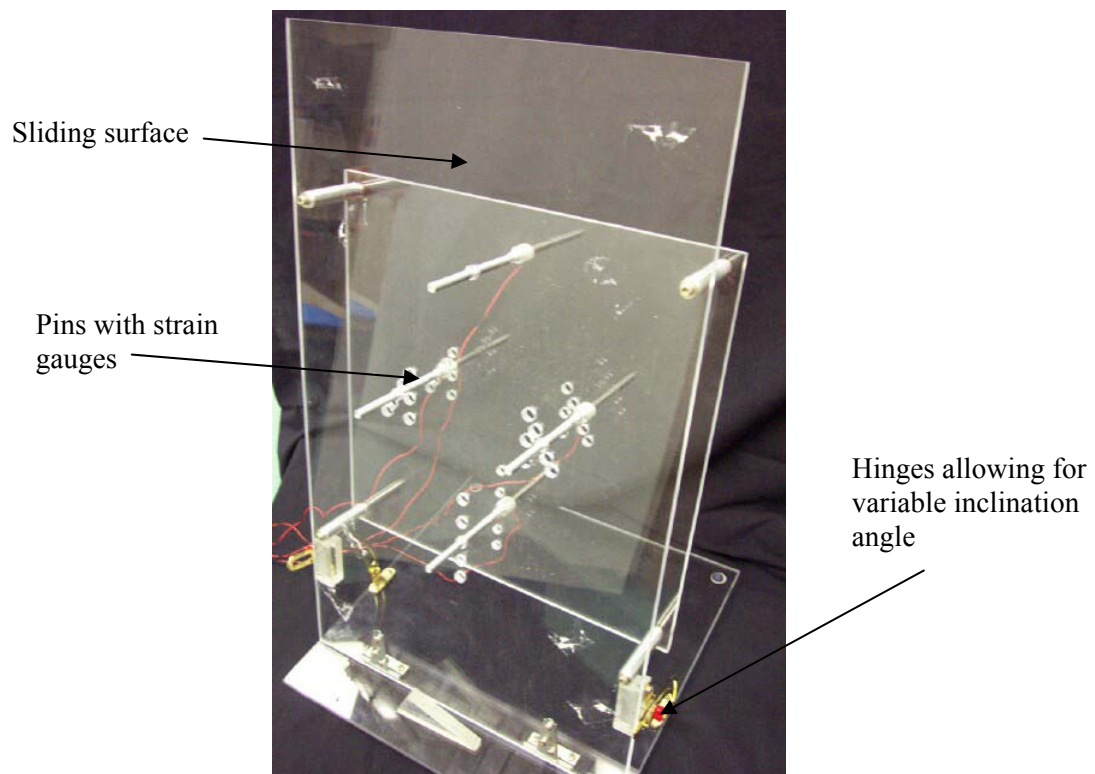


**Figure G-6** Picture of experimental test-bed for HGPO.

Comparatively, the behaviour of the part was observed to follow the motion modeled in the previous section. The approximate amount of rotation and the subsequent edges to contact the second pin matched for most compared cases. Unfortunately, complications were encountered when timing was tested, thus, yielding inconclusive results.

First, the angle of inclination  $\psi$  had to be kept to a near vertical stance in order to overcome the static friction at the sliding surface interface for the part to commence sliding freely driven by gravity alone. Consequently, the motion of the part resulted in greater speeds due to a larger effect of gravity on the part and less friction at the sliding surface. This unplanned increased speeds resulted in larger impact forces upon contact with a pin. Subsequently, the selected pin and strain gauge configuration produced much unwanted noise due to the vibration of the pin occurring at the moment of contact. Also, due to the part's impact on the pin, "bouncing" of the part on the pin was noted, resulting in consecutive instances of contact between the part with the same pin. This type of behaviour had not been included in the modeling phase because the impulse upon impact was deemed negligible for simplification of the model; however, an impact model must be added and this is left as future work.

Nonetheless, foam sleeves were attached to the pins in order to reduce the amount of vibration experienced by the pins upon contact with the part, although it doesn't solve the bouncing effect. The present design of the pins allows for a signal to be registered upon the part contacting a pin, but it does not register the instant when the part leaves or loses contact with a pin which is also of interest. This is mainly due to the poor sensitivity of the chosen sensors and the corresponding noise in the signal. These complications did not allow for proper verification of the modeled timing variables where a simplified model was applied.

#### **G4 –Conclusions and Future Work Recommendations**

One of the complications lies on the proper modeling of the part through the array of pins, therefore, it is recommended that further development is made in the mechanics-based modeling, particularly, the incorporation of an impact/impulse model such as the ones presented in [6] by Brach, [24] by Stewart, and [25] by Wang and Mason.

Further, having been able to reduce some of the vibration on the pins due to the part's impact on the pin, it is recommended that other sensors capable of greater sensitivity than foil strain gauges are used in the experimental phase, such as semiconductor strain gauges.

Finally, on the overall picture of the HGPO, it is recommended that planning methods be devised after successfully attaining useful information from the layer of static pins and that the dynamic layer be designed, whether it be dynamic pins or a dynamic fence as illustrated in Figure 6-3.

# Bibliography

- [1] S. Akella and M. T. Mason. Parts Orienting with Partial Sensor Information. In *IEEE International Conference on Robotics and Automation*, pp. 557-564, Leuven, Belgium, 1998.
- [2] S. Akella and M. T. Mason. Parts Orienting with Shape Uncertainty. In *IEEE International Conference on Robotics and Automation*, pp. 565-572, Leuven, Belgium, 1998.
- [3] S. Akella, W.H. Huang, K. M. Lynch, and M. T. Mason. Parts Feeding on a Conveyor with a One Joint Robot. *Algorithmica*, 26:313-344, 2000.
- [4] R.P. Berretty, K. Goldberg, M.H. Overmars, and A.F. van der Stappen. Orienting parts by inside-out pulling. In *IEEE International Conference on Robotics and Automation*, pp. 1053-1058, Seoul, Korea, 2001.
- [5] S.J. Blind, C.C. McCullough, S. Akella, and J. Ponce. A Reconfigurable Parts Feeder with an Array of Pins. In *IEEE International Conference on Robotics and Automation*, pp. 147-153, San Francisco, CA, 2000.
- [6] R.M. Brach. Friction, Restitution, and Energy Loss in Planar Collisions. In *ASME Journal of Applied Mechanics*, Vol.51, March 1984, pp. 164-170.
- [7] M. Brokowski, M. Peshkin, and K. Goldberg. Curved Fences for Part Alignment. In *IEEE International Conference on Robotics and Automation*, Atlanta, GA, 1993.
- [8] L.C.W. Dixon. Nonlinear Optimization. The English Universities Press Ltd., 1972, pp. 82-85.
- [9] K. Fischer. An Agent-Based Approach to Holonic Manufacturing Systems, an invited paper in *Intelligent Systems for Manufacturing: Multi-Agent Systems and Virtual Organizations*, edited by L.M Camarinha-Matos, H. Afsarmanesh, and V. Marik. Kluwer Academic Publishers, 1998.
- [10] K.Y. Goldberg. Orienting Parts Without Sensors. In *Algorithmica*, 10(2/3/4):201-225, 1993.
- [11] A. Koestler. Ghost in the Machine. The Macmillan Company, New York, 1967.
- [12] J.C. Lagarias, J.A. Reeds, M.H. Wright, and P.E. Wright. Convergence Properties of the Nelder-Mead Simplex Method in Low Dimensions. *SIAM Journal of Optimization*, Vol.9, No.1, pp.112-147, 1998.
- [13] P.E. Lewis and J.P. Ward, The Finite Element Method: Principles and Applications. Addison-Wesley Publishing Co., pp. 183-202, 1991.
- [14] K. Y. Goldberg. Orienting polygonal parts without sensors. In *Algorithmica*, 10(2):201-225, August 25, 1993.

- [15] Q. Li and S. Payandeh. Planning Velocities of Free Sliding Objects as Free Boundary Value Problem. Technical report, Experimental Robotics Laboratory, Simon Fraser University, Burnaby, BC.
- [16] K.M. Lynch. Toppling Manipulation. In *IEEE International Conference on Robotics and Automation*, Detroit, Michigan, 1999.
- [17] M.A. Peshkin and A.C. Sanderson. The Motion of a Pushed, Sliding Workpiece. In *IEEE Journal of Robotics and Automation*, Vol. 4, No. 6, December 1988.
- [18] M.A. Peshkin and A.C. Sanderson. Planning Robotic Manipulation Strategies. In *IEEE Journal of Robotics and Automation*, Vol. 4, No. 5, December 1988.
- [19] M.A. Peshkin and A.C. Sanderson. Minimization of Energy in Quasistatic Manipulation Strategies. In *IEEE Journal of Robotics and Automation*, Vol. 5, No. 1, pp. 53-60, 1989.
- [20] H.F. Noriega, K.K. Gupta, and S. Payandeh. Distributed Overhead Pins for Part Orienting – An Exploratory Study. Submitted for review to *IEEE International Conference on Advanced Robotics 2003*, December 6, 2002.
- [21] S. Rusaw, K. Gupta, and S. Payandeh. Determining Polygon Orientation using Model Based Force Interpretation. In *IEEE International Conference on Robotics and Automation*, pp. 544-549, Leuven, Belgium, May 1998.
- [22] S. Rusaw. Orienting Polygons: Experiments in Automated Part Orienting. M.A.Sc. Thesis, Simon Fraser University, Burnaby, BC, September 1998.
- [23] A. Salvarinov and S. Payandeh. Flexible Part Feeder: Manipulating Parts on a Conveyor Belt by Active Fence. In *IEEE International Conference on Robotics and Automation*, pp. 863-868, Leuven, Belgium, May 1998.
- [24] D.E. Stewart. Rigid-Body Dynamics with Friction and Impact. In *SIAM Review*, Vol. 42, No. 1, pp. 3-39, 2000.
- [25] Y. Wang and M.T. Mason. Two-Dimensional Rigid-Body Collisions with Friction. In *ASME Journal of Applied Mechanics*. Vol. 59, pp. 635-642, September 1992.
- [26] D.E. Whitney. Research Issues in Manufacturing Flexibility – An Invited Review Paper for *ICRA 2000 Symposium on Flexibility*, pp. 383-388, San Francisco, CA, 2000.
- [27] J. Wiegley, K. Goldberg, M. Peshkin, and M. Brokowski. A Complete Algorithm for Designing Passive Fences to Orient Parts. In *IEEE International Conference on Robotics and Automation*, pp. 1133-1139, 1996.
- [28] T. Zhang, G. Smith, R.P. Berretty, M. Overmars, and K. Goldberg. The Toppling Graph: Designing Pin Sequences for Part Feeding. In *IEEE International Conference on Robotics and Automation*, pp. 139-146, San Francisco, CA, April 2000.

- [29] R. Zhang and K. Gupta. Automatic Orienting of Polyhedra through Step Devices. In *IEEE International Conference on Robotics and Automation*, pp. 550-556, Leuven, Belgium, May 1998.
- [30] P.J. Antsaklis and A.N. Michel, Linear Systems. The McGraw-Hill Companies, Inc., pp. 648,652-653, 1998.
- [31] Moving averages method, with reference to: The Encyclopedia of Technical Market Indicators, Colby and Meyers. URL: [http://support.ultimatetrader.com/WebHelp/cha\\_moving\\_averages.htm](http://support.ultimatetrader.com/WebHelp/cha_moving_averages.htm). Accessed on: July 16, 2002.
- [32] “Where can I get a list of friction coefficients for different materials?” With reference to: Serway Physics for Scientists and Engineers, 4th edition, p. 126. URL: <http://www.physlink.com/Education/AskExperts/ae139.cfm>. Accessed on: August 15, 2002.
- [33] Installations and Operation Manual for F/T. Intelligent Multi-axis Force/Torque Sensor System, Manual PN 9610-05-1001-11. Industrial Automation, Assurance Technologies, Inc., 1994.